Studies for the Direct Measurement of the Proton Structure Function F_L with the H1 Detector at HERA

Diploma thesis by
Carmen Diez Pardos

Diplomarbeitsäquivalente Schrift

Referees:

Prof. Dr. Hermann Kolanoski (Humboldt Universität zu Berlin, DESY)
Prof. Dr. Thomas Naumann (Universität Leipzig, DESY)

Contents

Chapter 1

Introduction

Understanding the structure of matter, its properties and interactions, is one of the fundamental questions of physics. The theory that currently describes and explains successfully most experimental data is known as the Standard Model. According to this theory, the fundamental constituents of matter are leptons and quarks and their antiparticles. There are three generations of leptons and quarks and they interact via the exchange of gauge bosons. The electromagnetic force, mediated by virtual photons, and the weak force by Z^0 and $W^{\pm}$ bosons are described by the unified electroweak model. The strong interaction, mediated by gluons, is described by Quantum Chromodynamics (QCD).

The scattering experiments have had a fundamental role in the research of elementary particles since the Rutherford experiments, which studied the structure of the atom (1911) or later the SLAC experiment, which showed the partonic substructure of the nucleon (1969). At HERA electrons were collided head-on with protons. The former can be regarded as a source of virtual photons which penetrate the proton and resolve its substructure. Due to the large energy transfer, the proton usually breaks up producing multi-particle states of high invariant mass which allow to study the interaction between elementary particles in detail.

Since 1992, HERA operated at a high centre of mass energy, above 300 GeV in order to explore the region of highest momentum transfers Q^2 and high transversal scales. One of the achievements of its program has been the measurement of the F_2 structure function. However it was not possible to measure directly the longitudinal structure function without modifying the centre of mass energy. Then during the last three months of HERA running, two special runs with lower proton beam energy took place devoted to the mentioned measurement. The objective of the third proton beam energy run was to extend the range of F_L data and provide valuable systematic cross checks. Apart from measuring F_L, other contributions of this new data will be the measurement of the diffractive longitudinal structure function $F_L^D(x_{IP}, Q^2, \beta)$, and the contribution to measure total cross sections and extend the kinematic range of the inclusive F_2.

The measurement of F_L will help to determine the gluon distribution at low x, and particularly at low Q^2, to determine whether fixed-order calculations in QCD are sufficient or

other theoretical extensions may be needed. It is also an important measurement to make predictions and comparisons at the LHC, providing a constraint on the determination of the gluon density in the x range of W and Higgs production at LHC [2, 3].

The aim of this work is to prepare for the measurement of F_L. This diploma thesis is organised as follows: The theoretical background, ie. deep inelastic scattering, quark parton model, structure functions, etc. and the motivation of this diploma are presented in the second chapter. An overview of HERA and the H1 detector is introduced on the following chapter. In chapter 4 the data sets analysed and the general selection are described. Before carrying out any analysis of the data, it is obviously necessary to study the efficiency of the detectors involved. Therefore in chapters 5 and 6 the performance of the detectors which are significant for the measurement of the proton longitudinal structure function, SpaCal, CIP and BST are studied. One of the basic quantities which has to be determined precisely is the energy of the scattered electron in the SpaCal, the necessary calibration is introduced in chapter 7. The last two chapters are dedicated to study the data collected in 2007. First of all, the stability, focusing on the three energy runs in 2007, is shown, to study the relative normalisation between the samples. Finally in chapter 9, the first cross sections for high and low energy proton beam runs are obtained.

Chapter 2

Theoretical Background: Deep Inelastic Scattering

The deep inelastic scattering (DIS) is the scattering of an electron off a proton with sufficient energy to interact with a charged constituent of the proton, producing a multihadronic final state. These processes are characterised by the exchange of a space-like virtual gauge boson between the interacting lepton and proton, see figure 2.1. Depending on the exchanged boson the DIS processes can be classified into two groups:

Neutral current processes (NC) $ep \longrightarrow eX$ are mediated by the exchange of a neutral gauge boson, photon or Z^0.

Charge current processes (CC) $ep \longrightarrow \nu_e X$ are mediated by the exchange of a charged gauge boson, $W^{\pm}$.

CC processes are hindered compared to NC processes due to the high mass of the $W^{\pm}$ bosons.

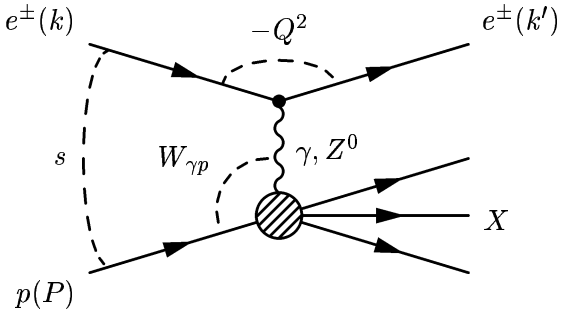

Figure 2.1: Schematic diagram of a deep inelastic lepton-nucleon scattering process. The four vectors of the particles are given in parentheses.

2.1 DIS Kinematics

The usual variables to describe the lepton-nucleon scattering are:

$q^2=(k-k')^2$ is the squared momentum transfer, where k and k' are the 4-vector of the incoming and outgoing electron[1] respectively. In order to work with a positive defined variable, the photon virtuality, $Q^2 = -q^2$, is introduced. It determines the resolving power of the interaction.

$W^2_{\gamma p} = (P+q)^2$ defines the hadronic invariant mass, γ-proton centre of mass, where P is the 4-vector of the incoming proton and q is the 4-vector of the photon

$s = (k+P)^2$ is the squared centre of mass energy of the lepton-nucleon system.

$x = \frac{Q^2}{2P\cdot q}$ is the dimensionless Bjorken variable, corresponding, in the quark parton model, to the fraction of the proton momentum taken by the parton hit by the exchanged photon or Z boson.

$y = \frac{q\cdot P}{k\cdot P}$ known as the *inelasticity variable* which gives, in the rest frame of the proton, the fraction of the incoming lepton energy carried away by the exchanged boson.

These quantities are not independent from each other, neglecting the proton and the electron mass, which are two and six orders of magnitude smaller than the centre of mass energy of the system, y is related to x and Q^2 by the equation

$$Q^2 = sxy. \tag{2.1}$$

Depending on the photon virtuality different regimes are defined, the photoproduction domain is defined by $Q^2 \sim 0$ GeV^2 and the deep inelastic scattering regime by $Q^2 > 1$ GeV^2.

2.2 Determination of the Event Kinematics

A precise measurement of the DIS cross section requires an accurate reconstruction of the kinematics describing the scattering process. These can be reconstructed using the scattered lepton, the hadronic final state or a combination of both methods [4]. Using several methods is important for the maximum coverage of the kinematic range and the control of systematic uncertainties.

In the *"electron method"* the event kinematics are determined from the measured energy of the scattered electron, E'_e, and its polar angle θ_e:

$$y_e = 1 - \frac{E'_e(1-\cos\theta_e)}{2E_e}, \qquad Q^2 = 2E'_eE_e(1+\cos\theta_e) = \frac{E'^2_e\sin^2\theta_e}{1-y_e}. \tag{2.2}$$

The coordinate system of H1 is defined such that the positive z-axis is in the direction of the incident proton beam, i.e. polar angles are defined with respect to the proton beam

[1] In this diploma thesis the term electron is used to refer to both electron and positron.

direction. From the above formulae the following conclusions can be drawn: If the electron is scattered at large angles, $\theta_e > 155^\circ$, the inelasticity y is almost defined by its energy E'_e, the lower the energy, the larger values of y are reached. The virtuality Q^2 depends mainly on θ_e at low y, large values of the polar angle correspond to small values of Q^2 and vice versa.

Performing the error propagation for the inelasticity y one obtains:

$$\frac{\delta y_e}{y_e} = \frac{1-y_e}{y_e}\left(\frac{\delta E'_e}{E'_e} \oplus \frac{\delta\theta_e}{\tan(\theta_e/2)}\right) \tag{2.3}$$

where $\oplus$ denotes quadratic addition, $A \oplus B = \sqrt{A^2+B^2}$. The electron method is accurate at large y (events with the electron scattered into the backward calorimeter, see section 3.2.3, large θ, low E'_e). The resolution degrades with $\frac{1}{y}$ as E'_e approaches the electron beam energy E_e. Thus, it is usually used for $y > 0.1$. Variables reconstructed with this method are sensitive to the initial state radiation, so corrections are needed.

Another method is the *"hadronic method"*, using the hadronic final state particles. The detector has no 4π coverage so there is some leakage of particles along the beam. As the proton beam energy is much greater than the electron beam energy, see next chapter, the leakage is more significant in its direction. One has to use the variables which are less sensitive to these losses. These can be derived from the transverse momentum balance in the event:

$$0 = P_t^{in} = P_t^{out} = E'_e \sin\theta_e + P_{t,h} = E'_e \sin\theta_e + \left|\sum_i \mathbf{p}_{\perp,i}\right| \tag{2.4}$$

and from the conservation of the difference of energy and longitudinal momentum:

$$(E_p^{in} - P_{z,p}^{in}) + (E_e - P_{z,e}) = 2E_e = E'_e(1-\cos\theta_e) + \Sigma \tag{2.5}$$

with

$$\Sigma = \sum_i E_i(1-\cos\theta_i) \tag{2.6}$$

The inelasticity can be determined as:

$$y_h = \frac{\sum_i (E_i - p_{z,i})}{2E_e} = \frac{2E_e - E'_e(1-\cos\theta_e)}{2E_e} = \frac{\sum_i E_i(1-\cos\theta_i)}{2E_e} = \frac{\Sigma}{2E_e} \tag{2.7}$$

where E_i and $p_{z,i}$ are the energy and longitudinal momentum of a particle i in the hadronic final state, neglecting its mass. The hadronic scattering angle is defined by

$$\tan\frac{\theta_h}{2} = \frac{\Sigma}{P_{t,h}} \tag{2.8}$$

where $P_{t,h}$ is the transverse momentum of the hadronic final state particles. In the quark parton model (QPM), θ_h defines the direction of the struck quark related to θ_e,

$$\tan\frac{\theta_h}{2} = \frac{y}{1-y} \cdot \tan\frac{\theta_e}{2} \tag{2.9}$$

This relation and y_e determine the scattered electron energy from θ_h and θ_e in the *"double angle method"*, used for calibration purposes, see chapter 7.

The third method is the *"Σ method"* which uses measurements from the scattered lepton (θ_e, E_i') and the hadronic final state (Σ). The kinematic variables are defined as

$$y_\Sigma = \frac{\Sigma}{\Sigma + E_e'(1-\cos\theta_e)}, \qquad Q^2_\Sigma = \frac{E_e'^2 \sin^2\theta_e}{1-y_\Sigma}. \tag{2.10}$$

The hadronic variables y_h and y_e are related by

$$y_\Sigma = \frac{y_e}{1+y_h-y_e}. \tag{2.11}$$

The results of performing an error propagation for the inelasticity for the hadronic and Σ method are:

$$\frac{\delta y_h}{y_h} = \frac{\delta\Sigma}{\Sigma} \tag{2.12}$$

$$\frac{\delta y_\Sigma}{y_\Sigma} = (1-y_\Sigma)\left(\frac{\delta\Sigma}{\Sigma} \oplus \frac{\delta E_e'}{E_e'} \oplus \frac{\delta\theta_e}{\tan(\theta_e/2)}\right). \tag{2.13}$$

The precision of these methods compared to the electron method is better for low y. They show the same behaviour at low y since the term $\frac{\delta\Sigma}{\Sigma}$ dominates the resolution of δy. At large values of y the resolution of y_Σ is better than the one of y_h due to the factor $(1-y)$. The Σ method is also less sensitive to initial state radiation, using the $E-p_z$ conservation in the event, it absorbs ISR effects into its definition. For this analysis the electron method and the Σ method will be used.

2.3 Cross section and Structure Functions

At a fixed centre of mass energy, the DIS measured cross-section depends only on two independent kinematic variables due to the ϕ symmetry, the momentum conservation and negligible particle masses. These are chosen to be x and Q^2. The neutral current double differential cross section in the one-photon exchange approximation is given by

$$\frac{d^2\sigma}{dxdQ^2} = \kappa\left(F_2(x,Q^2) - \frac{y^2}{Y_+}F_L(x,Q^2)\right) \tag{2.14}$$

where $Y_+ = 2(1-y)+y^2$ and $\kappa = \frac{2\pi\alpha^2}{Q^4 x}Y_+$. F_2 and F_L are the proton structure functions. Due to the positivity of the cross sections for longitudinally and transversally polarised photons scattering off protons, the proton structure functions obey the relation $0 \le F_2 \le F_L$.

The ep process can be understood as the interaction of a flux of virtual photons with the proton. Then $\frac{d^2\sigma}{dxdQ^2}$ can be written as [4]

$$\frac{d^2\sigma}{dxdQ^2} = \Gamma(y)(\sigma_T + \epsilon(y)\sigma_L) \tag{2.15}$$

where $\Gamma(y) = \frac{Y_+\alpha^2}{2\pi Q^4 x}$ corresponds to the flux factor, $\epsilon(y) = \frac{2(1-y)}{Y_+}$ to the photon polarisation and σ_T, σ_L are the cross sections of the interaction of transverse and longitudinally polarised photons. These are related to the structure functions as:

$$F_2(x,Q^2) = \frac{Q^2}{4\pi^2\alpha}(\sigma_T(x,Q^2) + \sigma_L(x,Q^2)), \qquad F_L(x,Q^2) = \frac{Q^2}{4\pi^2\alpha}\sigma_L(x,Q^2). \tag{2.16}$$

The ratio $R = \sigma_L/\sigma_R$ measures the amount of photon-proton scattering with different polarisation.

The experiments at SLAC [8] in the seventies showed that at $Q^2 \approx 5$ GeV^2 the dependence of the structure functions on Q^2 vanishes and they depend only on x. This is called the "scaling behaviour" of the proton structure functions and it was explained by Bjorken [10] and interpreted by Feynman leading to the Quark Parton Model, QPM [9]. In the QPM the DIS is interpreted as scattering of point-like, quasifree constituents within the proton, in the frame in which the proton has infinite momentum. The DIS is the sum of incoherent elastic lepton-parton scattering processes.

In this model the structure function F_2 can be expressed as a sum of quark/antiquark momentum distribution $xq_i(x)$ weighted with the square of their electric charge e_i:

$$F_2(x) = \sum_i e_i^2 x[q_i(x) + \bar{q}_i(x)]. \tag{2.17}$$

The functions $q_i(x)$ are the probability momentum density functions of the partons i inside the proton.

The ratio R depends on the spin of the interacting particles. A spin 1/2 massless particle cannot absorb a longitudinally polarised photon without breaking helicity conservation, therefore the QPM predicts that $\sigma_L = 0$ which leads to

$$F_L = 0 \tag{2.18}$$

known as the Callan-Gross relation. In the early measurements R was consistent with zero which gave support to the idea that partons in the nucleus were in fact quarks, spin 1/2 and massless particles [11].

One of the main contributions of HERA was to measure F_2 with high precision to confirm the scaling violation of Q^2. Together with the violation of the mentioned Callan-Gross relation which was as well experimentally confirmed, the naive approach of the QPM had to be modified to take into account this features predicted by QCD.

2.3.1 Quantum Chromodynamics and QCD Evolution Equations

QCD describes the strong force, it introduces a new quantum number, colour, carried by the quarks in addition to their charge. There are three colours and the interactions are invariant under SU(3) transformations. Eight massless gauge bosons enter the theory, the gluons, which are electrically neutral but carry colour. The running coupling constant, α_s, decreases at large energy scales and quarks are *asymptotically* free and increases at lower energies, quarks are confined to colourless hadrons. For large momentum scales, $Q^2 > 1$ GeV^2, perturbative calculations using order-by-order expansions in α_s are possible.

Then according to QCD, protons are not only constituted by quarks but also by gluons binding the quarks in the proton. Fluctuations such as emission and reabsorption of gluons and creation and annihilation of $q\bar{q}$ are expected. Some of these fluctuations can be seen depending on the resolving power of the probe and the time of the interaction, changing the partonic structure of the hadron. In other words, the structure functions acquire Q^2 dependence.

The parton distributions in the hadron cannot be calculated from first principles, however, thanks to the QCD factorization theorem the parton evolution, the Q^2 dependence of partons, can be calculated within perturbative QCD. These parton evolution equations are known as DGLAP (Dokshitzer-Gribov-Lipatov-Altarelli-Paresi) evolution equations. They describe the way that the quark, q, and the gluon, g, momentum distributions in a hadron evolve with the scale of the interactions Q^2, see expression 2.19. The splitting functions P_{ij} describe the probability of parton j to emit a parton i with a given fraction of parton j momentum [5]. They are obtained in QCD by perturbative expansion in α_s. In leading order the parton distribution acquires a Q^2 dependence and beyond leading order the splitting functions depend on the factorisation scale and the definition of parton distribution is not unique. This affects the relation between quarks and structure functions.

$$\frac{\partial}{\partial ln Q^2}\begin{pmatrix} q \\ g \end{pmatrix} = \frac{\alpha_s(Q^2)}{2\pi}\begin{bmatrix} P_{qq} & P_{qg} \\ P_{gq} & P_{gg} \end{bmatrix} \otimes \begin{pmatrix} q \\ g \end{pmatrix} \tag{2.19}$$

Due to the additional particles at the hadronic vertex it is possible to conserve the helicity and angular momentum with a longitudinally virtual photon. In next to leading order the Callan-Gross relation is violated and F_L takes the form: [7]

$$F_L(x) = \frac{\alpha_s(Q^2)}{4\pi}x^2\int_x^1 \frac{dz}{z^3}\left[\frac{16}{3}F_2(z,(Q^2)) + 8\sum e_q^2\left(1-\frac{x}{z}\right)zg(z,(Q^2))\right] \tag{2.20}$$

with contributions from quarks and gluons.

At low x, F_L essentially determines the gluon distribution $xg(x,Q^2)$ [1],

$$xg(x) \propto F_L(0.4x). \tag{2.21}$$

The measurement of the longitudinal structure function would be a clean probe of the gluon in the domain of x $(10^{-4}, 10^{-3})$.

2.4 Measurement of the Longitudinal Structure Function

The extraction of $F_2(x, Q^2)$ from the measured cross section has only be possible at low y, where the contribution of $F_L(x, Q^2)$ can be neglected, or at high y making assumptions on F_L and the latter has not been measured directly. The direct method to obtain F_L is to measure the differential cross section at fixed (x,Q^2) and different y, ie. different beam energy and to fit the reduced cross section, defined in equation 2.22, with a straight line as a function of $f(y) = y^2/Y_+$.

$$\sigma_r = \left(F_2(x, Q^2) - f(y)F_L(x, Q^2)\right) \tag{2.22}$$

2.4.1 Running at Low Proton Beam Energies

According to equation 2.1, fixing (x, Q^2) and varying y can be done by changing s. Since $s = 4E_eE_p$ this could be done varying the electron, proton or both beam energies. It was decided to lower the proton beam energy because reducing the electron beam energy would have required to lower the scattered electron energy below the trigger threshold and it would have affected the scattered electron angle more that the reduction of the proton beam energy. Another advantage of reducing E_p is the maximum cancellation of systematics when making a relative cross section measurement [1].

In 2007 three data sets were taken, the proton beam energies were E_p= 920 GeV, like it had been previously, E_p= 460 GeV and finally E_p= 575 GeV. In this thesis these data sets will be often referred to as *high energy*, *low energy* and *medium energy* data respectively. The choice of the first reduced proton beam energy was a compromise between the requirement to have the lowest proton beam energy and the luminosity, which is diminished approximately $\propto E_p^{-2}$. The measurement could be also done with only two proton beam energy values but the third run, E_p= 575 GeV, provides a statistical cross-check of the systematics uncertainties which compensates the partial loss of statistical precision of a longer E_p= 460 GeV run.

To illustrate the method, the reduced cross section at $x = 0.00025$ and $Q^2 = 10$ GeV^2 is plotted in figure 2.2 for the three energies [39]. One can see that the precision of F_L requires the difference between $f(y)$ at high and low energy beams to be large, ie. large difference between the centre of mass energies as it was stated in the previous paragraph. The precision varies as

$$\frac{1}{f(y_{460GeV})} \approx \frac{1}{y^2_{460GeV}} \tag{2.23}$$

where y_{460GeV} corresponds to the y value for the E_p=460 GeV data. It is necessary to reach the highest value of y possible. F_L is sensitive to small relative shifts of the cross sections and not to absolute errors.

At low enough values of y the second term of the equation 2.22 is negligible and the value of the reduced cross section is the same independently of the centre of mass energies at fixed x, Q^2. For higher values of y the measured cross section depends on s. That behaviour is shown figure 2.3. The reduced cross section as a function of the proton beam energy is plotted

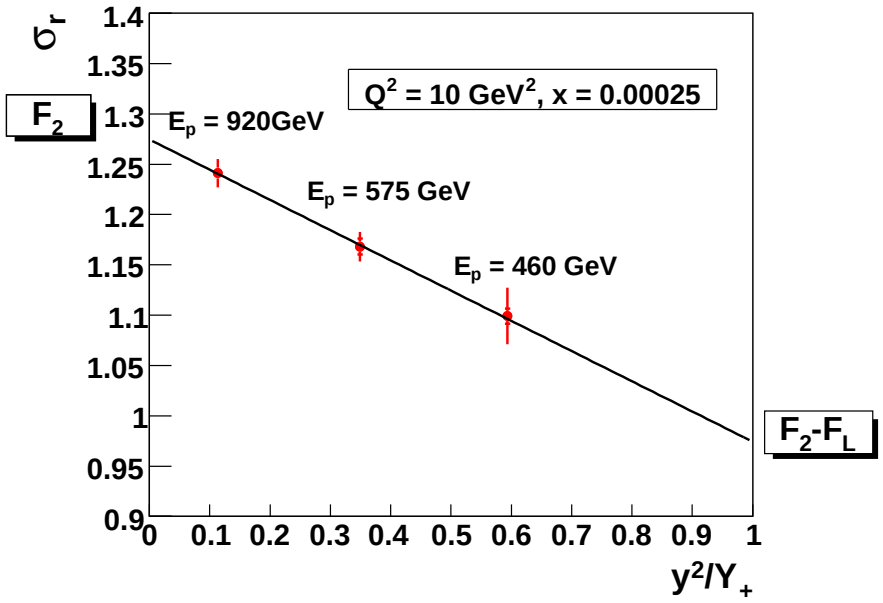

Figure 2.2: Simulated measurement of the reduced cross section for data at 920 GeV (30 pb^{-1}), 575 GeV (10 pb^{-1}) and 460 GeV (13 pb^{-1}). The inner error bar represents the statistical error. The full error bar denotes the statistical and the systematic uncertainty added in quadrature [39].

for $Q^2 = 15$ GeV^2 and for three different values of x. At $x = 0.001$ the relative difference between σ_r for E$_p$= 460 GeV and E$_p$= 920 GeV is about 1%. At $x > 0.001$, which implies y smaller than 0.3 for E$_p$= 460 GeV, the value of σ_r is essentially the same for the three proton beam energies. At lower values of x the difference in σ_r increases and at $x = 0.00035$ it is expected to be around 20%. This corresponds to $y \approx 0.85$ for the low proton beam energy data, which is the upper limit that H1 is expected to reach. In the figure, the values of the kinematic plane that will be analysed in this work are represented by closed circles and the triangles correspond to the expected future measurement by H1.

It is fundamental to check at $x > 0.001$ the relative normalisation of the three sets, proportional to the luminosity measurement, because a shift would ruin the measurement of F_L.

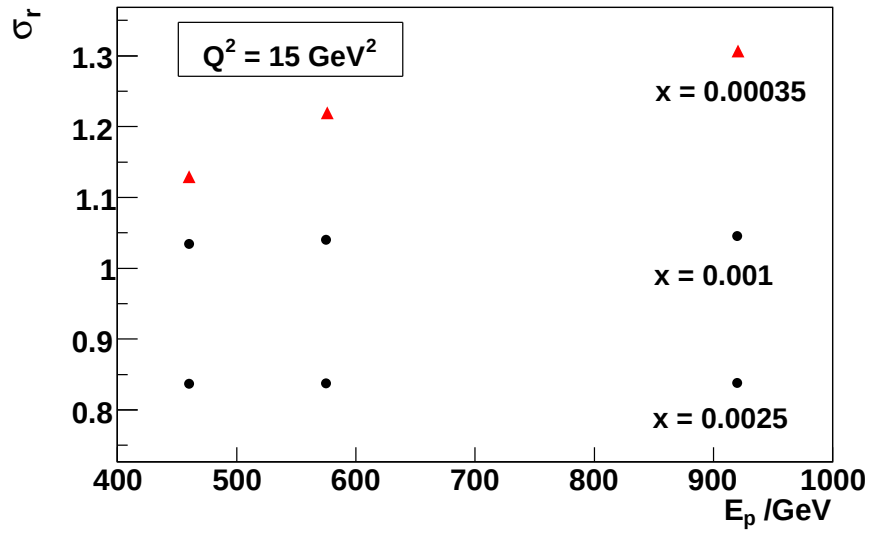

Figure 2.3: Reduced cross section for data at 920 GeV, 575 GeV and 460 GeV at $Q^2 = 15$ GeV^2 for three different values of x. The dots represent values of x which will be analysed in this thesis and the triangles represent the reduced cross section at the minimum x that H1 can measure. The values of the cross sections are obtained using the QCD fit H1PDF2000 [36].

Chapter 3

HERA and the H1 Detector

In this chapter the HERA accelerator and the H1 detector are introduced. The description of the H1 detector corresponds to its configuration after the year 2003.

3.1 The HERA Accelerator

The particle accelerator HERA (Hadron-Electron-Ring-Anlage) was the first hadron/lepton collider and it was operating from the summer 1992 to the end of June 2007. It consists of two storage rings to accelerate protons or electrons (positrons) respectively, see figure 3.1. The energy of the lepton beam was 27.55 GeV. The energy of the proton beam has been modified for different periods: From 1992 to 1998 it was 820 GeV, which corresponds to a centre-of-mass approximate of 300 GeV. Then the energy was increased to 920 GeV, yielding

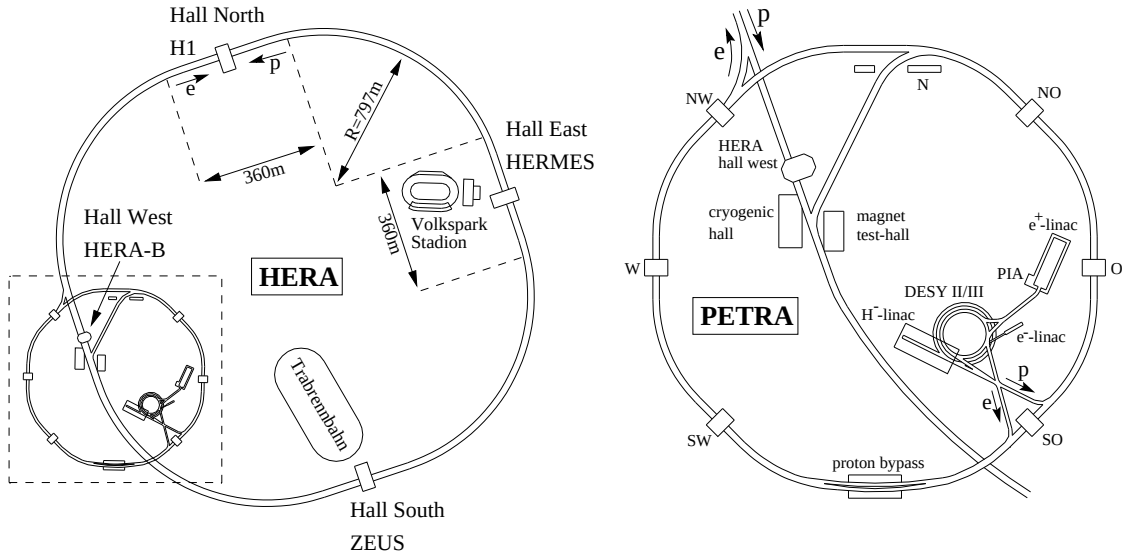

Figure 3.1: The electron-proton storage ring HERA is shown on the left side. A zoomed view of the pre-accelerators is presented on the right side.

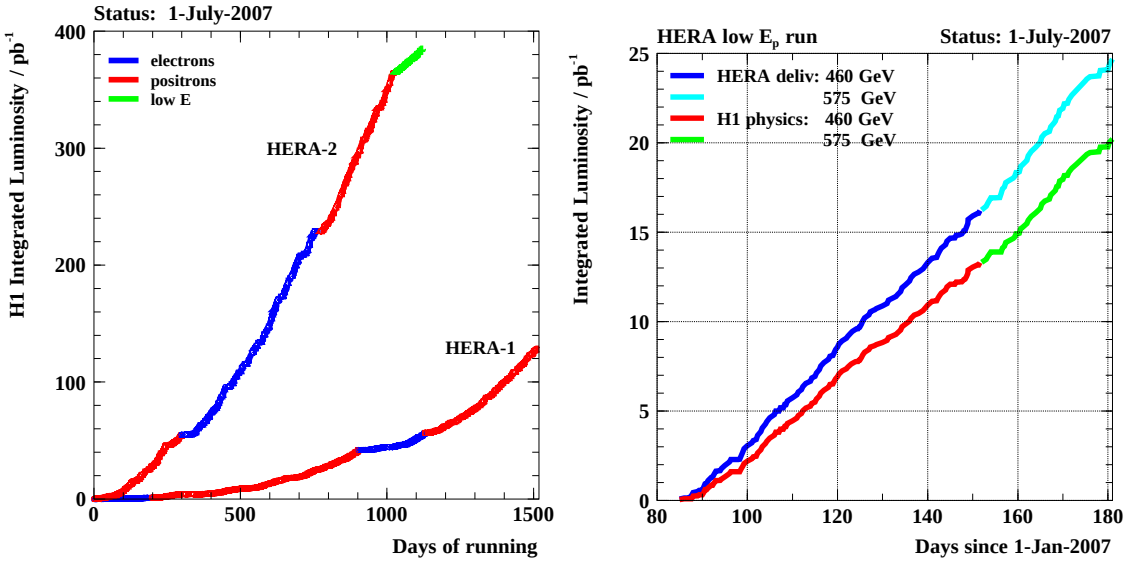

Figure 3.2: Integrated luminosity delivered by HERA I and HERA II (left plot) and integrated luminosity delivered and physics luminosity collected by H1 during the low and intermediate energy running period (right plot).

$\sqrt{s} \approx 320$ GeV. The last three months of HERA operation were devoted to two reduced proton beam energy runnings: from 26 March to 1 June, it was 460 GeV and the last month, to 30 June it was 575 GeV.

The HERA lepton beam magnets operate at ambient temperature, while the proton ring magnets are superconducting. The particle beams are stored in bunches with 96 ns bunch crossing intervals, corresponding to a 10.4 MHz collision rate. Some number of bunches are left unpaired for background studies. The usual maximum beam current reached just after injecting the new beams was $I_p = 100$ mA for protons and $I_e = 40$ mA for protons and for electrons respectively, with a typical peak luminosity of 4.5×10^{31} cm^{-2}s^{-1}. There are four experiments along the ring, two of them are fixed target experiments, HERMES which used the lepton beam and HERA-B (only until 2003) using the proton beam, and two colliding experiments, H1 and ZEUS. In 2000 the HERA I phase was finished and the collider and the detectors were upgraded for the HERA II phase, characterised by a higher luminosity. In figure 3.2 the integrated luminosity for the whole HERA running period and the luminosity collected during the low and medium energy runs in 2007 are shown.

At the high centre of mass, Q^2 values up to 10^5 GeV^2 were reached at the highest x, y possible. At low Q^2, x values down to $5 \cdot 10^{-5}$ were reached. HERA operated using both electrons and positrons, their interaction differ due to electroweak effects. After the HERA II upgrade, lepton beam polarisation was available for the colliding beams having a similar effect as the sign of the lepton.

3.2 The H1 detector

The H1 experiment is arranged cylindrically around the beam axis. The origin of the H1 coordinate system is at the nominal interaction point. Points within the detector are usually defined using the cartesian coordinates. The z-axis is pointing in the direction of flight of the incoming proton, the y-axis is pointing vertically upwards and the x-axis points horizontally to the centre of the storage ring. Angles are described with a spherical system (r, θ, ϕ), such the azimuthal angle ϕ lies in the xy-plane and the polar angle θ is measured from the positive z-axis.

Due to the imbalance of the energy of the electron beam and proton beam, the centre of mass system is boosted in the positive z-direction with respect to the laboratory system, many more particles are produced at small angles, the forward direction. Therefore the H1 detector has different systems in the forward and backward direction. The H1 detector combines tracking in a solenoidal magnetic field of 1.15 T with calorimetry to investigate high-energy ep interactions. The energy of the electron, when scattered into the backward region of the detector ($153° < \theta_e < 177°$) is measured with the Spaghetti Calorimeter, SpaCal, a lead-fibre calorimeter. The identification of the scattered lepton is improved and the polar angle is measured with a backward chamber, BPC, and a backward silicon strip detector, BST. The hadronic final state is reconstructed with the Liquid Argon calorimeter, LAr, the tracking detectors and the SpaCal. The interaction vertex is determined with the central tracking detector which consists of a concentric z chamber, COZ, and two concentric jet drift chambers, CJC. The vertex reconstruction is complemented by the inner proportional chamber, CIP. The luminosity is determined using the process $ep \longrightarrow ep\gamma$, the final state photon and electron can be detected in calorimeters which are situated close to the beam pipe. In figure 3.3 an overview of the detector is shown, the most important parts are numbered.

In the next section the mean systems of the H1 detector after the last upgrade, will be presented. A complete description of the detector as it was in 1997 can be found in [12] and [13].

3.2.1 Tracking Systems

The tracking system of H1 provides triggering, reconstruction and particle identification of charged particle tracks. It covers the polar angular region $7° < \theta < 173°$. Due to the asymmetry between the electron and the proton beam energies the tracking system is divided in different parts depending on the direction: forward tracker, central tracker and backward tracker.

The Central Tracker Detector (CTD) is composed of a number of drift and proportional chambers for tracking and triggering. It consists on the Central Jet Chambers (CJC1, CJC2), the Central Inner Proportional chamber (CIP), Central Outer z-chamber (COZ) and Central Silicon Tracker (CST). The designed resolution for the momentum of charged tracks is $\sigma_p/p^2 \approx 3 \cdot 10^{-3}$ GeV^{-1} and for the polar angle $\sigma(\theta) \approx 1$ mrad. In figure 3.4 a transversal cut of the CTD and the BST/FST, described in next section, looking in the negative z direction

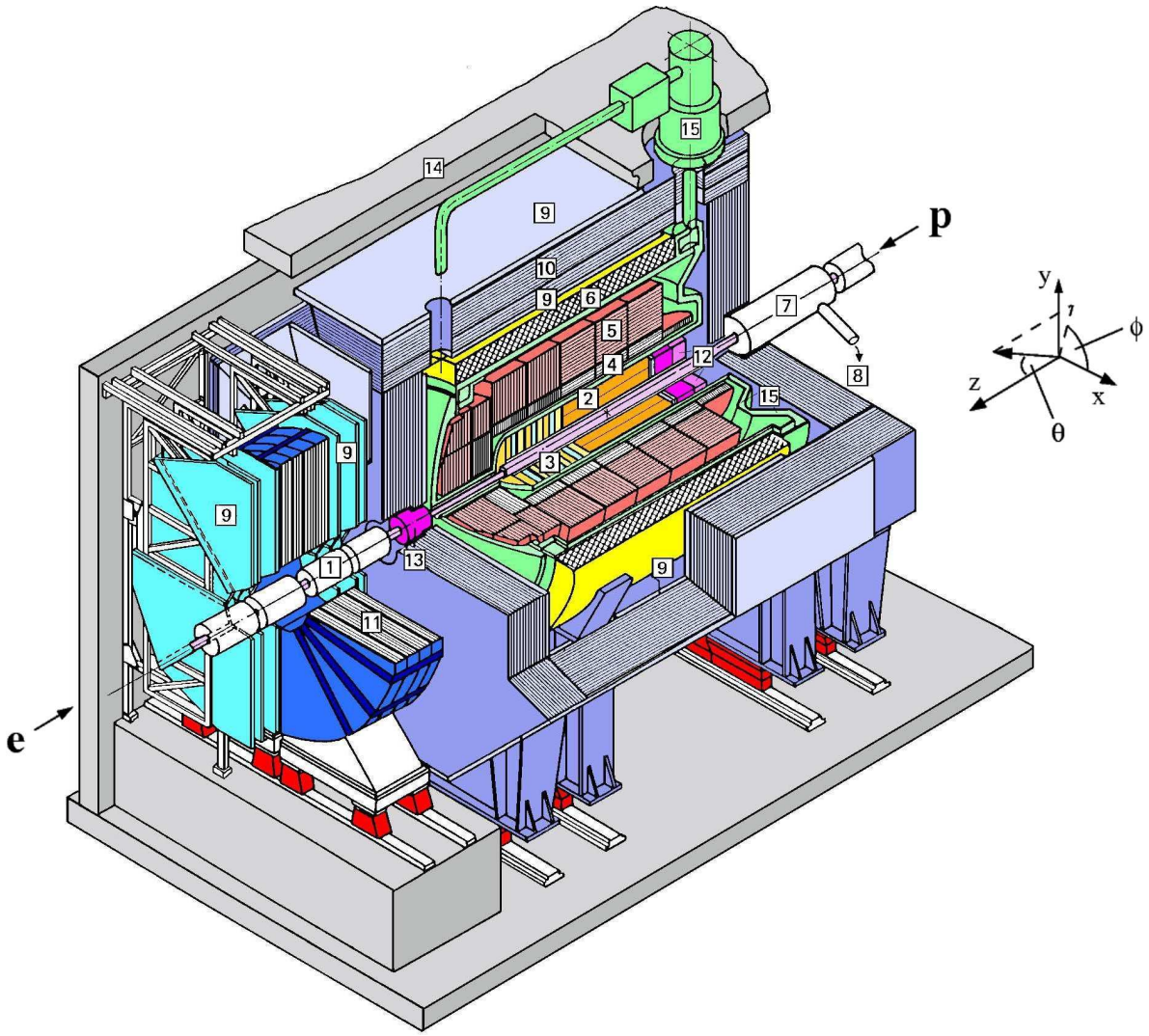

Figure 3.3: H1 detector: The main tracking system is provided by the *Central* [2] and *Forward Trackers* [3]. The calorimetry is provided by a *Liquid Argon Calorimeter (LAr)* with *electromagnetic* [4] and *hadronic* [5] sections in the central and forward region and a *Lead-Scintillating Fibre Calorimeter (SpaCal)* [12] in the backward direction. The calorimeter region is surrounded by a large superconducting coil [6], which provides a *uniform solenoidal magnetic field* of 1.2 T. The streamer tubes [9] in the iron return yoke [10] measures hadronic shower leakage and identifies muons in the central region. In the forward direction there are dedicated muon systems [9] with a separate toroid [11].

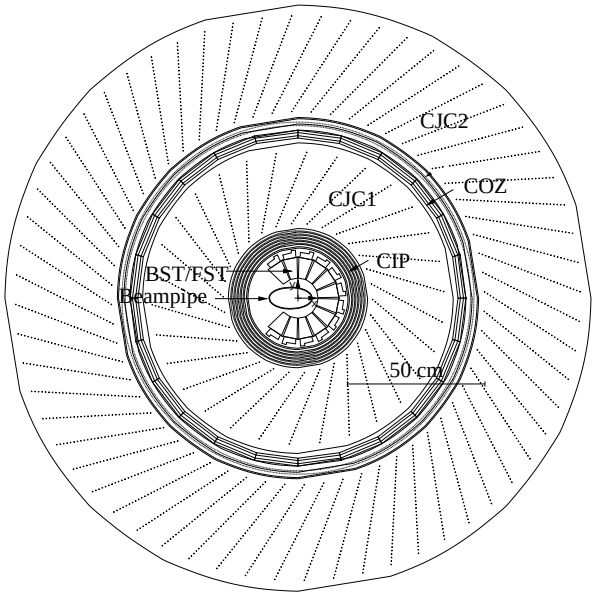

Figure 3.4: Projection of the Central trackers, BST and FST in the negative z direction.

is presented.

The CJC is the main device of the H1 tracking system, it comprises two concentric parts: The inner CJC1 and the outer CJC2, with sensor wires running in the y direction and a 1.15 T magnetic field parallel to the z-axis. The drift cells are tilted by 30° with respect to the radial direction, so the electrons created by the ionisation travels perpendicularly to the track direction. The CJC tracking resolution in the $r-\phi$ plane is 170 μm and the resolution in the z-direction is $\sigma_z = 2.2$ cm. It provides information about particle identification measuring dE/dx along the track. The COZ was built to complement the measurement of CJC, the chamber resolution is about 300 μm in the z-coordinate. The CIP is mainly used for triggering purposes. The CIP was upgraded within HERA 2000 upgrade. It is a concentric multiwire chamber situated between $z = -1127$ mm and 1043 mm, which covers the region $11° < \theta < 169°$. It consists of five layers which have 480 anode wires of 25 μm diameter strung parallel to the beam line. It is used for trigger Level 1, for details see [14].

The Backward Proportional Chamber, BPC, is the proportional gas chamber placed in the region in front of the SpaCal and its purpose is to ensure more precise calorimeter cluster position and partial particle identifications, especially photons and electrons. It consists of three supermodules with the sense wires strung perpendicularly to the beam line.

The Forward Tracker Detector is designed to provide accurate measurement of charged particle tracks in the forward direction. It covers the polar angular region from $7° < \theta < 30°$.

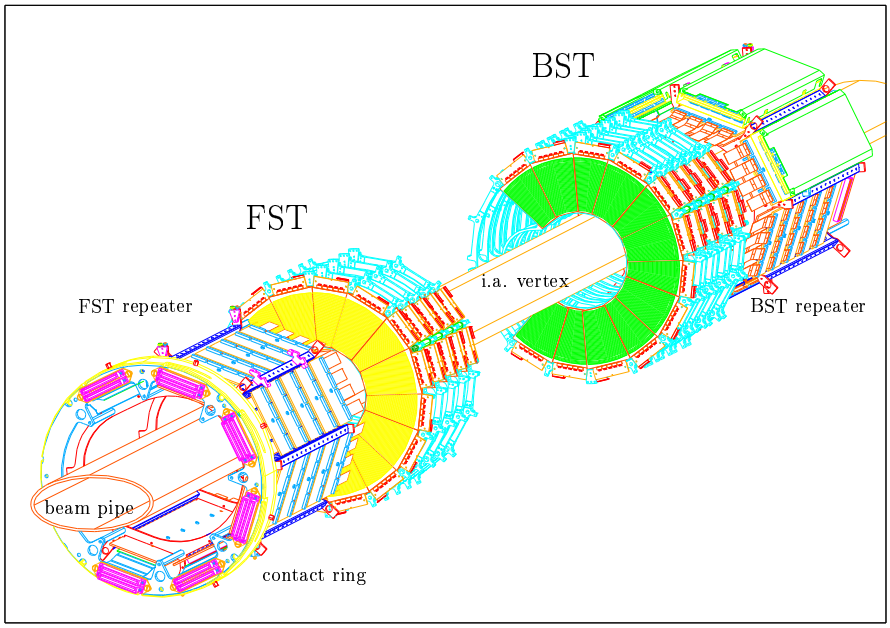

Figure 3.5: Schematic view of the FST and BST trackers.

3.2.2 Silicon Trackers

The silicon trackers have a good spacial resolution and they can supply signals very fast. The three silicon trackers in H1 are the Central Silicon Tracker (CST), the Forward and Backward Silicon Tracker, FST and BST respectively, see [15] for a detailed description. They are located close to the beam pipe. The main purpose of the CST [16] is to accomplish the track measurement with few precise points to ensure very accurate vertex measurements. It gives a 3D space hit instantly but there is some ambiguity in z which can only be resolved with the CJC. It consists of two layers of silicon sensors placed close to the beam line covering $29° < \theta < 151°$. The FST [31] and BST [22] detectors are very similar in structure, they are composed of an active volume close to the interaction point and a "repeater" section with additional readout components. The acceptance in the azimuthal angle, ϕ, is 270° due to the elliptical beam pipe. The FST covers the region $9° < \theta < 19°$ and the BST, $163° < \theta < 174°$. The main type of sensor used is a single metal strip sensor. There are 12 modules, each one covers 22.5° in ϕ from a radius between $r = 5.9$ cm and $r = 12.0$ cm, they overlap in ϕ for the detector internal alignment. Another set of twelve modules is mounted back-to-back on the same wheel, their strips cross the first modules strips at an angle of 22.5° and allow full track reconstruction.

The BST Silicon Tracker (BST) has been designed for an exact measurement of the polar angle of the scattered electron and it allows the event vertex determination by reconstructing the electron track. It complements the vertex reconstruction at low y where the hadronic final state is going forward, the vertex reconstruction efficiency is low in other track detectors due to missing acceptance. F_L contributes to the cross section mainly at high y. This corresponds to a low scattered electron energy E'_e. In this kinematic range a precise DIS measurement is

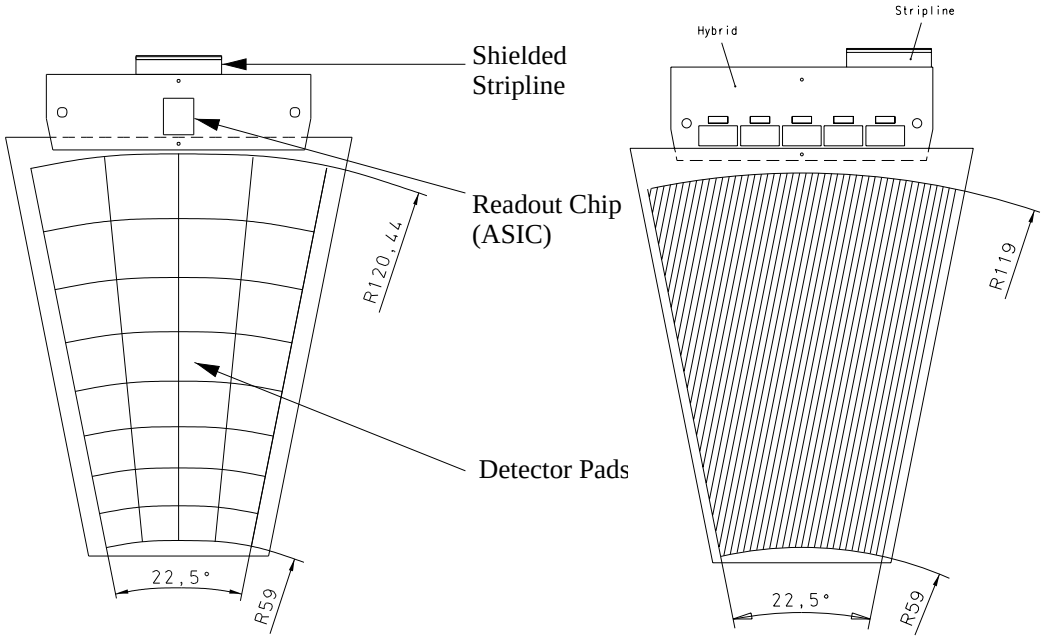

Figure 3.6: Schematic drawing of a BST Pad detector module, left, and a BST module, right.

a challenge due to the high backgrounds from photoproduction. A feature of the BST is that it is able to suppress this background contribution of neutral particles in the SpaCal. It can as well differentiate charged tracks, for example scattered electrons and pions created within the hadronic final state. The FST can be used as a cross-check for the vertex measurement for events with hadronic final state in the forward direction.

In addition there is also a trigger detector in the backward region, called "Backward Silicon Track Trigger" (BSTT) and sometimes referred to as "BST Pad", see [24]. It contains four planes of detector modules composed of pads. There are as well 12 modules per plane, each covering 22.5° in ϕ. Figure 3.6 shows the structure of two modules, corresponding to the BST strip detector and the BST pad detector. The BSTT is able to do background suppression online requiring a track. At low Q^2 the rate of photoproduction events and other beam related background is much higher than the DIS events. To suppress it, it would be necessary to higher the energy threshold of the trigger. However, to measure F_L it is necessary to trigger on low energetic scattered electrons. So requiring a track in the BSTT both kinds of background can be efficiently suppressed.

3.2.3 Calorimetry

Calorimeters are important instruments to measure the energy of a particle. The working principle is the transformation of the absorbed energy of the particle to a measurable signal proportional to the deposited energy.

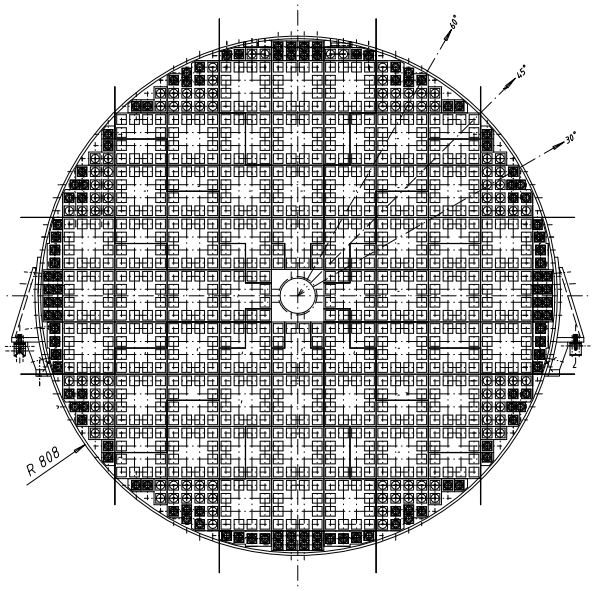

Figure 3.7: Technical drawing of the SpaCal. Each small box represents a cell, which are combined to 4×4 super modules.

The calorimetry measurement in H1 is based on the Liquid Argon (LAr) in the forward and the central region and the Spaghetti calorimeter (SpaCal) in the backward region. They are placed inside the iron return joke to have as few inactive material as possible in the way of the particles, in order to improve the scattered electron measurements. Additionally, they can be used for triggering. The LAr [17, 18] covers the polar angle $4° < \theta < 154°$. It has a hadronic and a electromagnetic section. The former is made of steel and provides 5-8 interaction lengths. The electromagnetic section lead is used to promote shower development, it provides 20-30 radiation lengths.

The SpaCal [19, 20] was designed for the precise lepton, photon energy measurement in the backward region of the experiment covering the polar angle $153° < \theta < 174°$. It is a lead/scintillating fibre calorimeter consisting of an electromagnetic section of 28 radiation lengths long and a hadronic section which is 1.02 interaction lengths long, with the inner radius of 10 cm and the outer of 80 cm. Every cell has scintillating fibres parallel to the z-axis pressed in the lead and tied together to the cone to which a light mixer of the photomultiplier is attached.

The electromagnetic section consists of 1192 cells with a cell cross section of 40.5×40.5 mm^2. The cell depth is 25 cm in the z direction, sufficient for electromagnetic showers to deposit their whole energy up to 30 GeV. Individual cells are combined to 4×4 super modules. Since the Molière radius, which describes the transversal size of the shower, is 25.5 mm it allows a good electron/hadron separation by measuring the transverse shower profiles. The time resolution is better than 1 ns, it permits the suppression of the beam induced background. The electron energy resolution is $\sigma_E/E = \frac{7\%}{\sqrt{E/GeV}} \oplus 1\%$ and the cluster position

resolution is a few mm.

The hadronic section is composed of 136 cells of 119.3 $\times$ 119.3 mm^2 cross section and 25 cm depth providing one nuclear interaction length. It is used to distinguish between hadronic and electromagnetic showers.

Both hadronic calorimeter are non compensating. The energy measurement is adjusted using software techniques.

3.2.4 Muon System

The muon detector of the H1 experiment is divided in two separate parts: Central Muon Detector (CMD) [13] and Forward Muon Detector (FMD) [21]. The former is a part of the instrumented iron yoke, which guides the magnetic field of the main solenoidal coil. It covers the polar angles $4^\circ < \theta < 175^\circ$ and it is used to detect muons with $E_\mu > 1.2$ GeV. The FMD consists of a toroidal magnet and three double-layer drift chambers in front and behind the magnet. It covers the range $4^\circ < \theta < 17^\circ$.

3.2.5 Luminosity System

The luminosity is estimated from the measurement of the Bethe-Heitler process $ep \longrightarrow ep\gamma$, which has a well known cross section. The H1 luminosity system [12] consists of an electron tagger, ET, situated at z = -5.4 m in the tunnel, a photon detector (PD) at z = -101.8 m and a veto counter (VC), part of the photon detector. The ET is a 12 channels SpaCal type calorimeter, the photon detector is a electromagnetic calorimeter and the veto counter is a water Cherenkov detector. The electrons scattered under a small angle but with reduced energy are bent by the HERA magnets to reach an exit window in the beam pipe and hit the ET. The photons reach the PD through an exit window where the electron beam pipe bends upwards. Apart from measuring the luminosity, this system can be used in addition to tag photoproduction and measure hard photons from initial QED radiation in DIS.

3.2.6 Trigger System

The task of the trigger system is to select the events originated from a given ep interaction of physics interest out of the flow of signals registered in the multitude of detector channels, to record them and to reject the background, such as synchrotron radiation from the electron beam, proton gas interaction in the beam pipe, beam halo muons or muons from cosmic radiation. As the readout rate, data transfer and storage have limited capability, fast hardware and software algorithms decide whether to keep or reject an event. The dead-time of the experiment, which is the time when signals are being read and the subsystems are insensitive to new events, should be kept to a minimum.

The central trigger system consists of four levels:

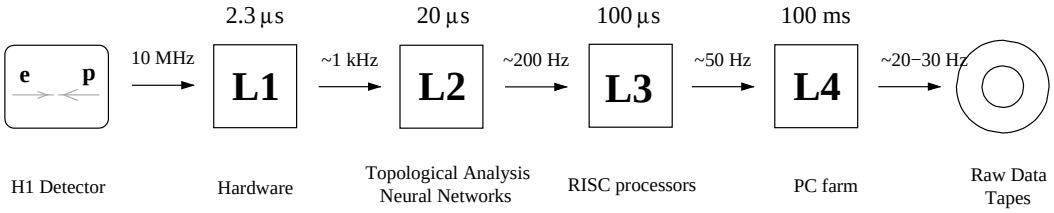

Figure 3.8: Schematic description of the four trigger levels of H1.

L1 The L1 decision is based on the information provided by various subdetectors, i.e. SpaCal, LAr, CJC, BST, CIP, muon system, which gives 256 trigger elements (TE) combined into 128 subtriggers. They can be defined in order to select interesting physics, to monitor detection efficiency or to select cosmic ray events for calibration purposes. L1 accepts events if at least one subtrigger gives positive decision, which cannot be delayed by more than 2.3 μs. The central trigger sends an L1Keep signal stopping the subdetectors pipelines. Until the pipelines do not restart, there is no data collected. A subtrigger can be prescaled with prescale n, which implies that only one out of n events with fulfilled conditions is selected. That is the way of suppressing subtriggers with too high rate.

L2 At this level neural network (L2NN) and topological analysis (L2TT) are performed within 20 μs. They verify the L1 decision working with refined information. After a positive decision, L2Keep, the readout of all subsystems starts and after a negative decision the pipelines are restarted to collect more data. The readout is finished after 1-2 ms, the complete information is then transfer to the trigger level L4.

L3 The third trigger level was activated in 2006 as part of the *Fast Track Trigger* (FTT). Its aim is to reduce the dead time and it is used only by specific triggers, ie. searches for specific decay channels and topologies. The decision if the readout should be aborted is taken after approximately 100 μs.

L4 Its purpose is not online event selection, but a reduction of offline storage space needed. It is integrated in the central data acquisition system and it is based on a PC farm. Each PC reconstructs a complete event applying a series of selection criteria depending on the subtriggers that triggered the event. Events which pass the L4 are written to tape at a rate of 20-40 Hz. It was switched off during the low and intermediate data taking period in 2007.

In figure 3.8 a schematic description of the trigger system in H1 is presented with its input rates and processing times.

Chapter 4

Data Samples and Selection

In this chapter the data samples used in this analysis and the general event selection applied is introduced.

4.1 Data Samples

The data samples used for this diploma were taken by H1 in 2007. The focus of this work is the analysis and comparison of the three proton beam energy runs. The efficiencies of the detectors and subtriggers and data quality are studied in the three cases. In chapter 8 also the positron running period in 2006 is studied to cross check with the E_p =920 GeV in 2007. In table 4.1 the different data sets are listed.

The total integrated luminosity for the studied data in 2007 is 34.1 pb^{-1} for E_p = 920 GeV sample[1], 11.8 pb^{-1} for $E_p = 460$ GeV and 6.3 pb^{-1} for $E_p = 575$ GeV.

4.2 Run Selection

The data collected by H1 is split into *luminosity runs*, each one is associated to a number corresponding to events collected under similar conditions. They could have a duration from

[1]This luminosity corresponds to the period when the subtrigger s0 had a lower prescale than s2 (10.01-13.03.07) not to the whole data collected during the high energy run.

Table 4.1: Data samples used in this analysis

Date	*run number*	*Description*
13.07.06-01.01.07	468530-492541	2006, e^+ running
01.01.07-20.03.07	492556-499909	2007 $E_p = 920GeV$
26.03.07-01.06.07	500918-507824	2007 $E_p = 460GeV$
01.06.07-30.06.07	507843-511079	2007 $E_p = 575GeV$

some minutes up to an hour, the number of recorded events varies between 10000 and 100000. Each run has an integrated luminosity value. Another time unit for the data taking is the *luminosity fill* which is a period of data taking with the same fill of electrons and protons, the lifetime of the former limits its duration to 12 hours. Beam parameters are usually stable within a fill.

4.3 General Selection

The aim of the event selection is to provide a sample of events for the cross section determination which contains the minimum amount of background events with the smallest number of selection criteria possible. The description of the DIS selection presented in this section is used for most of the studies in this thesis. In same cases, depending on the focus of the analysis, the cuts on some variables may vary or cuts related to acceptances of a certain part of the detector may be included. The modifications in the selection will be introduced in the corresponding sections.

4.3.1 Electron Identification

The starting point of the electron identification procedure is the measurement of the energy clusters in the backward calorimeter. The energy range selected is $11 < E'_e < 32$ GeV. At this relative large energy, the criterion of identifying the electron choosing the cluster with the highest energy is nearly 100% efficient. It also allows to reject a big part of the background.

Obviously, the correct identification of the scattered electron is essential to reconstruct the event kinematics. It is basic to distinguish between electromagnetic or hadronic clusters and reject the latter from the selection, which is done with the parameters proposed in [23]:

- Logarithmic cluster radius: The hadronic clusters in a electromagnetic calorimeter are usually broader than the electromagnetic ones, therefore their transversal size can be used to distinguish between the two kind of clusters. The logarithmic cluster radius estimates the transversal dimension of a cluster, it is defined as the quadratic sum of the logarithmic weighted distances r_i between the centre of the gravity of the cluster and the geometrical centre of the cell i.

$$r_{Clog} = \sqrt{\frac{\sum_i w_i^{log} r_i^2}{\sum_i w_i^{log}}} \tag{4.1}$$

  where the logarithmic weight is defined as follows:

$$w_i^{log} = \max(0, w_{cut} + ln(E_i/E_{cluster})). \tag{4.2}$$

  For data the cut off weight is 4.85 and for MC 5.05. For the selection, the requirement is $r_{Clog} < 4.0$ cm.

- *Hadronic fraction*: The so-called "hadronic fraction" is the ratio between the energy deposited in hadronic section of the SpaCal and the energy of the cluster measured by the electromagnetic section. The energy deposited in the hadronic section of the SpaCal is calculated in a radius of 15 cm around the cluster in the hadronic section. If the fraction of the energy in that cylinder is greater than 15%, $f_{had} = E_{had}/E_{cluster} > 0.15$, the cluster is classified as hadronic and rejected from the selection.

4.3.2 Vertex Reconstruction

The vertex requirement is aimed to define the position of the interaction point which is necessary to reconstruct the DIS event kinematics. In particular the z-position of the vertex is directly used for the measurement of the polar angle of the scattered electron θ_e based on the cluster information. Therefore it is important to have an accurate reconstruction. The vertex can be reconstructed using tracks of the scattered electron or hadronic final state particles in different detectors, depending on the values of Q^2 and y.

For most of the results in this thesis, the *primary vertex* reconstructed by the Central Tracker is used, if the precision is better than $\Delta z_{vtx} < 8$ cm. This requirement rejects badly reconstructed events. If there is no available central vertex, which is usually due to the lack of tracks from the hadronic final state particles for low y events, the CIP is used for the reconstruction. In this case the condition to select the vertex is that the number of *linked hits* is greater than two. This means that the hits in at least three out of the five layers which compose the detector are associated to an electron. In the following, the terms "central vertex" and "CIP vertex" will be used to refer to vertices reconstructed with the central jet chambers or the CIP, respectively. The vertex reconstructed by the FST will be used in some cases to increase the statistics, see chapters 5 and 6.

The z-vertex position is restricted to the interval $-35 < z_{vtx} < 35$ cm, which rejects contributions from the satellite bunches and background events, such as cosmic or beam induced background.

4.3.3 Longitudinal Momentum Balance: $(E - p_z)_{tot}$

$(E - p_z)_{tot}$ should be equal to twice the electron beam energy due to energy and momentum conservation. For photoproduction events it is likely to be smaller, as the electron is scattered below the backward calorimeter acceptance. $(E-p_z)_{tot}$ can also be smaller due to initial state radiation when a photon of energy $E_\gamma = E_e - 0.5 \cdot (E - p_z)$ escapes undetected along the beam pipe. Then the cut applied, $E - p_z > 35$ GeV is a good filter against background and radiative corrections.

4.3.4 Transverse Momentum Balance: $\mathbf{p}_t$ balance

The p_t *balance* ratio is defined as the coefficient of the total transverse momentum of the hadronic final state particles over the total transverse momentum of the scattered electron:

$$p_{t,ratio} = \frac{p_{t,hfs}}{p_{t,e}} \tag{4.3}$$

Due to momentum conservation one could expect $p_{t,ratio} \sim 1$. However, the hadronic final state can be produced at small angles escaping the forward calorimeter acceptance, creating an imbalance of the transverse momenta of the hadrons with the electrons. Then, low values of $p_{t,ratio}$ characterise events in which particles of the hadronic final state escaped undetected leading to energy losses. At low Q^2 this effect is especially pronounced for low values of y. To exclude that region the cut $p_{t,ratio} > 0.3$ is applied.

4.3.5 Background

Two classes of background can be distinguished, the *photoproduction* events and the so-called *non-ep interactions*. The latter contribution to the background is due to particles produced by cosmic rays or by interactions of beam particles with beam line elements, *beam-wall interactions*, or residual gas in the beam pipe, *beam-gas interactions*. The rate of this processes is larger than the DIS events rate. However, they have different timing, topologies of energy deposition and vertex distribution. Most of them are rejected requiring a localised electromagnetic energy deposition above a certain threshold in the SpaCal on the first trigger level. A further reduction to a negligible level is achieved by the selection criteria of the final analysis, first of all by the cut on the z-vertex position of the interaction vertex.

In photoproduction the exchange photon is quasi-real, $Q^2 \approx 0$ GeV^2, the scattered electron escapes undetected along the beam pipe. If the generated hadronic particles are scattered into the backward region, they could produce energy depositions in the SpaCal misidentified as electrons. A large fraction is rejected by the general electron selection requirements described in section 4.3.1. In this analysis no specific studies concerning the background were done, therefore the event selection has also the aim of keeping a "background free" sample.

4.4 Kinematic Phase Space

The optimal phase space to measure F_L corresponds to large y and Q^2 $<$ 120 GeV^2. In this kinematic range the electron is scattered through a small angle (corresponding to the backward region) and it is accompanied by part of the hadronic final state. It is necessary to identify the scattered electron to very low energies, few GeV, to reach high enough y values, $y > 0.6$ for the E_p= 460 GeV data. The photoproduction background in this region is considerable. In this region of the (x, Q^2) plane the reconstruction of the electron kinematics can be done using the SpaCal calorimeter for the energy and the Backward Silicon Tracker or the Central Jet Chamber for the precise measurement of the angle. It is also possible to remove the mentioned background by requiring a track to be associated to the energy cluster in the SpaCal, which reject photons, and by measuring its charge, which allows to remove the rest of the background (on an statistical basis) [6].

In figure 4.1 the kinematic plane (x, Q^2) is presented, the scattered electron variables y and θ_e are shown. The θ lines correspond to the acceptance of the SpaCal for the E_p= 460 GeV and E_p = 920 GeV samples. The y lines for the low energy show the limits to measure

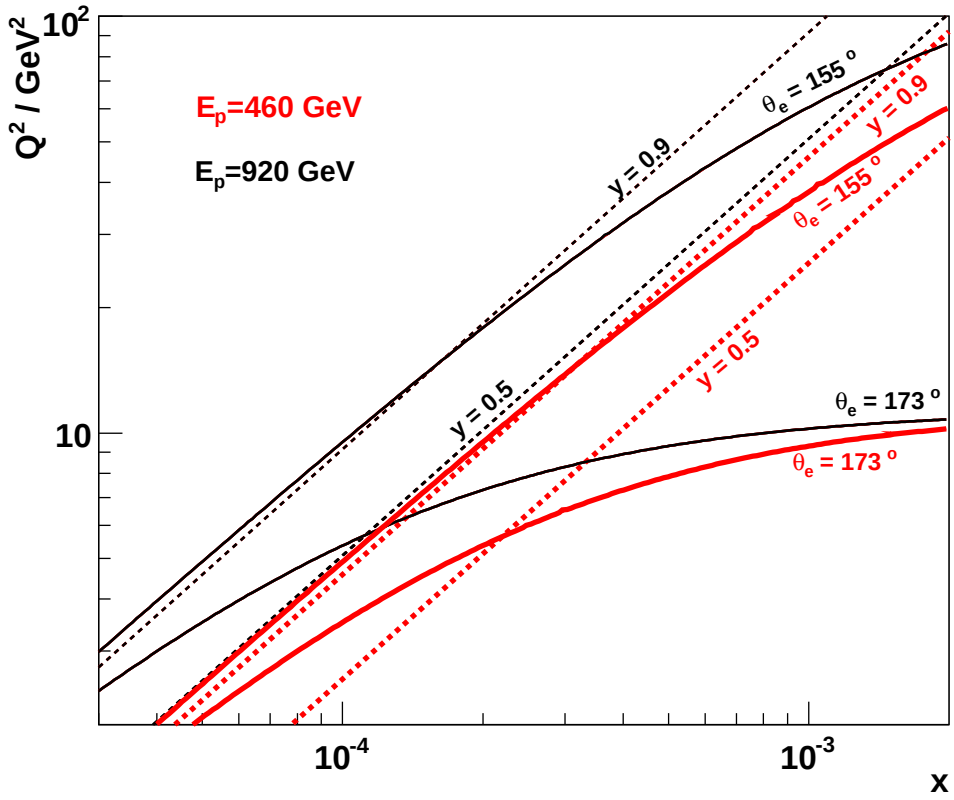

Figure 4.1: Kinematic (x, Q^2) plane, the thicker and lighter lines (red) correspond to the kinematic variable y and the polar angle of the scattered electron for the E_p= 460 GeV sample and the darker lines correspond to the E_p= 920 GeV data.

F_L, H1 can not measure at $y > 0.9$ and at $y < 0.5$ the contribution of F_L to the reduced cross section is negligible. Then one can see that the phase space where F_L can be measured with the scattered electron in the SpaCal is constraint by the highest θ_e value for the E_p = 920 GeV data and the lowest θ_e and the y for the E_p = 460 GeV data.

In this thesis the phase space used will be restricted to low $10 < Q^2 < 120$ GeV^2 and intermediate and low y, $y < 0.6$, where the contribution of background is much smaller and it is possible without major difficulties to study the measurement of the scattered electron energy in the SpaCal and the efficiency of the tracks reconstruction and charge identification with the BST. This information is needed to move towards large y. Moreover this phase space is the adequate to check the relative normalisation between the three data samples in 2007.

Chapter 5

Trigger Analysis

The subtriggers are designed to study different physic processes and therefore they are based on different subdetectors. The triggers analysed in this thesis are based on backward detectors because DIS events with $Q^2 \leq 150$ GeV^2 are characterised by scattered electron detected in the SpaCal calorimeter.

The subtriggers are defined by a logical combination of trigger elements which can be modified. The basic information comes from the energy deposited in the SpaCal cells. This energy deposition defines the bits of the Inclusive Electron Trigger (IET), which is the basis of all trigger elements delivered by SpaCal. IET considers three different energy thresholds denoted as `SPCLe_IET>1,2,3` corresponding to $E'_e > 3, 6, 10$ GeV respectively, it discriminates at L1 between different SpaCal regions. Another element is a radial cut in the position in the SpaCal, the three thresholds are denoted as `SPCL_R20`, `SPCL_R30`, `SPCL_R40`. Despite their names, the shape does not correspond to a circumference, but to a rectangular shape typically smaller than the corresponding radius.

Apart from the trigger elements based on SpaCal information, some subtriggers contain as well information about the BST and the CIP trackers. Here s7 and s8 with BST and CIP information respectively, will be studied. The subtriggers contain as well *global (veto) options* (GO) which are based on *Time-of-Flight* measurements and assumed to be 100% efficient.

The setup of the used triggers is summarised on table 5.1[1]. The subtriggers have slightly complementary properties:

The trigger s0 covers the full phase space needed for the F_L extraction for E_p=920 GeV data and for this analysis, already described in previous chapters. s0 had a low prescale for the low and medium proton beam energy runs, its average prescale for that period was ~ 1, so it provides the best statistical uncertainties. For the period from 10.01.2007 to 13.03.2007 which corresponds to high energy run, the averaged prescale was ~ 1.66. A fiducial cut is

[1] Although no results concerning to s2 are presented in this chapter, the subtrigger s2 is listed because it will be used in section 8.1. Its behavior is similar to s0, except for the higher energy threshold.

Table 5.1: Definition of the subtriggers used in this analysis during the period 2006-2007

Subtrigger	*Definition*
s0	(SPCLe_IET>1) && (SPCL_R20)
s2	(SPCLe_IET>2)&& (SPCL_R20)
s3	(SPCLe_IET>2)&& (SPCL_R30)
s7	(STT_R_gt_20&&STT_Spac_BST) && (SPCLe_IET>0)
s8	(SPCLe_IET>0) && (SPCL_R20)&& (CIP_T0)

derived based on the s0 performance, the inner region of the SpaCal is excluded from the element SPCLe_IET>1. This cut is applied for the selection in chapters 8 and 9.

The trigger s3 has, like s0, high efficiency but it does not cover the whole radius in the SpaCal due to the element SPCL_R30. However, it had a lower averaged prescale than s0 for the high energy running period mentioned, close to 1, so it improves the statistical uncertainties.

The trigger s7 and s8 have the lowest energy threshold, they allow to study scattered electron energies down to $E'_e = 3$ GeV, $y \sim 0.9$, which is fundamental for the F_L measurement. s8 triggers on the energy of the cluster plus a track in the CIP, which can be produced by the hadronic final state or the scattered electron. s7 triggers on a track originated from the scattered electron in BSTT matching to a cluster in the SpaCal in the same ϕ region. s7 is defined by a *SpaCal Topological Trigger* (STT) element. These elements are aimed for the low energy running due to its lower energy threshold. With the STT the decision in the position in the SpaCal is moved from the trigger level L2 to level L1 to gain decision time. The identification of charged and neutral particles in SpaCal at L1 trigger level is done using the topology matching between the BST ϕ sectors and SpaCal.

5.1 Trigger Efficiency

In general the efficiency for one selection criterion is defined by

$$\varepsilon_{sel} = \frac{N_{sel}}{N_{ref}} \tag{5.1}$$

where N_{ref} are the events satisfying every criteria except the one under study and N_{sel}, the events which also satisfy the selection. In this case, the efficiency of a subtrigger is given by the fraction of DIS selected events triggered by the subtrigger over the total of DIS events which passed the selection.

To study a subtrigger it is necessary to set the reference triggers. To study s0 and s3, which are SpaCal triggers, a combination of independent subtrigger without SpaCal conditions was used. The subtrigger s7 (s8) was studied using s8 (s7) as a reference. This allows

to study only the non-SpaCal components of the subtriggers, studying s8 is equivalent then to study `CIP_T0` and s7 is equivalent to analyse BSTT. The study was done for the three data sets of 2007. The efficiency can be studied for different variables, such as energy of the scattered electron, radius on the SpaCal plane or as a function of time.

The selection applied for E'_e and R_{SpaCal} was modified for each subtrigger to adjust it to the different thresholds and detector acceptances. The selection for the reconstructed vertex was as follows: A central vertex was required in every case. For the subtriggers s0 and s3, if there was no central vertex, a vertex reconstructed by the FST or the CIP was selected. For the s7 and s8 studies, a selection independent of the CIP it was needed, because it is already involved in the definition of s8, used as well as a reference for s7. The cut in the vertex position was the standard $-35 < z_{vtx} < 35$cm.

The subtrigger s7 contains information about the BST detector so a "Non vertex fitted track" reconstructed by the BST is required, see section 6.2.1. The following cuts were applied for s7:

- Match of the extrapolated track to a cluster in the SpaCal: The distance between the cluster and the extrapolated track in the z-position of the cluster was required to be smaller than 2cm.

$$\left|\sqrt{(x_{cl}-x_{track})^2-(y_{cl}-y_{track})^2}\right|_{z=z_{cl}} < 2 \quad \text{cm} \tag{5.2}$$

- Cut in BST acceptances: Taking into account the coverage of the BST a cut in ϕ and R_{BST}. The latter is measured in the $z_{BST} = -48$ cm plane, which is the centre of the BST in the H1 coordinates. It corresponds to the distance from the H1 z-axis to the (x, y) position of the straight line between the central vertex to the cluster.

$$R_{BST} = \sqrt{x^2_{z_{BST}} + y^2_{z_{BST}}} \tag{5.3}$$

  It is defined in the H1 coordinates, otherwise it would be ϕ-dependent. The cut was set to $5 < R_{BST} < 10$ cm. The BST does not cover the whole 2π then a cut $-2.5 < \phi < 2.5$ rad was chosen.

In figure 5.1 the efficiency is presented as a function of E'_e, r_{SpaCal} and ϕ measured by the SpaCal. The distributions correspond in this case only to the low energy running period, but the results are equivalent for the other two runs. The difference in the efficiency between the three periods is negligible. For s0 and s3 it is in the per mil level and the biggest differences for s7 and s8 are not greater than 0.1%.

The efficiency of the triggers s0 and s3 as a function of the energy and radius in the SpaCal is, above the threshold, about 99.9% and constant for the whole range. Although for each cell the change from negative decision to positive decision of the subtrigger should be a step function, one can see the "turn on" in the efficiency. The efficiency of s8 is 98.5%, one can see that also at small radius and energy values the efficiency has the same value. The efficiency

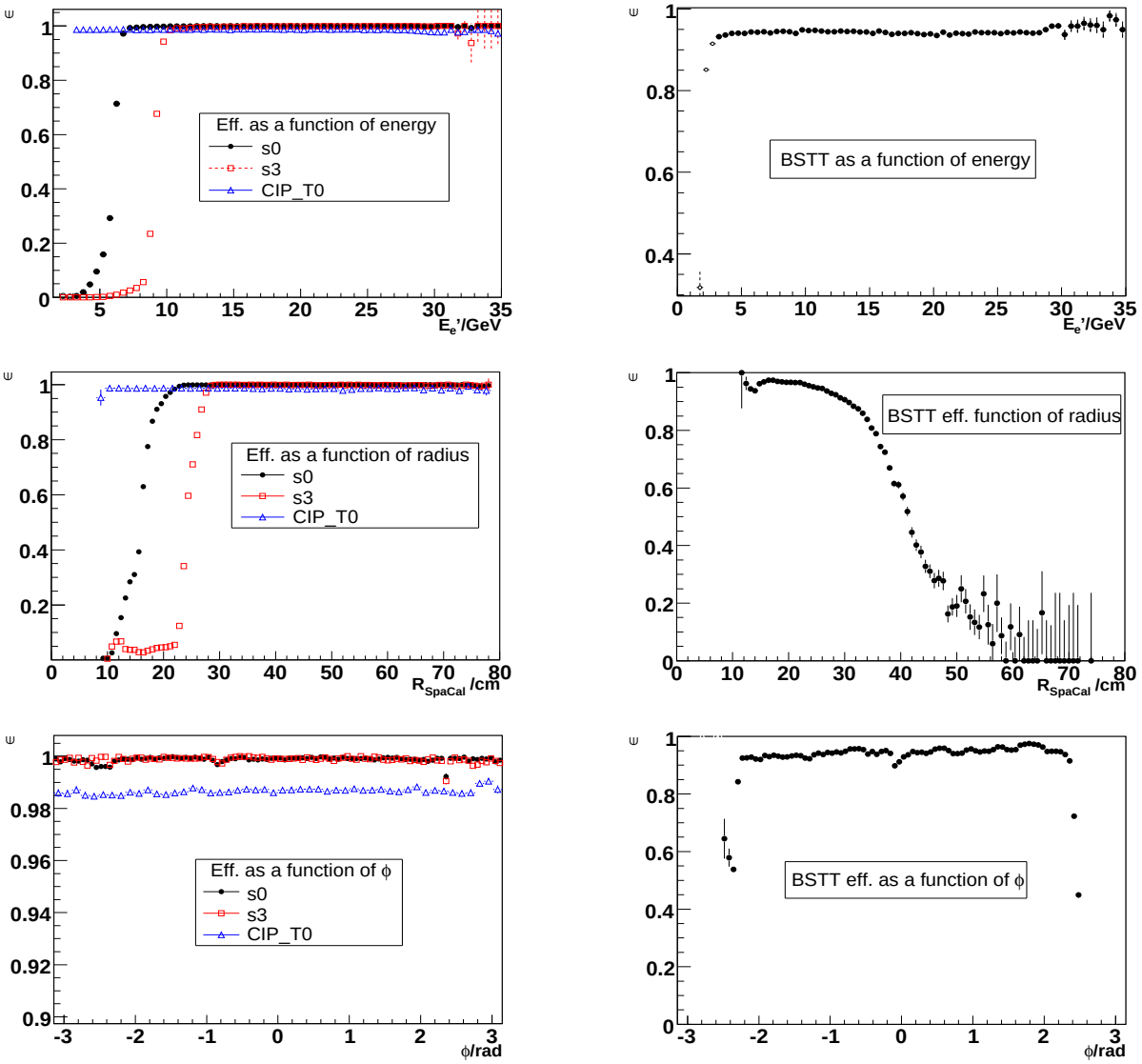

Figure 5.1: Efficiency of the four subtriggers selected as a function of the selected electron energy E'_e, its radius on the SpaCal plane r_{Spac} and ϕ for the low energy data. On the left side, the solid circles correspond to the s0 efficiency, the open squares to s3 and the triangles to the CIP_T0. On the right side the corresponding distributions for the BSTT are shown.

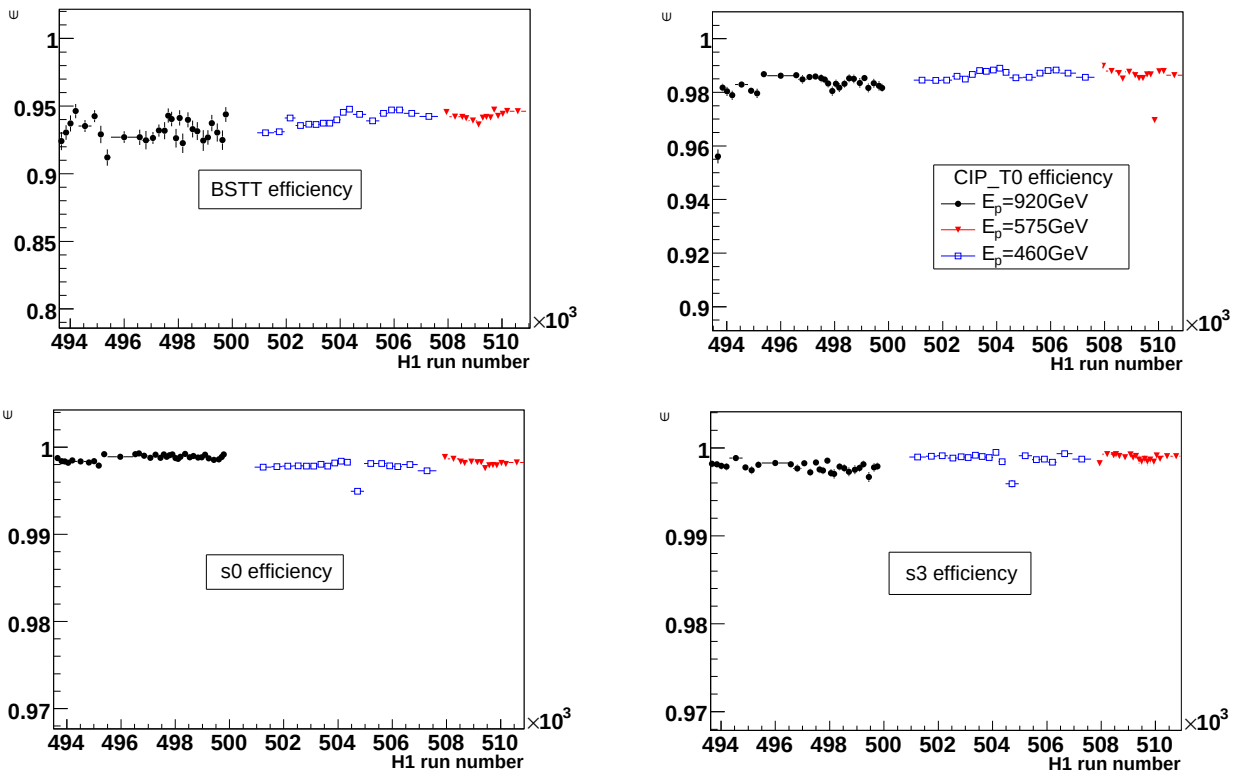

Figure 5.2: Efficiency of the non SpaCal components of the subtriggers s7 and s8 and the subtriggers s0 and s3 as a function of the H1 run number (from right to left and from top to bottom). The closed circles correspond to the high energy, the open squares to the low energy and the triangles to the low proton beam energy.

of s7 is lower than for the rest and it is not efficient in the whole SpaCal. The efficiency for radii between 15 and 35 cm is about 94% and then decreases where the BST does not cover the SpaCal.

Figure 5.2 shows the efficiency of the different subtriggers as a function of the H1 run number. The efficiency of the subtriggers s3 and s0 is greater than 99.8% for the three periods. The efficiency of the subtrigger s8 is, also for the whole data considered, about 98.2%. The lowest efficiency corresponds to the s7 subtrigger, about 94%. During the high proton beam energy running the s8 subtrigger had a high prescale, therefore the statistical uncertainties are bigger than for the other two periods, as it is shown in the plots corresponding to s7 and s8. One can also see that the s7 efficiency has a certain dependence on the luminosity fill, it varies about 2%.

The lower efficiency of s7 comes from the difficulty of doing online noise rejection in the silicon signals. For the measurement of F_L the subtriggers s8 and s7 will be combined to compensate it. The s8, the `CIP_T0`, triggers at high SpaCal radius the electron and at lower the hadronic final state and s7 triggers only the scattered electron, it does not depend on the hadronic final state.

Chapter 6

Vertex Reconstruction and Efficiency of CIP and BST

In this chapter the performance of the CIP and the BST detectors is presented. Both detectors can be used to reconstruct the event vertex just from the scattered electron and they are therefore convenient to study DIS processes. Moreover the BST detector also measures the charge of the track which helps to identify the scattered electron.

The alignment of the CIP detector with respect to the central tracker and the vertex reconstruction, which is used for the DIS event selection, will be studied. The efficiency of the BST as a function of different parameters is also studied.

6.1 CIP Vertex Reconstruction

To study the performance of the Central Inner Chamber no trigger selection was applied to have the maximum statistics. The energy of the scattered electron was required to be $E'_e > 15$ GeV and the standard electron identity cuts were applied. The distribution corresponding to the reconstructed CIP vertices was compared to the one corresponding to vertices reconstructed by the central tracker or FST (to increase statistics).

The efficiency of the CIP is defined by at least three CIP hits linked to the electron track, which is to a first approximation defined by the SpaCal cluster and the nominal vertex position. Since each part of the detector covers a limited region, it is necessary to establish a certain selection taking into account its acceptance. In this case, a cut in the radial position of the track in the CIP was set, $R_{CIP} > 19$ cm. This radial position is defined as

$$R_{CIP} = (z_{CIP} - z_{cnt}) \cdot \tan\theta_e \tag{6.1}$$

where z_{CIP}=-112.5 cm is the z-position of the CIP closest to the SpaCal in the H1 coordinates, z_{vtx} is the z-position of the central tracker and θ_e is the polar angle of the scattered electron.

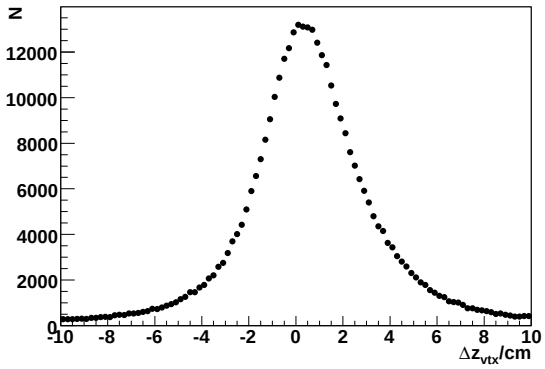

Figure 6.1: Difference in the z-position of the vertex of the central vertex and the CIP vertex

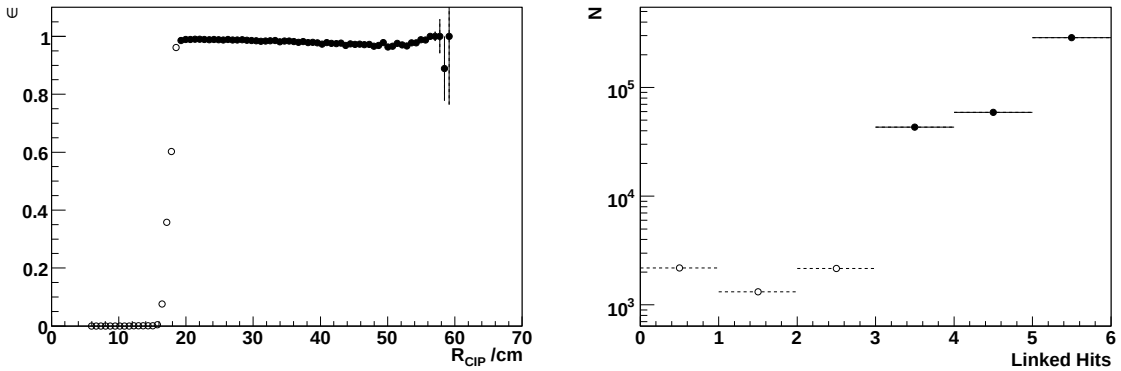

Figure 6.2: On the left hand side the efficiency of the CIP as a function of the so-called R_{CIP} is shown. On the right hand side the distribution of the number of linked hits is presented.

Figure 6.1 shows the difference between the vertex reconstructed by the central tracker and the CIP, $\Delta Z_{vtx} = z_{cnt} - z_{CIP}$. One can see that the vertex reconstruction by the CIP is correct, most of the events have a deviation smaller than 3-4 cm, fitting the curve with a Gaussian in the interval (-3,3) the value of σ is 2 cm and the offset is about 0.4 cm.

In figure 6.2 the efficiency of the CIP as a function of R_{CIP} is shown. After the cut in R_{CIP}, its value is 98,8% for the whole data taking in 2007. On the right hand side of the figure the distribution of the number of linked hits is shown. Requiring a minimum value of three hits, the efficiency of the cut is high and it avoids the selection of more noise unnecessarily.

In figure 6.3 the efficiency as a function of the luminosity run number is presented. The dependence of efficiency on the proton beam energy is negligible, the average for the high and intermediate energy runs is higher than 98.7% and for low energy run it is around 0.2% lower. This difference could be due to the variation of the efficiency within a luminosity fill, which is about 1%.

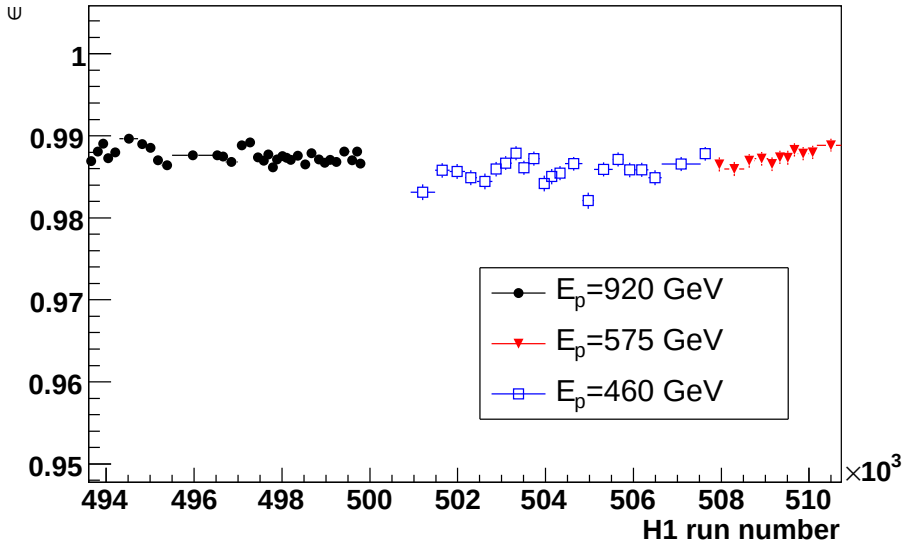

Figure 6.3: CIP efficiency as a function of the luminosity run for the three energy runs.

6.1.1 CIP Alignment

The reconstructed vertices selected in most of the results in this thesis are the central and the CIP vertex. In order to measure precisely θ_e, which is a basic quantity to reconstruct the kinematic variables, the CIP should be correctly aligned with respect to the central tracker, which defines the reference in H1.

Figure 6.4 shows the difference between the polar angles measured with the central chamber and the CIP, $\Delta\theta = \theta_{cnt} - \theta_{CIP}$ as a function of the azimuthal angle ϕ_e measured with the SpaCal. On the right side of the figure the circles represent the mean values of Gaussian fits performed to the quantity $\Delta\theta$ in slices of ϕ_e. The sinusoidal shape indicates a shift of the detector in the $x - y$ plane. To determine the shift, the distribution was fitted with the functional form proposed in [23]:

$$\Delta\theta = p_0 \cdot \sin(\phi_e - p_1) + p_2 \tag{6.2}$$

where p_0 corresponds to an absolute value of the shift in the x-y plane, p_1 corresponds to the direction of that shift and p_2 to the z displacement of the CIP detector. In table 6.1 the parameters of the fit are listed. The most relevant one is the first parameter, the shift in (x,y) thus the aim of the correction will be to minimise it. There is some structure due to local features which is independent of the global alignment. The alignment applied was $y = -0.17$ cm. In figure 6.5 the distributions after applying the alignment are presented. The values of the parameters are also presented in the table 6.1. There is still a sinusoidal shape but this dependence in ϕ is within 1 mrad uncertainty. In principle, the distribution should be centred in zero but there is a small shift to positive values of $\Delta\theta$. The third parameter, $p2$, is also significant. However, the value of the offset with and without the alignment is small,

Table 6.1: Parameters of the fit $\Delta\theta = p_0 \cdot \sin(\phi_e - p_1) + p_2$.

Parameter	Before alignment	After alignment
p0	$(-1.717 \pm 0.002) \cdot 10^{-3}$	$(2.12 \pm 0.05) \cdot 10^{-4}$
p1	0.105 ± 0.004	-0.76 ± 0.02
p2	$(7.43 \pm 0.002) \cdot 10^{-4}$	$(7.22 \pm 0.03) \cdot 10^{-4}$

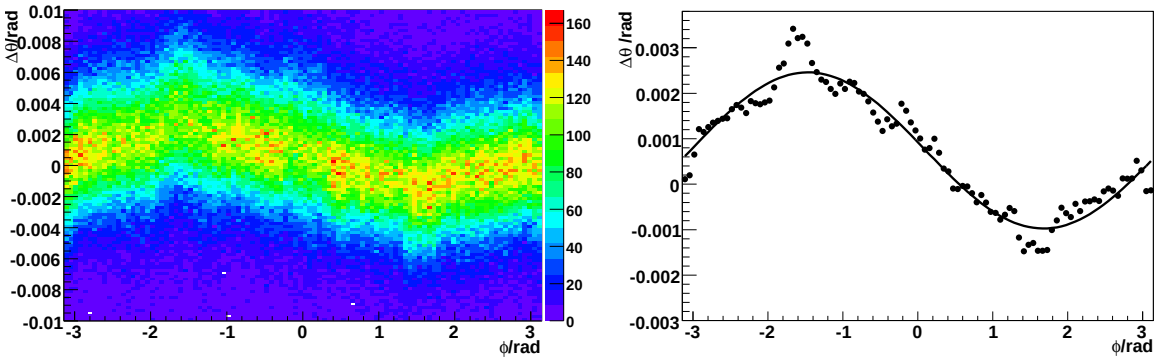

Figure 6.4: Difference between the polar angle from the central tracker and the CIP as a function of ϕ without any alignment. On the right side, the mean values of gaussian fits performed to $\Delta\theta$ are shown.

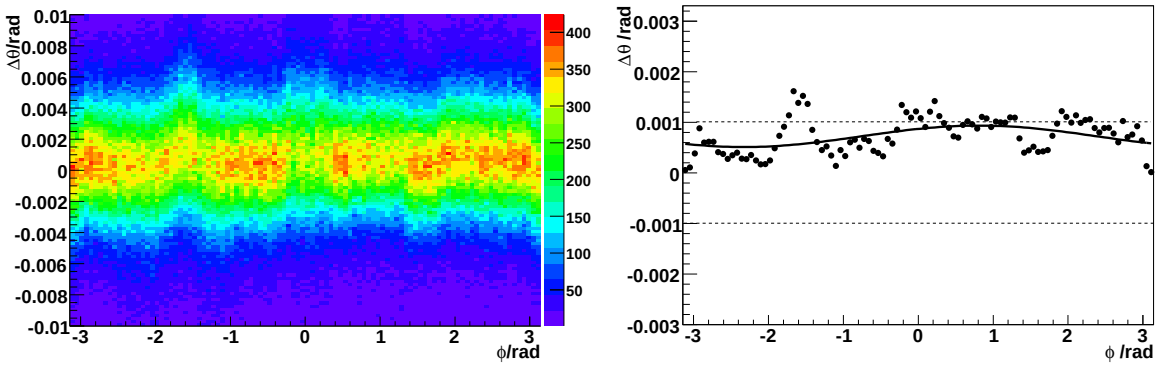

Figure 6.5: Difference between the polar angle from the central tracker and the CIP as a function of ϕ applying the alignment.

its order of magnitude is 10^{-4}. The systematic errors are high enough to cover the observed shift, so no further studies have been carried out.

Table 6.2: Modified cut in BST acceptance

ϕ/rad	minimum R_{BST}/cm
$-2.3 < \phi < -0.2$	6.0
$-0.2 < \phi < 0.8$	6.5
$0.8 < \phi < 2.3$	6.0

6.2 Electron Tracking with the BST

The BST detector will be fundamental for the measurement of the longitudinal proton structure function so it is important to check its performance. It is the only detector which is able to measure the electron track at low Q^2 so it complements the vertex reconstruction of other track detectors. At high y, it helps to distinguish photoproduction background thanks to the track charge identification. In this section the BST tracking efficiency is obtained for the three runs in 2007. The BST efficiency is also compared to the efficiency in Monte Carlo.

6.2.1 BST Efficiencies

The general selection applied was similar to the one of the previous section. The selection concerning the BST detector, related to the reconstructed tracks and the coverage of the BST, which was introduced in 5.1 is used.

There are two kinds of tracks reconstructed by the BST implemented in the H1 software. The tracks known as "Non vertex fitted tracks" are first reconstructed from the BST hits. Then, these are fitted to the expected beam position determined by the central tracker and they are referred to as "Vertex fitted tracks". Both cases are studied here. To select a track, the requirement was the match, in the $x-y$ plane, of the extrapolated track to the z position of the cluster within 2 cm distance.

Taking into consideration that the extrapolated track must be within the acceptance of the BST, cuts in ϕ and R_{BST}, like in section 5.1, were introduced. The latter cut was set to $6 < R_{BST} < 11$ cm. [1]

The efficiency of linking a cluster in the SpaCal with a track from the BST as a function of ϕ is not constant for the whole region, see figure 6.6, closed circles. Independently of the type of tracks, it drops approximately 20% between $0 < \phi < 0.8$ rad. This is a consequence of a known hardware defect in the sectors corresponding to that ϕ-range. To try to increase the efficiency instead of using the described independent cuts for R_{BST} and ϕ, a combined cut in the (R_{BST}, ϕ) plane was introduced. The cut in ϕ was tightened with respect to section 5.1, $\phi < 2.3$ rad and the lower limit of R_{BST} was modified depending on ϕ, see table 6.2.

[1] The cut in R_{BST} is different to the one in section 5.1 because in that case the BSTT is used, which has only four planes in contrast to the BST which has six.

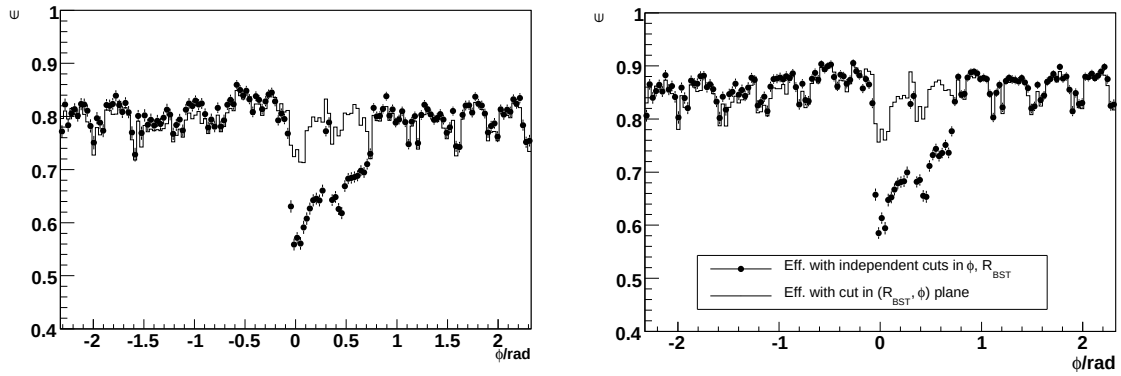

Figure 6.6: Efficiency of linking a cluster in the SpaCal with a vertex fitted track from the BST (left side) and a non vertex fitted track (right side) as a function of ϕ. The closed circles represent the efficiency with the initial cuts in R_{BST} and ϕ and the open histogram the improved efficiency with the cut in the plane (R_{BST}, ϕ).

Table 6.3: Efficiency of the BST as a function of the luminosity run

Track& period	High energy run	Medium energy run	Low energy run
Vertex Fitted Tracks	78.98 ± 0.03	78.6 ± 0.2	79.5 ± 0.1
Non Vertex Fitted Tracks	84.59 ± 0.02	84.5 ± 0.2	85.44 ± 0.08

Applying the new cut the efficiency of the problematic region in ϕ improves, see figure 6.6 open histograms. The global effect of the new cut is a 4% increase in the efficiency for both non vertex and vertex fitted tracks. The efficiency with non vertex fitted tracks changes approximately from 80% to 85% and with vertex fitted tracks from 75% to 79%. The plots correspond only to the low energy run but the improvement affects in the same way the high and medium energy runs.

The BST, see section 3.2.2, is composed of 12 ϕ-sectors each one covering 22.5%, approximately 0.4 rad, so one can see that the structure in the distributions in figure 6.6 corresponds to the different sectors. The efficiency is higher at the centre of the sectors and between 5-10% lower at the sector boundaries. This feature may indicate a problem with the alignment as it is mostly absent in the MC simulation, see below.

In figure 6.7 the efficiency as a function of time is presented for the three data samples. The efficiency is reasonably constant for the three periods except for a short period for the high energy sample where the efficiency drops by 10%. This is a known problem, between the H1 run numbers 495031 and 495400 two sectors of the BST did not work. The averaged values are listed in table 6.3. The average for the high energy run is obtained excluding the runs where not all the sectors worked. In every case the efficiency for the non vertex fitted tracks is 5-6% higher than for vertex fitted tracks.

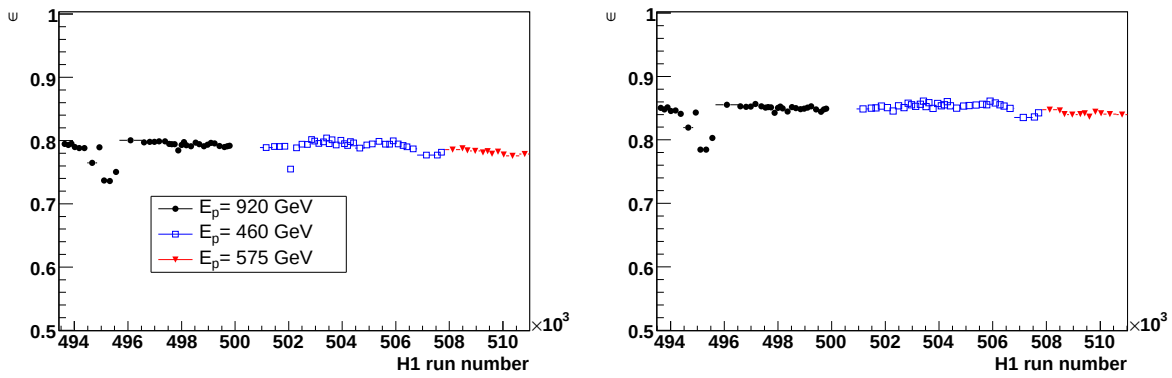

Figure 6.7: Efficiency of BST as a function of luminosity run for vertex fitted (left) and non vertex fitted tracks (right). The closed circles correspond to the efficiency during the high energy run in 2007, the open squares to the low energy run and the inverted triangles to the medium energy run.

The BST detector has a small acceptance and it is important to test that the cuts are correct. This can be done by determining the efficiency with a MC simulation. In this case the comparison was done with data and MC corresponding to $E_p = 460$ GeV. The MC simulation used is this thesis is described in section 9.1 so no details about its characteristics are now commented. Running the same algorithm for data and Monte Carlo the efficiencies can be compared. In principle, the efficiency for data and MC should be the same, which is necessary to obtain the cross sections. However, figure 6.8 shows that the efficiency of linking a track for the MC simulation is clearly higher than the efficiency for data, which means that the MC simulation has to be improved to model the efficiency of the BST. The efficiency for the MC does not depend on the type of track, it is about 90% for both non vertex and vertex fitted tracks, 10% higher than in data for vertex fitted tracks and 5% higher for non vertex fitted tracks. The efficiency differs as well as a function of R_{BST}: For MC it does not depend on R_{BST}, as the plateau region was chosen, while for data there is nearly a 10% difference between the efficiency corresponding to R_{BST} values close to the limits of the cut and the central values. The efficiency of the MC also shows the problem with the boundary sectors but the effect is smaller than for data, it drops only by 3%. The reason may be the increased dead material at the sector boundaries or deficits in the reconstruction algorithm.

6.2.2 Charge Identification with the BST

The BST detector can not only perform track reconstruction but also allows to identify their charge and to measure the momentum. This is a valuable tool to identify and reject background at low scattered electron energy. One way to study it is to compare the SpaCal energy measurement with the track curvature measurement from the BST, which gives the information about the momentum and the charge of track. The momentum and the energy values should be the same and for positrons the charge identified should be positive.

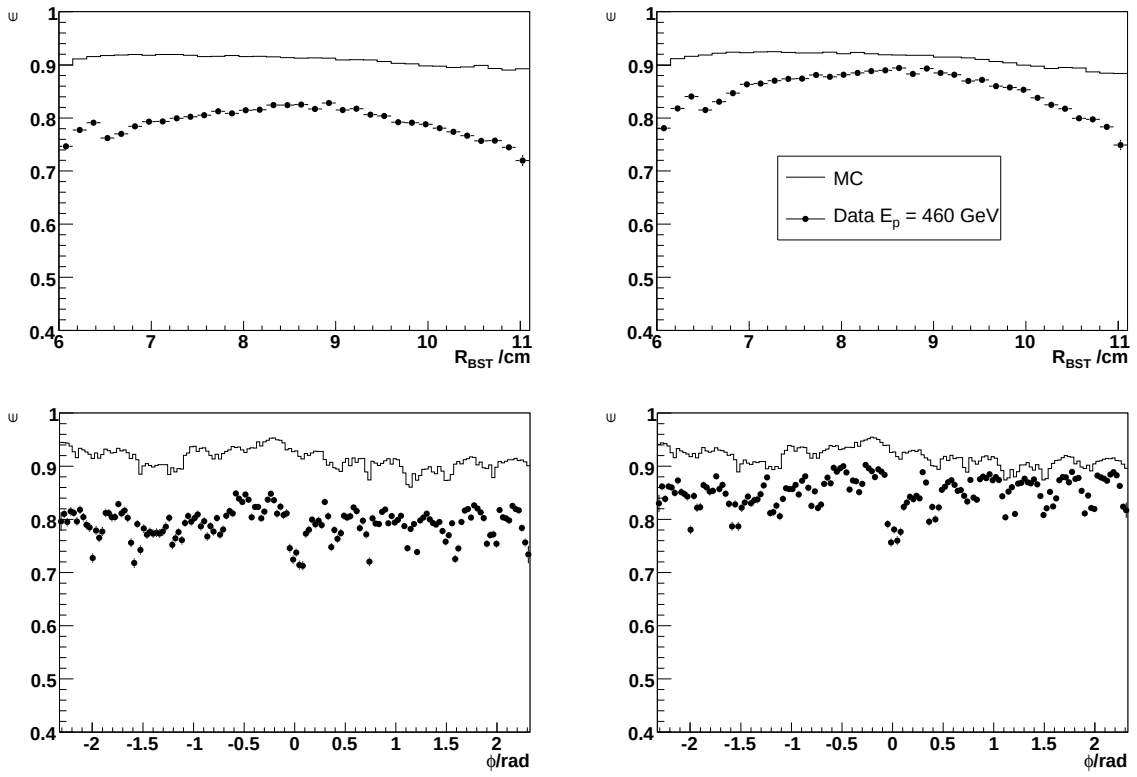

Figure 6.8: Efficiency as a function of R_{BST} and ϕ for data and MC for the low energy beam sample for vertex (left) and non vertex fitted tracks. The circles are the experimental data and the open histogram is MC simulation.

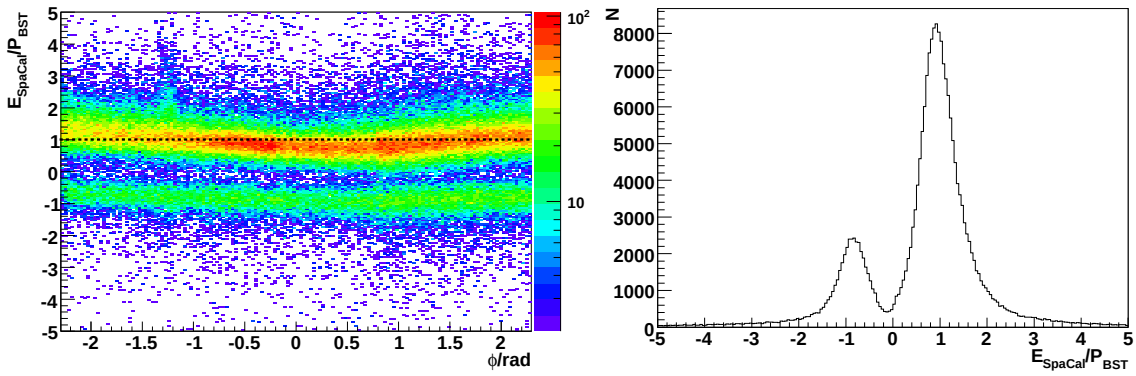

Figure 6.9: Distribution of E_{SpaCal}/P_{BST} as a function of ϕ for $E'_e < 15$ GeV. On the right hand side the projection is shown.

In figure 6.9 the ratio between the energy measured by the SpaCal and the momentum multiplied by the charge of the track measured by the BST as a function of ϕ measured with the SpaCal for non vertex fitted tracks is shown. The energy of the scattered electron is taken $E'_e < 15$ GeV in order to study the contribution of the background and to avoid the region of worse BST resolution. The dotted line corresponds to $E_{SpaCal}/P_{BST} = 1$. Although the distributions should not depend on ϕ, there is a clear dependence. It is shifted to values smaller than one at small ϕ and it increases at greater ϕ. It can be inferred that the BST has a problem with the alignment.

On the right hand side of the figure, the projection over E_{SpaCal}/P_{BST} is presented. The distribution shows the expected peak at $E_{SpaCal}/P_{BST} = 1$ since the scattered leptons are positrons and a secondary peak at -1, which is mostly due to background. The immediate consequence of the alignment problem is that "wrong charged events" can not be identified as background, a fraction could be due to a wrong reconstruction.

Chapter 7

SpaCal Calibration

The resolution of the reconstruction methods relies on the precision of the measurements of the angles and energies of the scattered electron and hadronic final state. Since the energy measurement enters directly to the kinematics, it is necessary to perform a precise calibration of the energy measured by the SpaCal calorimeter on the analysis level.

The energy measurement in each of the 1192 cells of the SpaCal is performed using photomultiplier tubes individually for each cell whose gains can vary with time. This variation is measured with the help of a LED calibration system situated at the back side. Each photomultiplier receives well defined constant light pulses and the photodiodes are used to identify instabilities of the LED intensity. These are read out to the data base and afterwards an offline correction of the multiplier gain is performed.

A precise calibration on the analysis level is provided by a method proposed in [23] which is described in more detail in [26]. It uses the scattered electron reconstructed with the "double angle method" as a reference. This reconstruction method expresses the kinematic variables y, Q^2 as a function of the polar angles of the scattered electron, θ_e, the hadronic angle, θ_h, and the electron beam energy E_e:

$$y_{DA} = \frac{\tan(\theta_h/2)}{\tan(\theta_e/2) + \tan(\theta_h/2)} \tag{7.1}$$

$$Q^2_{DA} = 4E_e^2 \frac{\cot(\theta_e/2)}{\tan(\theta_e/2) + \tan(\theta_h/2)}. \tag{7.2}$$

The energy of the scattered electron is given by:

$$E_{DA} = E_e \frac{1 - y_{DA}}{\sin^2(\theta_e/2)}. \tag{7.3}$$

The E_{DA} can be reconstructed in the kinematic peak region, $E_e \sim 27.6$ GeV very precisely, that is the reason why it can be used as reference for the calibration as absolute scale. The selection applied is the following: Events at low y are selected applying a cut on the hadronic angle $\theta_h < 80°$ allowing a maximum value of $y < 0.15$ and a lower limit $\theta_h > 15°$, which

suppresses the influence of events where the hadronic final state escapes often undetected in the forward direction. A cut on the difference of $|y_h - y_{DA}|/|y_h + y_{DA}| < 0.2$ was used to reject events with wrongly reconstructed y, usually due to noise in the LAr calorimeter. In order to minimise contributions of photoproduction background events, only events with one cluster in the SpaCal with an energy in the kinematic peak region $20 < E'_e < 32$GeV are accepted. A cut on the SpaCal radius, distance of the cluster to the beam pipe, $R_{SpaCal} > 12$ cm was set to avoid the effects of leakage along the beam pipe. In addition, a fiducial cut at high SpaCal radius, $R_{SpaCal} < 73$ cm is also selected. It removes events in the acceptance edge of the SpaCal. There is no trigger selection in order to maximise the statistics.

To ensure homogeneity over the whole calorimeter plane the following calibration factors are applied:

1. Gain calibration factors for each cell of the calorimeter.
2. Inbox calibration factors which correct for the energy losses due to the SpaCal cell module geometry.
3. Cracks and radial calibration factors, corrections due to the supermodule geometry of the SpaCal and as a function of the transverse distance to the centre of the beam pipe.

These factors are applied sequentially to the uncalibrated energy to both data and MC.

7.1 Cell Gains

The gain of each calorimeter cell is calculated using an iterative procedure. For each event, the event pull (event "miscalibration") is introduced:

$$\delta_{ev} = \frac{\sum_{ic} E^{ev}_{ic}(1 + \Delta^{it} g_{ic})}{E^{ev}_{DA}} = \frac{E^{ev}_{cluster}}{E^{ev}_{DA}}. \tag{7.4}$$

E^{ev}_{DA} defines the energy scale of the event to which the calibration is performed and E^{ev}_{ic} the energy measured by the cell ic for the event ev, it includes all corrections done before the final calibration. $\Delta^{it} g_{ic}$ is the correction to the amplification gain of the cell ic and it denotes the iteration number with $\Delta^1 g_{ic} = 0$ for the first iteration.

The relative contribution of the cell j to the event pull is given by:

$$w^{ev}_j = \frac{E^{ev}_j(1 + \Delta^{it} g_j)}{E^{ev}_{cluster}}. \tag{7.5}$$

The sum of the weights for any event is equal to 1. The weighted pull average over all the events except the outliers was calculated and the correction of all cell amplification gain factors was determined as

$$\Delta^{it+1} g_j = \Delta^{it} g_j - (\overline{\delta_{ev} w^{ev}_j} - 1). \tag{7.6}$$

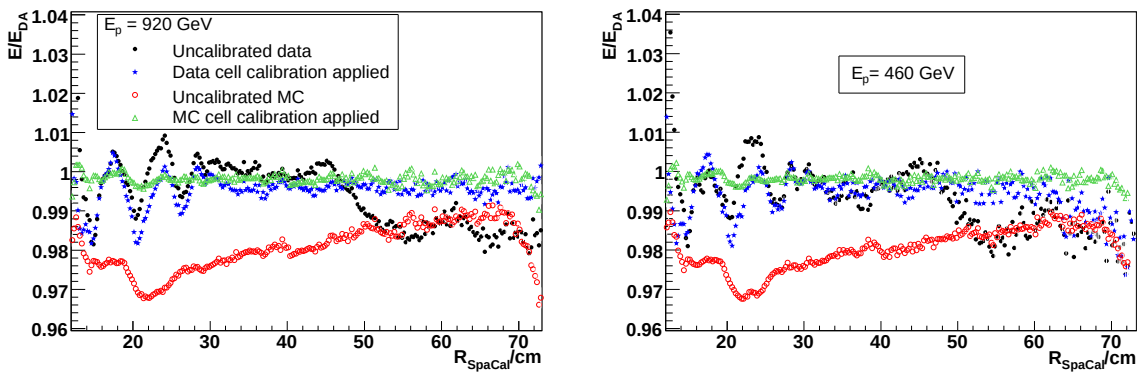

Figure 7.1: Uncalibrated and calibrated (only cell gain factors applied) E_{SpaCal}/E_{DA} for data and MC for the high and low proton beam energy periods.

The process is iterated until the maximum $\overline{\delta_{ev} w_j^{ev}}$ is smaller than 0.002 or the average change for all cells in the SpaCal with good statistics is smaller than $3 \cdot 10^{-4}$,

$$\frac{\sum_j \overline{\delta_{ev} w_j^{ev}}}{N_{cells}} < 3 \cdot 10^{-4}. \tag{7.7}$$

In figure 7.1 the variation of E_{SpaCal}/E_{DA} as a function of the distance of the cluster to the centre of the beam pipe (R_{SpaCal}) for the uncalibrated distribution and after applying the cell gains is presented. The left distribution corresponds to the high energy proton beam data and MC the right one to the low energy proton beam run. The gain factors correct the energy measurement by 1% to 2%. The remaining variations are minimised by the following steps.

7.2 Inbox Corrections

The energy losses are also investigated as a function of the cluster position relative to the centre of the cell with the largest energy deposition. The measurement of the energy is corrected as function of the impact point of the electron candidate inside the cell. The coordinates of the hottest cell are used to determine its position. The cells are divided in a grid with spacing of 2 mm. This correction, the so-called inbox correction [26], is derived using the same selection as for the cell calibration and with the same fit procedure.

7.3 Cracks and Radial Corrections

Another source of energy losses comes from the inhomogeneity of the SpaCal cells due to the supermodule structure, the SpaCal calorimeter is constructed in supermodules containing 16 cells, energy losses due to the dead material present between the supermodules are expected.

The corrections are derived as a function of x_{SpaCal}, y_{SpaCal} comparing the double angle energy with the SpaCal energy calibrated with cell gains and inbox corrections.

The last calibration factor is applied as a function of the measured radius R_{SpaCal}. It should correct the possible influence of the dead material located in front of the SpaCal.

The resolution for the Monte Carlo sample is better than the resolution for data, therefore it is necessary to smear the reconstructed energy of the MC so the kinematic peak becomes wider. The correction was done by applying an additional Gaussian smearing, resulting 2% for low energies and smaller above E'_e=23.5 GeV. Finally, a correction for the nonlinearity of the SpaCal described in [26] was applied to the MC. The correction is about 3% at E'_e=1 GeV and linearly extrapolated to higher values of the energy, in the kinematic peak the correction is zero.

In figures 7.2 and 7.3, the comparison for the two sets of data and MC calibrated and uncalibrated is shown. The distributions are normalised to area so the effect of the calibration is better visible. The selection is not the special selection for the DA calibration but the nominal DIS selection described in section 4.3. Before applying any calibration, plots on top of the figure, there is a shift in the E'_e kinematic peak between MC and data as well as difference in the resolution. Once the calibration is applied, plots on the bottom part of the figure, the MC distribution describes correctly the behaviour of the data. While the E'_e spectrum can be influenced by the used PDFs in MC, $E - p_z$ is more independent of the used structure functions, the position of the peak is determined by the longitudinal momentum balance. One can see that also for the latter the peak is around $2E_e$, in the same position for MC and data after the calibration.

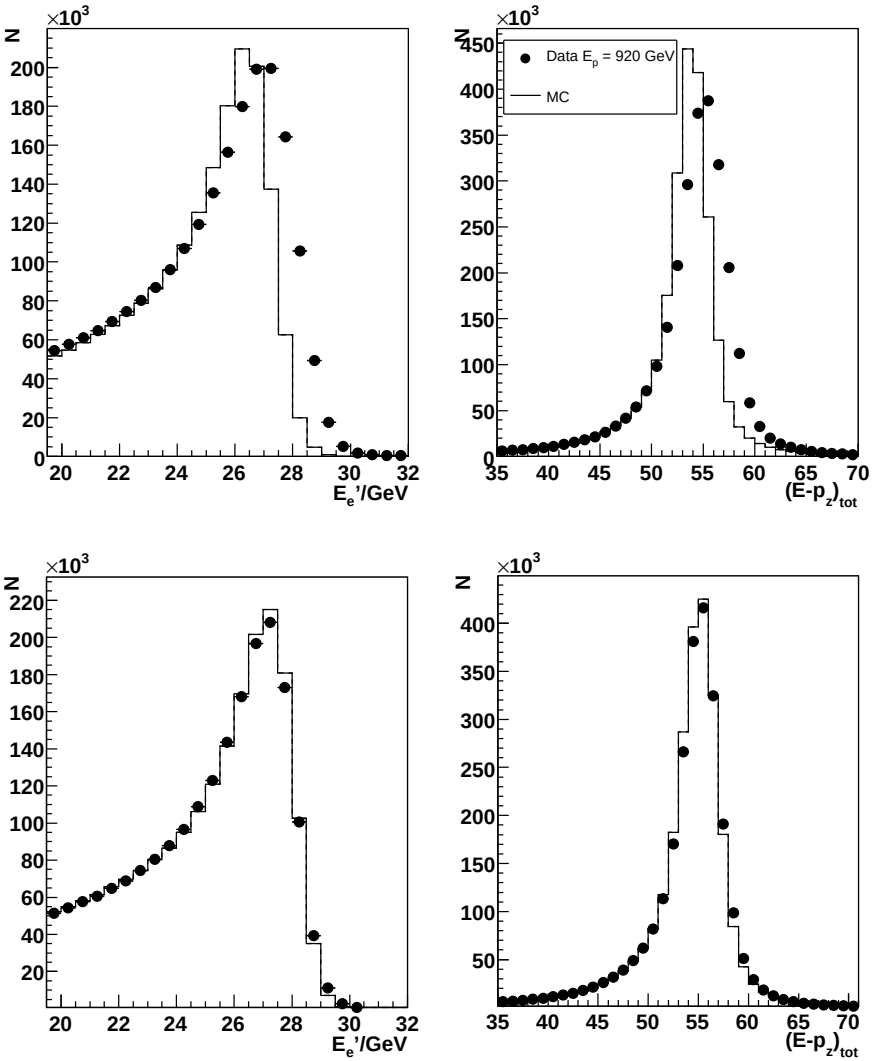

Figure 7.2: Uncalibrated (top figure) and calibrated distributions (bottom) for the high energy running period in 2007. On the left side the energy of the scattered electron is presented and on the right side, $E - p_z$.

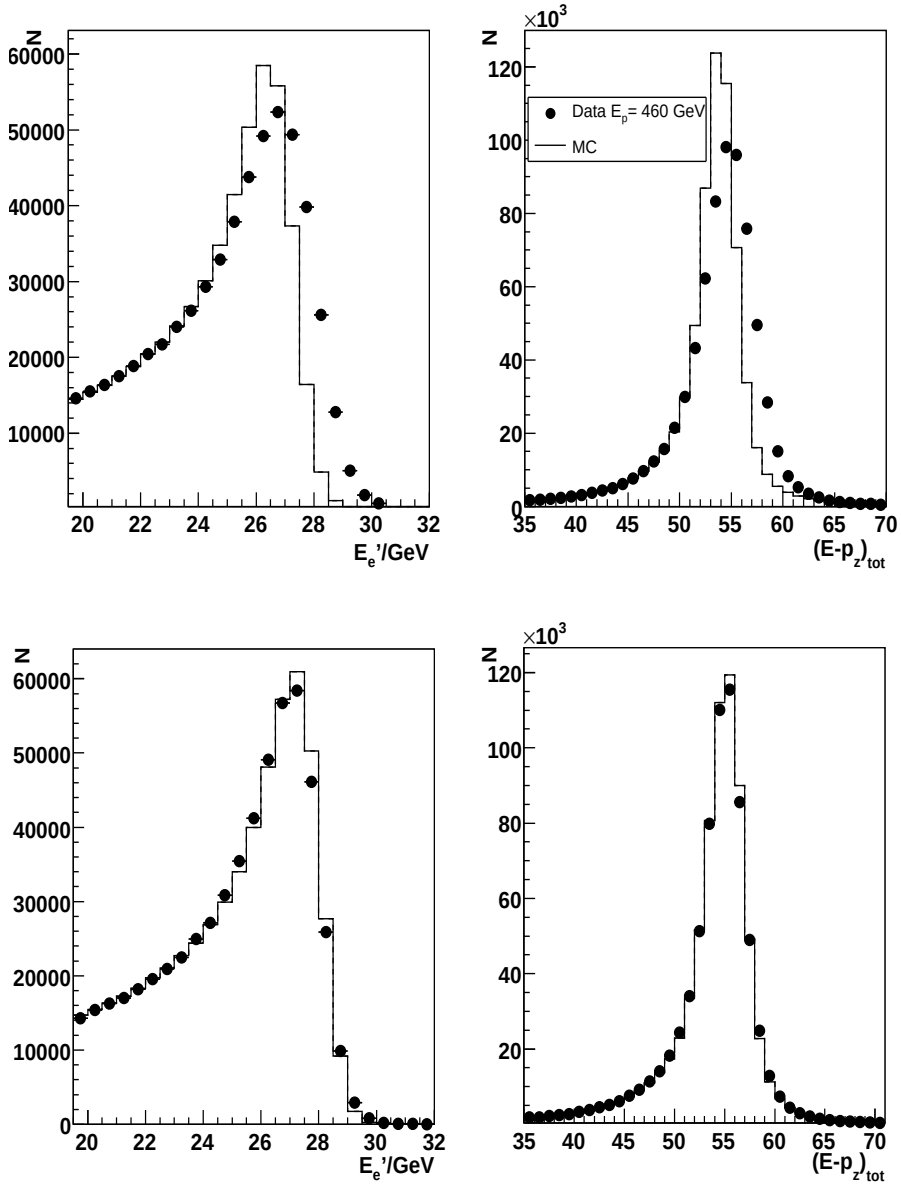

Figure 7.3: Uncalibrated and calibrated E'_e (left) and $E - p_z$ (right) distributions for low proton beam energy data.

Chapter 8

Stability Studies

One important check of the data quality for the cross section measurement is the stability of the measurement as a function of time. The basic quantity for this study is the relative event yield, defined as the number of selected DIS events per integrated luminosity, as a function of the luminosity run number. The kinematic region studied corresponds to low Q^2 and intermediate y. In the first part of this chapter the stability of the positron period in 2006 and the data in 2007 is analysed and in the second part the value of the yield for the three energy runs in 2007 is compared.

8.1 Stability of 2006 and 2007 Data

The selection applied is described in section 4.3, the energy measured by the SpaCal is required to be in a more restricted range, $15 < E'_e < 25$ GeV, which selects events in the intermediate y domain, where the background contribution is small enough to assume to have a background free sample and where the vertex reconstruction efficiency is largest. Additionally, a cut in θ_e is set, $160^\circ < \theta_e < 170^\circ$, to ensure 100% calorimeter acceptance independently from the z-position of the vertex. The mean and spread of the z-coordinate of the interaction vertex changes from run to run and the detector acceptance depends on the vertex position, so the result of not applying the cut in θ_e would be a varying yield. The inner region of the SpaCal is excluded with the s0 fiducial cut described in chapter 5 and the region corresponding to $R_{SpaCal} > 73$ cm is as well excluded.

The trigger selected was s2 except from the period between 10.01 and 13.03 2007, when there was a change in the priority of the subtriggers and s0 had a lower prescale. The energy threshold is higher for s2 than s0, see definition of the subtriggers in table 5.1, but the minimum value of the energy selected is 15 GeV, above both thresholds, so for this analysis they trigger the same SpaCal region. The trigger prescale is corrected for each event separately. In the case of the period in 2007 when s0 was selected, runs with s0 prescale higher than 3 were not analysed. The effect in the luminosity is negligible, only 0.2 pb^{-1} less than setting the maximum allowed prescale for example to 20. However, removing events with large prescale improves the statistical uncertainty. The average prescale of s0 for that period was 1.66 and for the low and medium energy runs the value is close to one. For these last two data sets

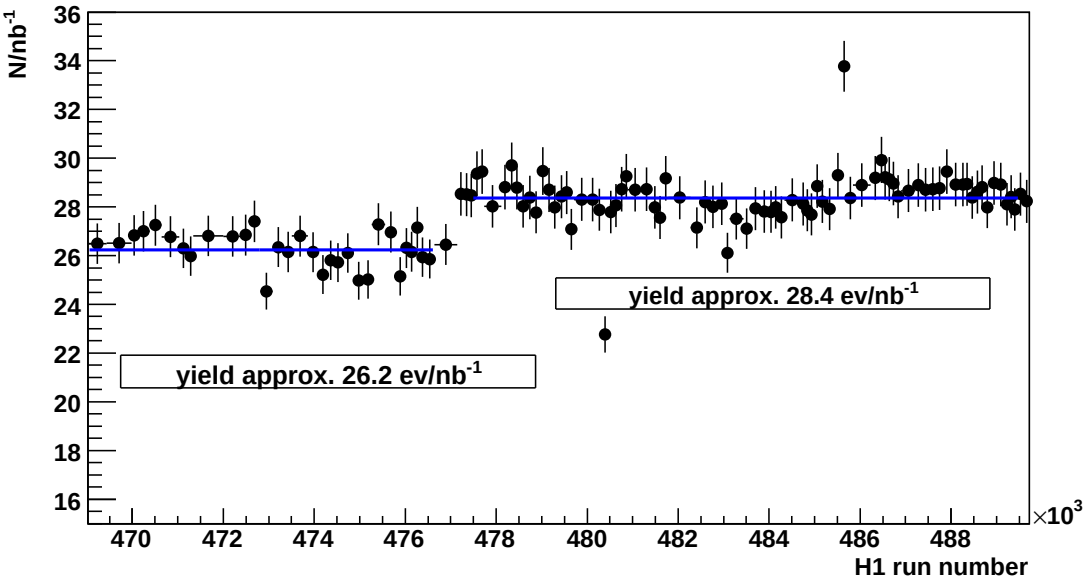

Figure 8.1: Yield in the positron running period in 2006.

one could also use s0 instead of s2 because its average prescale is equally low, the difference between them is on the per mil level.

In figures 8.1 to 8.4 the yield distribution as a function of the luminosity run number is presented for the different periods. At the beginning of September 2006 there is a step in the yield, its value is about 8% higher after approximately the run number 477200. It is suspected to be caused by a problem with the luminosity determination [40]. Apart from that, the yield is reasonable flat for all studied periods and for E_p= 920 GeV 2007 data has the same value as for 2006 after the step. The difference between the yield for the high energy run in 2007 and the low energy run is about 20% and between the high energy period and the medium energy is 16%. This difference is because the kinematic range is different for each period.

8.2 Comparison of the Yield for the Data Sets in 2007

The integrated luminosity is defined as

$$\mathcal{L} = N/\sigma \tag{8.1}$$

where σ is the cross section and N the number of DIS events selected. Then studying the yield is equivalent to study the cross section.The corresponding expression defined in section 2.14 is:

$$\frac{d^2\sigma}{dxdQ^2} = \kappa \left(F_2(x,Q^2) - \frac{y^2}{Y_+} F_L(x,Q^2) \right). \tag{8.2}$$

At low y the second term is negligible and the cross section is proportional to F_2. Fixing the values of x and Q^2, the dependence on y, or equivalently on the centre of mass energy $\sqrt{s}$,

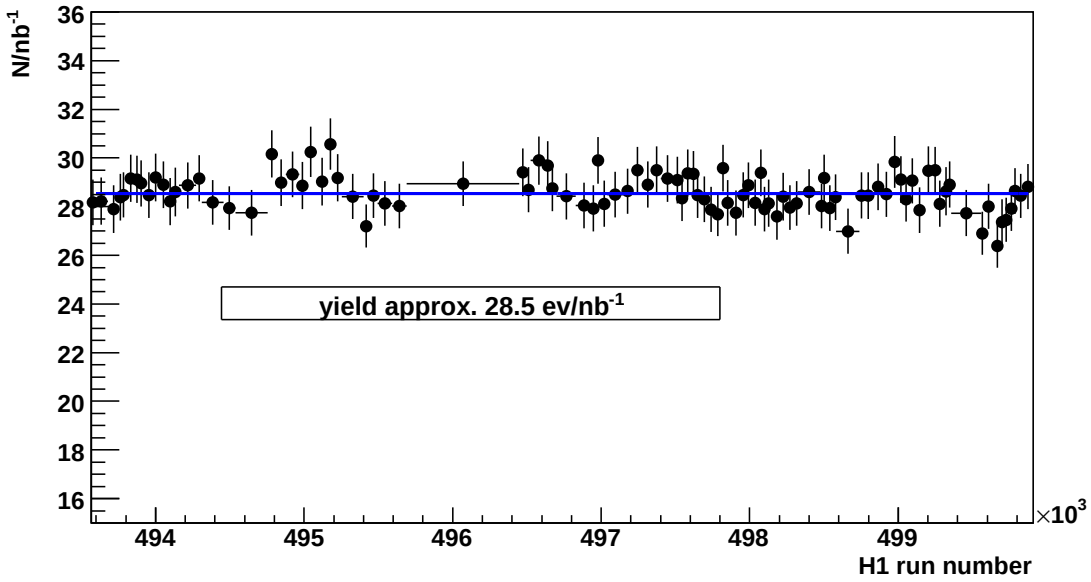

Figure 8.2: Yield in the period in 2007 when the subtrigger s0 had a higher priority (10.01-13.03.2007)

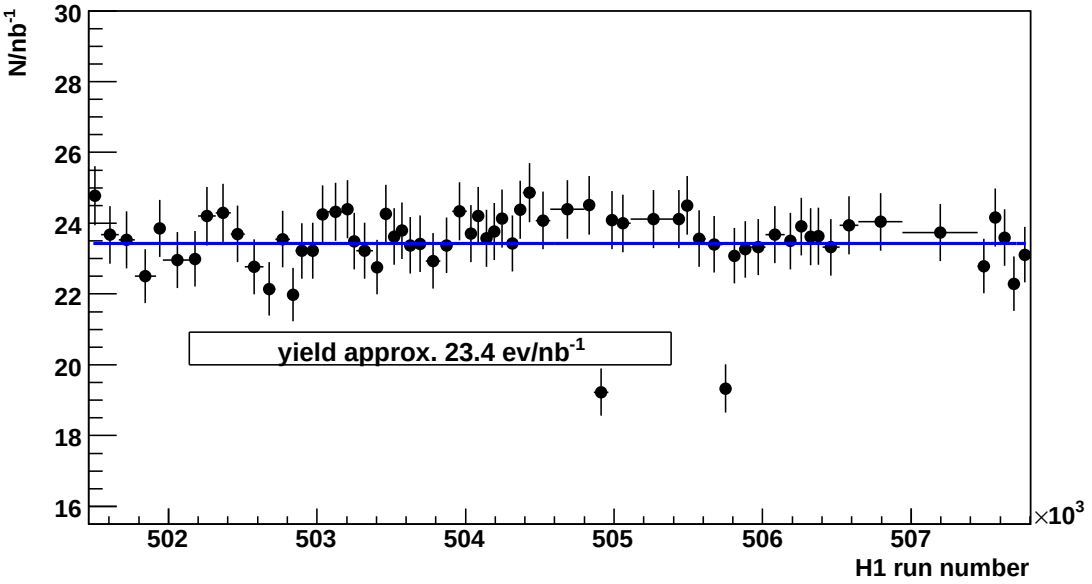

Figure 8.3: Yield in the low energy run period (E_p= 460 GeV)

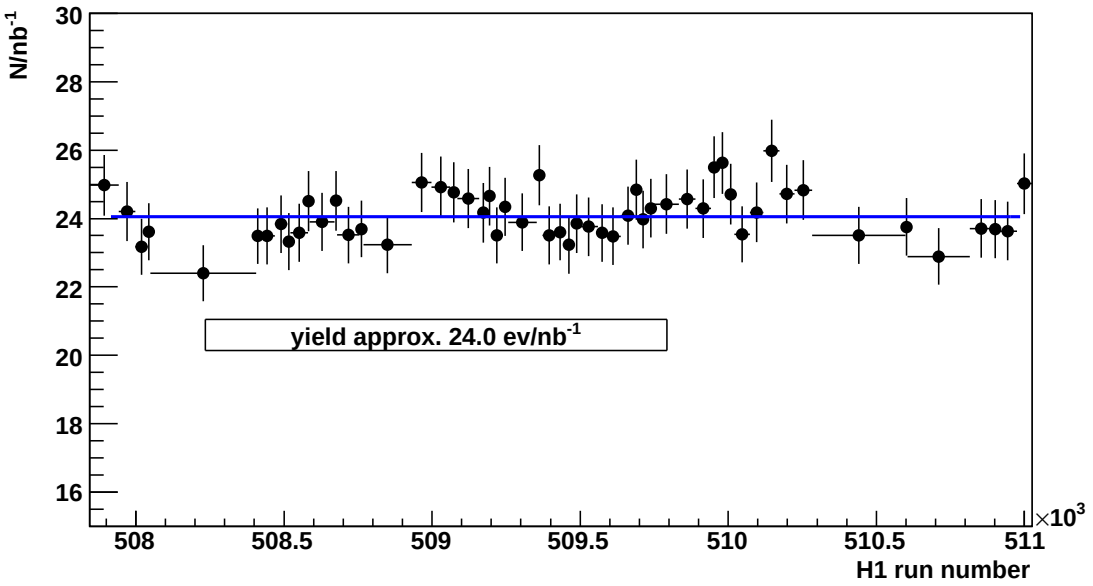

Figure 8.4: Yield in the intermediate energy run period (E_p= 575 GeV)

comes from the factor Y_+. This dependence can be removed by reweighting each event with the factor $1/Y_+$. Then the value of the cross section and the yield should be independent of s at fixed (x, Q^2). The aim of this section was to verify that assumption comparing the yield for the three data sets in 2007.

To compare the yield for high, intermediate and low proton beam energy data, it is necessary to match the range (x, Q^2) in such a way that the corresponding value of y, different for each energy, is small enough to assume that the term proportional to F_L in the cross section is negligible. To fulfill this criteria the selection of the previous section was modified, see below. The kinematic variables used are reconstructed by the "electron method" because of its better resolution for the chosen y domain.

- In this case, it is especially important that the kinematic variables are reconstruct as precisely as possible, then the corrected values of the scattered electron energy obtained with the calibration were used.
- Instead of applying a cut in the θ_e of the scattered electron, the cut was done in Q^2 reconstructed with the electron method. To have the same SpaCal acceptance for the three proton beam energy runs the cut was fixed to 20 GeV^2 $< Q_e^2 <$ 50 GeV^2.
- Different proton beam energy implies different centre of mass, $\sqrt{s}$. Given $s = 4E_pE_e$ and $Q^2/x = s \cdot y$, the chosen y range has to be modified to keep Q^2/x constant. The selected ranges for the three periods were:
  - E_p= 920 GeV data: $0.1 < y_e < 0.25$

- E_p= 460 GeV data: $0.16 < y_e < 0.4$
- E_p= 575 GeV data: $0.2 < y_e < 0.5$

- As mentioned above the events were reweighted, their weight was divided by the factor $Y_+ = 2(1-y) + y^2$ calculated with the electron method.

- In order to reduce the effect of radiative corrections, which are y-dependent and can be rather large for the electron method, a cut on y_Σ was applied. Taking into account that different y ranges are chosen, the cut in y_Σ was also different for the three energy runs. It was set to be one half of the lower cut in y_e.

  - E_p= 920 GeV data: $y_\Sigma > 0.05$
  - E_p= 460 GeV data: $y_\Sigma > 0.08$
  - E_p= 575 GeV data: $y_\Sigma > 0.1$

  In addition, the contribution of events which are misreconstructed by the electron method because of undetected ISR photons is reduced by the cut in $E - p_z$.

For the y-range chosen, the values of the factor multiplying F_L, $f(y)$, varies approximately between 0.005 and 0.02, so neglecting that term is a reasonable assumption. Therefore under these conditions the yield is expected to have the same value.

The first step before analysing the yield is to prove that the selection achieves its goal. In figure 8.5 the distributions for the kinematic variables x, Q^2 reconstructed by the electron method are shown. As expected the range of x coincides for the three data sets. Figure 8.6 shows the energy range of the scattered electron for the three energy runs and the kinematic variable y reconstructed by the Σ method. The arrows correspond to the value to which the cuts are set. One can see that selecting different values of y implies different energy ranges, it also affects the ranges of the SpaCal radius and θ_e. The difference between the proton beam energy is smaller for the medium and the low energy runs, then also the corresponding E'_e ranges are closer than for the high energy run. All the distributions are normalised to luminosity of the high E_p energy run.

Finally, the results for the yield are presented in figure 8.7. The value of the yield is obtained fitting the distribution with a straight line, the errors correspond to the precision of the fit. The yield for the E_p= 920 GeV data is around 6% higher than for E_p= 460 GeV data and about 10% higher compared to the E_p= 575 GeV data, which is a rather large disagreement. The reason is probably a problem with the luminosity determination, pointed out by the change in the yield after August 2006. It could also be due to radiative corrections which should be evaluated with the help of MC, but in next chapter it will be seen that they do not play a role.

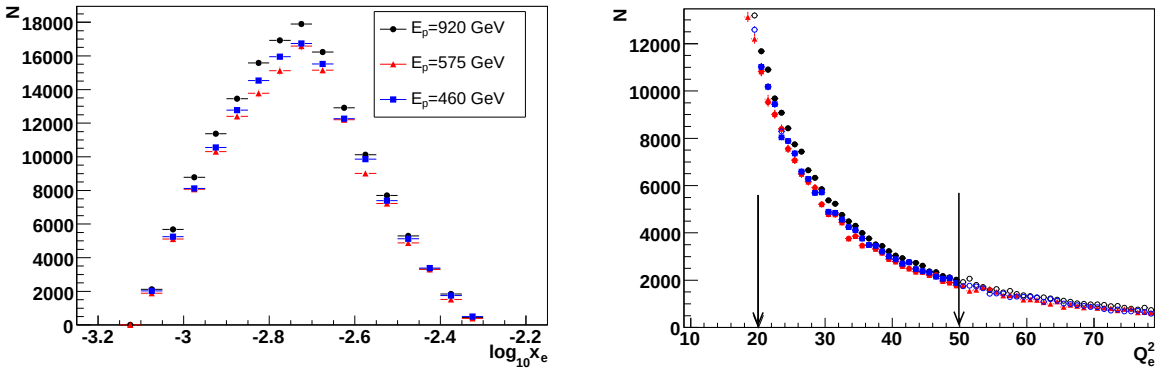

Figure 8.5: Kinematic variables x and Q^2 reconstructed by the electron method. The arrows in the Q^2 distribution indicate the limits of the cut. The circles correspond to $E_p = 920$ GeV data, the triangles to $E_p = 575$ GeV data and the squares to $E_p = 460$ GeV data.

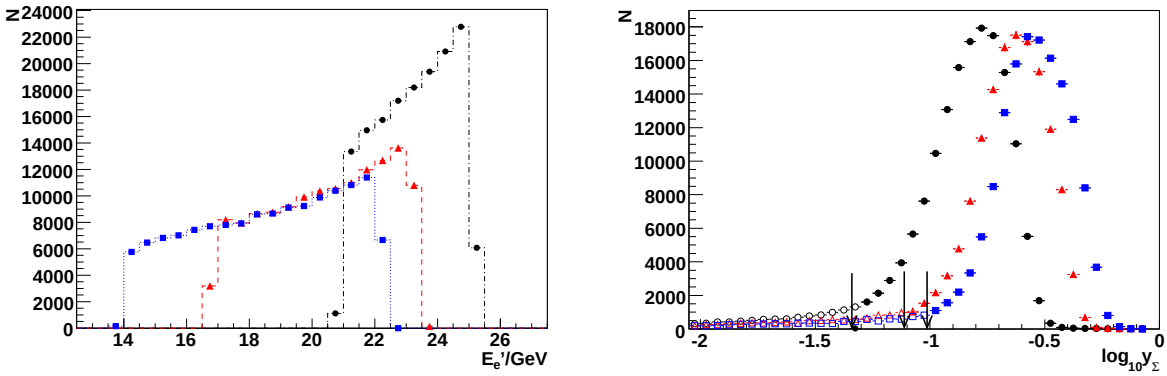

Figure 8.6: Energy of the scattered electron and the y variable reconstructed by the Σ method. The circles correspond to $E_p = 920$ GeV data, the triangles to $E_p = 575$ GeV data and the squares to $E_p = 460$ GeV data. The arrows show the cut in y_Σ for each energy run.

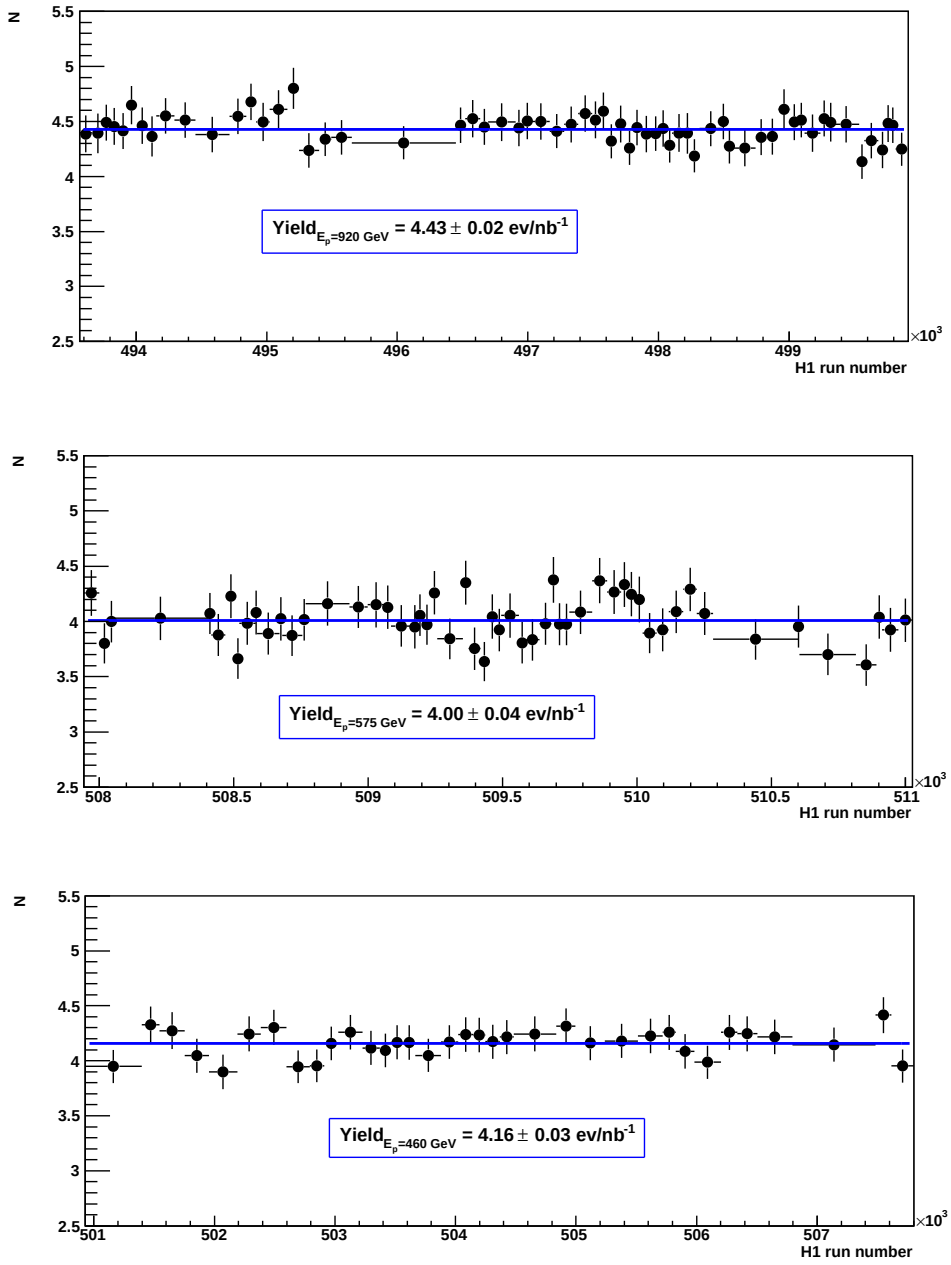

Figure 8.7: Yield corresponding to the three data sets in 2007, from top to bottom: High medium and low proton beam energy.

Chapter 9

DIS Cross Section Results

In this chapter the first cross-sections for the high and low proton beam energies in 2007 are presented. The reason why the study was not done as well for the intermediate value of the energy is the lack of an appropriate MC simulation. Together with the cross-sections, the control distributions and a preliminary evaluation of the systematic uncertainties are presented.

9.1 Monte Carlo Simulation

Monte Carlo programs are powerful tools to simplify the measurement of the DIS cross section. They allow to determine the corrections due to limited detector efficiency and acceptance, smearing of reconstructed kinematic variables due to detector resolution and radiative effects. They are also used to estimate the effects of systematic uncertainties on the cross section measurement.

The Monte Carlo generator program used was DJANGO [37], the version DJANGOH 1.4. For both low and high energy data sets, ten million events were simulated, corresponding to an integrated luminosity of $\mathcal{L} \sim 45$ pb^{-1} for the high energy simulation and $\mathcal{L} \sim 54$ pb^{-1} for the low energy one. The total luminosity for E_p= 920 GeV data is $\mathcal{L} \sim 34.0$ pb^{-1}, around 30% lower than for MC and for E_p= 460 GeV data $\mathcal{L} \sim 11.5$ pb^{-1}, five times lower. Leading order parton distributions from the PDFLIB with $F_L = 0$ with the code GRV5004 are used as an input structure functions. The phase space was restricted to $Q^2 > 5$ GeV^2. MC events at $Q^2 < 10$ GeV^2 are reweighted to reduce the number of simulated events at unused Q^2 values.

The production of Monte Carlo events are done in several steps. First, the events are generated according to a specific physics model using a MC generator, in this case DJANGO, as mentioned. This step involves the hadronisation of the final state quarks and gluons. The result is a set of 4-momenta and the identities of the final state particles. The second step is the detailed simulation of the H1 detector response to the generated events. The result is similar to real data and it is treated in the same way as data in the reconstruction and analysis steps.

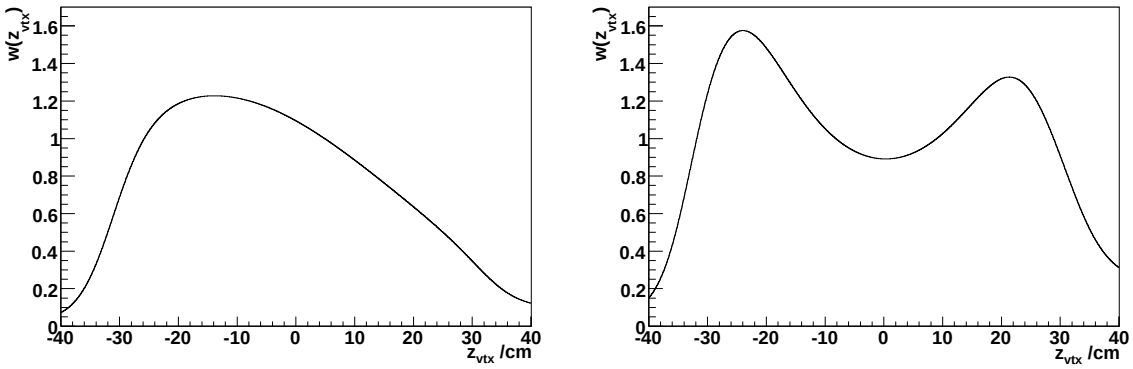

Figure 9.1: Reweighting functions for the E_p= 460 GeV MC vertex distribution, left, and for the E_p= 920 GeV MC, right.

To compare MC and data it is necessary to tune the MC simulation to reproduce the data behaviour. Apart from the calibration described previously, the MC is reweighted with two different correction factors, one related to the vertex distribution of the simulated events and the other corresponds to the structure function assumption used for the MC.

9.1.1 Event Weight

z-vertex Position

It has already been mentioned that for an accurate reconstruction of the event kinematics a precise knowledge of the position of the vertex, in particular the z-position, is needed. Therefore it is important that it is well described by MC. To reconstruct the vertex in data the so called *beam tilt* correction is applied, which takes into account the measured beam offset and tilt between the H1 z-axis and the beams due to changing beam conditions. This correction is also approximately introduced in the MC simulation.

The generated vertex position of the MC is a Gaussian distribution with a fixed mean position and width and it is necessary to reweight it to the data distribution. To obtain a mostly unbiased z-vertex distribution, the DIS event selection with the electron scattered in the SpaCal is used. The selection applied was exactly the same than in section 8.1 based on the description in [23]: Apart from the general cuts, $15 < E'_e < 25$ GeV and $160° < \theta_e < 170°$ are required to have a background free selection, the highest z-vertex reconstruction efficiency and 100% SpaCal acceptance.

The z-vertex distribution for data and MC are fitted to a Gaussian plus a polynomial function to describe the tails of the distribution. The weight used for the MC is calculated as

$$weight_{z-vertex} = \frac{F(z_v^{data})}{F(z_v^{MC})} \tag{9.1}$$

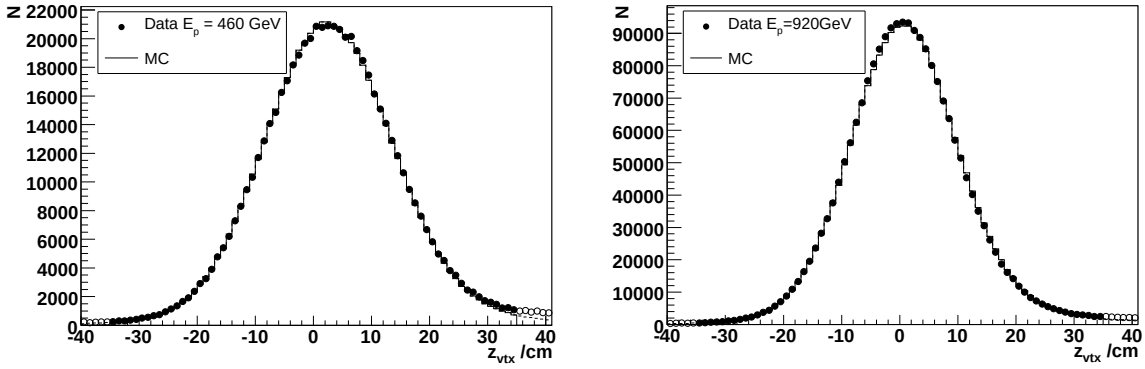

Figure 9.2: z-vertex distributions for the low proton beam energy data, left, and the high proton beam energy data, right. The closed circles represent the experimental data and the open histogram, the MC simulation. The distributions are normalised to area.

where $F(z_v^{data}) = G(z_v^{data}) + P(z_v^{data})$ and $F(z_v^{MC}) = G(z_v^{MC}) + P(z_v^{MC})$ are the fitted functions. In figure 9.1 the weight function applied to the z-vertex distribution for MC is presented for E_p=920 GeV and E_p=460 GeV. In figure 9.2 the distribution for data and reweighted MC are shown. They are normalised to the area of the data sample. There are no remarkable differences between the distributions.

Cross Section Reweighting

The next correction was applied to adjust the DIS cross-section used for the MC generation to an experimental measurement. Each MC event is weighted by the ratio of the double differential cross-sections calculated from the generated kinematics:

$$weight_{kin} = \frac{\sigma_{new}(x, y, Q^2)}{\sigma_{old}(x, y, Q^2)}. \tag{9.2}$$

$\sigma_{old}(x, y, Q^2)$ is evaluated with the GRV-LO 94 of F_2 and $F_L = 0$ parametrisation and $\sigma_{new}(x, y, Q^2)$ was obtained using the H1PDF2000 functions [36].

9.2 Summary of the Systematic Error Sources

The measured cross section is influenced by systematics effects, there are two types known as uncorrelated and correlated errors. The latter affect in the same direction different bins and they are related for example to the reconstruction of the kinematic variables. The sources considered in this thesis to determine the systematics were:

- The uncertainty in the electron energy scale is estimated a function of the energy, according to the equation

$$\frac{\delta E'_e}{E'_e} = 0.003 + 0.015 \cdot \frac{(27.6 - E'_e/GeV)}{26.6} \tag{9.3}$$

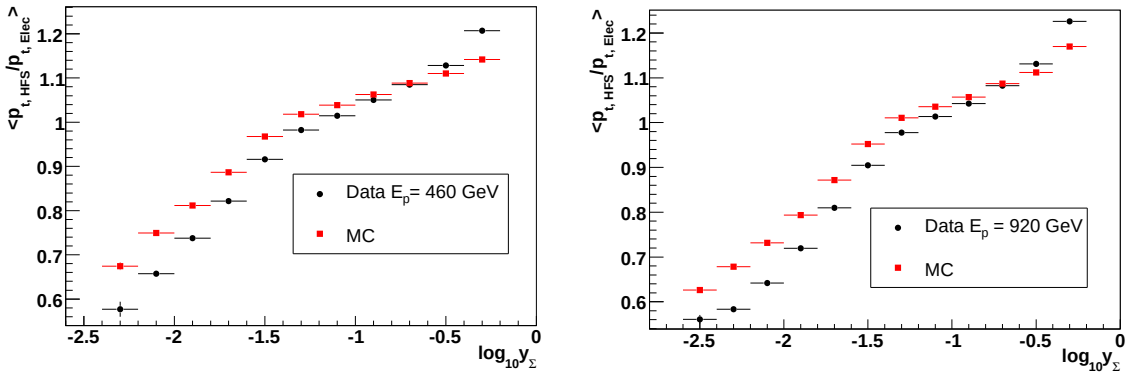

Figure 9.3: Test of the hadronic final state energy scale using the mean of the p_t balance ratio distributions as a function of y_Σ for the E_p=460 GeV sample, left plot, and E_p=920 GeV sample, right plot.

For the kinematic peak, it corresponds to 0.3% and for values of the energy about 1GeV it is approximately 2%. Former analysis have shown that with the same calibration procedure the uncertainty at the kinematic peak is better than 0.2% [26], in this thesis the chosen uncertainty is more conservative, 50% higher, as it has not been checked in such a detail.

- The electron polar angle is measured with the SpaCal which is optimised to measure energy but not position, since it is not a tracker. Then the error is set to 1 mrad, in line with other measurements using a similar method [35], because no further studies, apart from comparing θ_e with the CIP for the alignment, were done.

- For SpaCal contribution to the hadronic final state energy scale the uncertainty is chosen 0.9 GeV, it was derived with the same method than in [26]. The influence of this source was checked and found out to be small.

- The distributions in 9.3 show the dependence of the mean value of the p_t *balance* ratio between the hadronic final state and the electron as a function of y_Σ. The expected value should be always close to 1. However, there is a clear discrepancy for data and MC. The disagreement between the data distribution and MC increases at lower values of y_Σ, the ratio is significantly lower for data than for MC, at $\log_{10} y_\Sigma \lesssim -2.0$ the difference is about 10%. Therefore the uncertainty of the hadronic final state energy scale was selected 4% at $\log_{10} y_\Sigma > -1.5$ and a 10% per decade for smaller values of y_h according to this expression:

$$\frac{\delta y_\Sigma}{y_\Sigma} = 0.04 + 0.10 \cdot (-\log_{10} y_\Sigma - 1.5) \qquad \text{for} \quad y_\Sigma < -1.5 \tag{9.4}$$

- The error corresponding to the LAr noise fraction is 20%. In figures 9.7 and 9.9 one can see that the chosen error covers the discrepancies in the noise. The values of this uncertainty source and the previous one are quite conservative, but considering that there is no correction or calibration applied for the hadronic final state they seem adequate.

To estimate the correlated systematic errors the procedure is the following: For each of the sources listed above the relevant quantities are varied by the uncertainty in the MC simulation, separately in positive and negative directions. The reduced cross-sections for the former, σ_r^+ and the latter case σ_r^- are determined and the relative systematic error is calculated as

$$\delta = \frac{\sigma_r^+ - \sigma_r^-}{2\sigma_r^0} \tag{9.5}$$

where σ_r^0 is the reduced cross section without systematic variations.

The uncertainty taken for the uncorrelated sources, radiative corrections, efficiency of the subtriggers and the vertex determination, is 0.5% for each source. The radiative corrections have not been studied so the uncertainty is taken as in [6]. As it was seen in section 5.1 the efficiency of the subtriggers used is greater than 99.8%, considering some inefficiency coming from the global options or some local variations a 0.5% uncertainty is a safe value. The vertex reconstruction has been done combining the central and CIP vertices. It is considered to be highly efficient, since, as it was seen in section 6.1, the efficiency of the CIP alone is nearly 99% for high enough R_{CIP}. Bins at high y are selectively rejected so the amount of residual $\gamma - p$ background is expected to be lower than 2% [25].

9.3 Control Distributions

Before measuring the cross-section, it is necessary to check that the MC simulation after the reweighting reproduces correctly the behaviour of the data. This is done comparing the data and MC distributions of the most important variables.

The selection is exactly the one described in section 4.3 plus the fiducial cuts in R_{SpaCal}. Additionally, the value of Q_e^2 was required to be greater than 10 GeV^2. This is motivated for two reasons, first of all due to the fiducial cut in the radius no lower values could be reached and second, because for lower values of Q_e^2, the MC simulation is not be adequate.

The triggers selected are s0 for the low proton beam energy run and s0 and s3 for the high proton beam energy run. s3 does not cover the whole SpaCal range selected because of its higher cut in radius. However, it was included for the high energy run because its efficiency is similar to the efficiency of s0 and its average prescale was approximately 1, lower than s0 prescale. Then the events triggered by s3 have a lower weight than events triggered by s0 so the statistical uncertainty improves.

The MC simulation was reweighted for the control distributions to the H1PDF2000 functions plus a 12% correction for the high energy sample and 8% for the low energy one. The Monte Carlo cross section reweighting has very little influence on the extraction of the measured DIS cross section, the assumptions about it cancel in the acceptance calculation. In figures 9.4 and 9.5 the distributions of variables reconstructed with the electron method are

shown. The MC samples are normalised to the integrated luminosity of the data. The data and MC correspond to the selected bins in the (x, Q^2) plane used to obtain the cross section, which are introduced in the next section. One can see that there is a good agreement between data and MC for the low energy sample as well as for the high energy data.

In figures 9.6 and 9.8 kinematic variables reconstructed with the Σ method are presented. The MC describes correctly the data despite lacking hadronic calibration and the worse resolution of the kinematic variables reconstructed by the Σ method. The p_t balance plot shows a small disagreement, this is a consequence of the missing calibration for the energy of the hadronic final state particles. Figures 9.7 and 9.9 show the distribution of the fraction of y_h contributed by tracks, LAr calorimeter and noise and SpaCal for the high and low energy runs, respectively, to study the hadronic energy flow as in [25]. Instead of comparing data with the mean value of MC the allowed range of the MC considering the systematics is plotted. The assigned systematic uncertainties seem in general adequate, the agreement is reasonable. As expected, at low y the main contribution to y_h comes from the LAr calorimeter, according to the DIS kinematics the hadronic final state has a forward direction. At high y the greater contribution comes from the SpaCal. The contribution of tracks is about 30% in the medium y domain. The influence of the noise is large at $y < 0.01$, its effects varies from 40% to 80%.

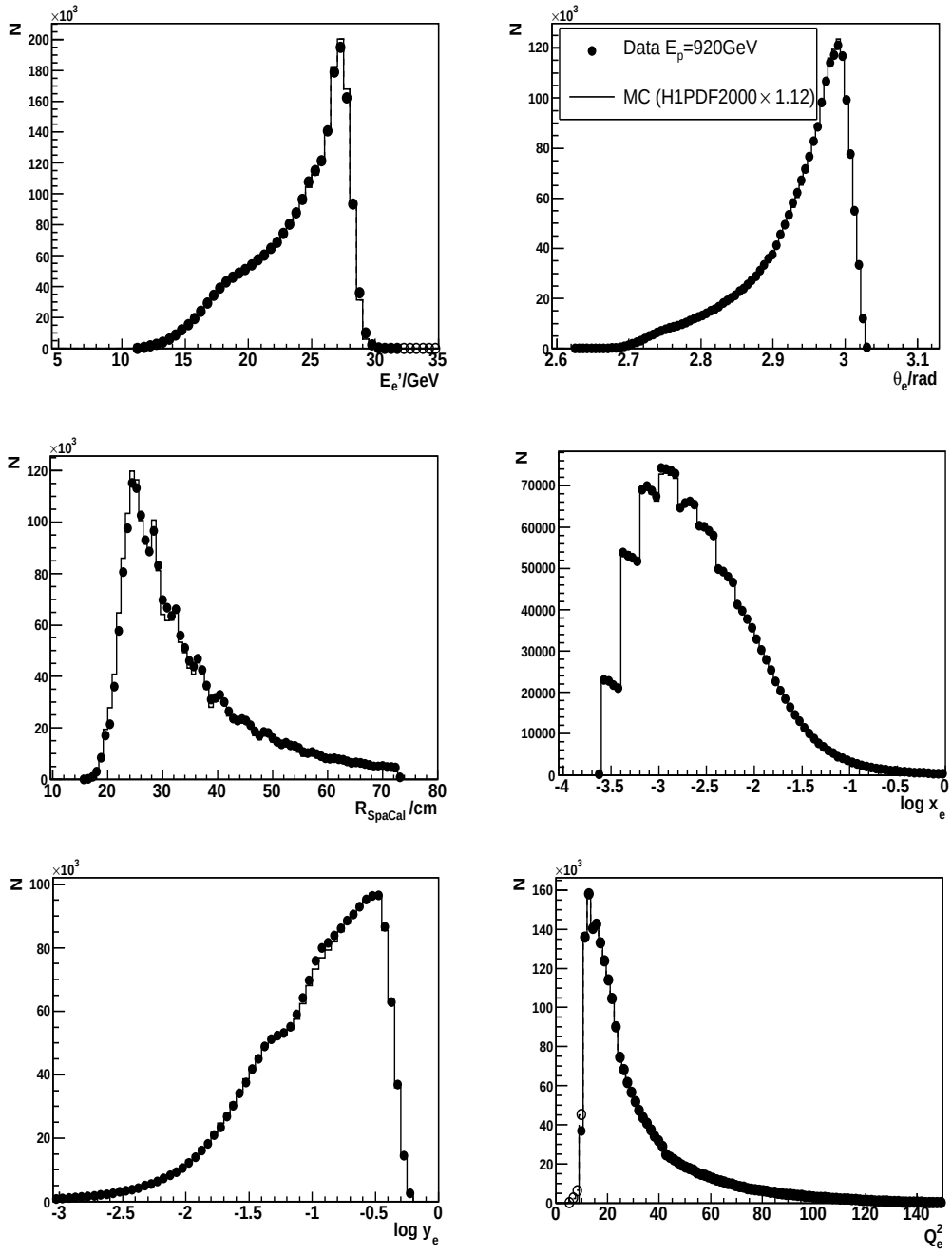

Figure 9.4: Control distributions of the high proton beam energy data sample in 2007. The open histogram corresponds to MC and the closed circles to data. The distributions presented from left to right and from top to bottom are: Energy of the scattered electron, polar angle, radius in the SpaCal and the kinematic variables x, y and Q^2 reconstructed with the electron method.

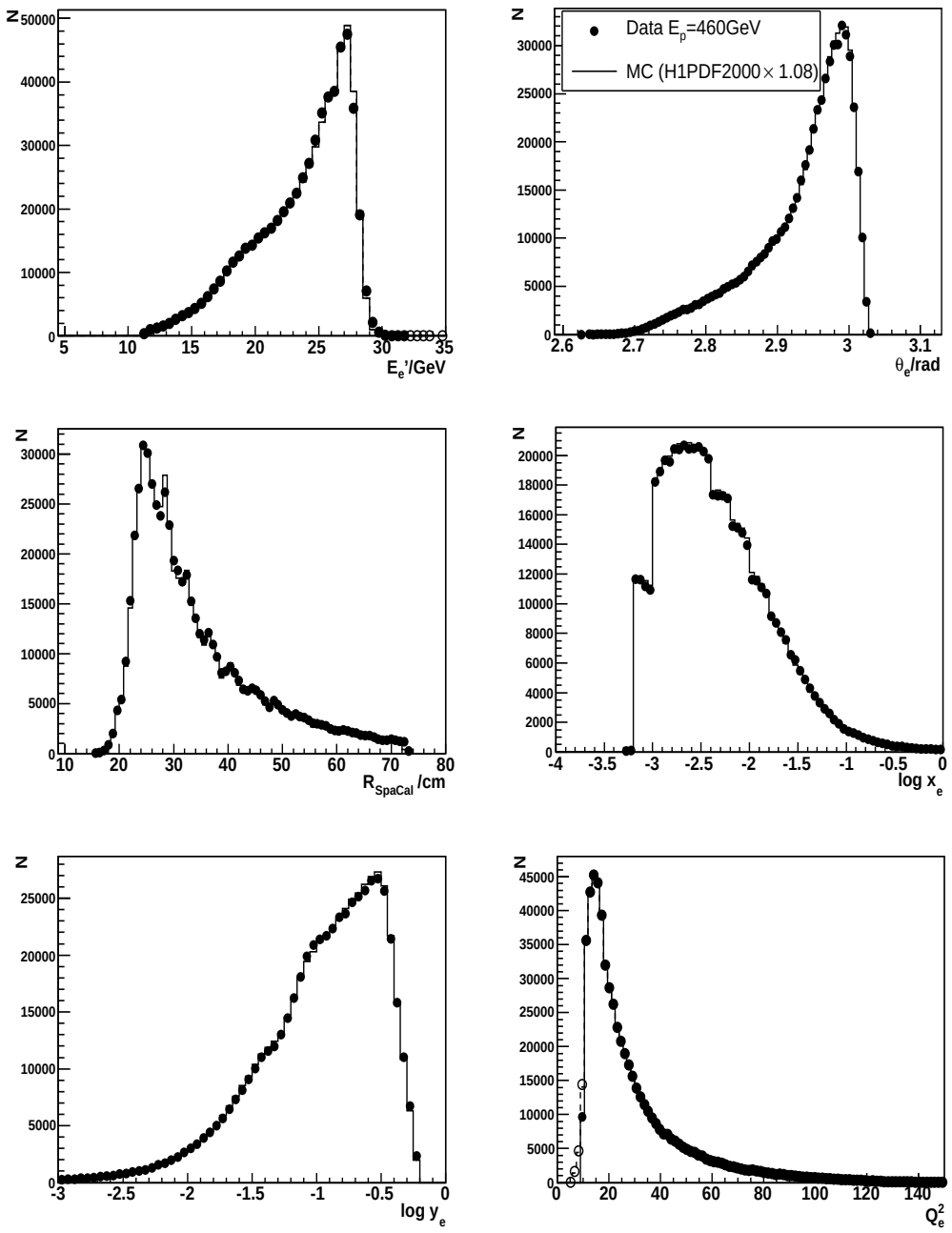

Figure 9.5: Control distributions of the low proton beam energy data sample in 2007. The open histogram corresponds to MC and the closed circles to data. The distributions presented from left to right and from top to bottom are, like on the previous figure: Energy of the scattered electron and polar angle, radius in the SpaCal and the kinematic variables x_e and y_e and finally Q^2_e.

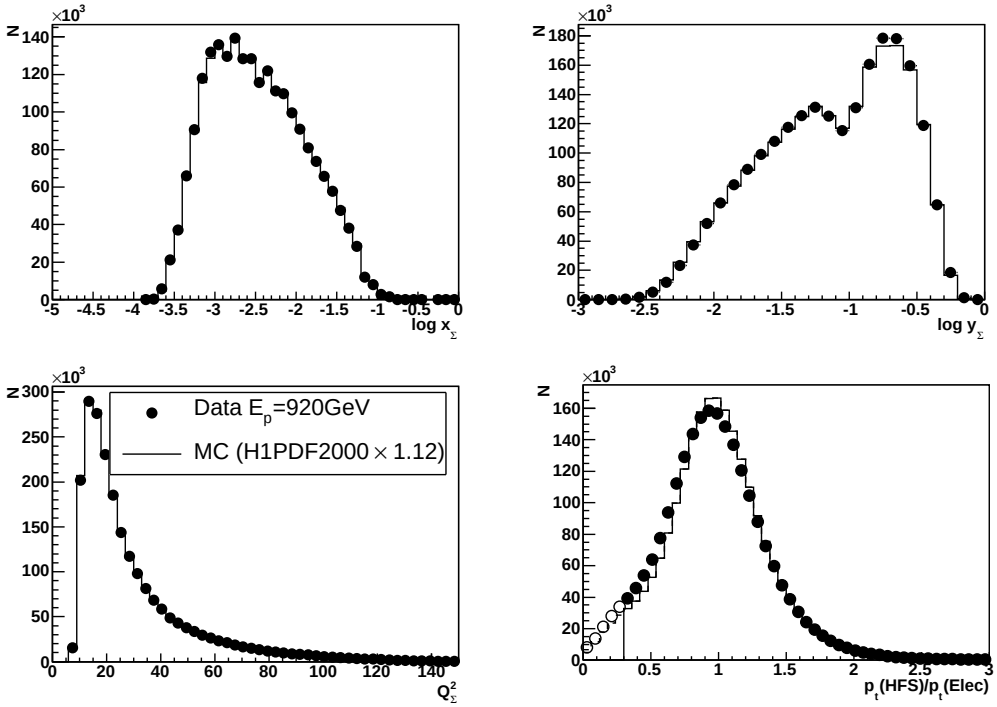

Figure 9.6: Control distributions for the E_p= 920 GeV data in 2007 (closed circles) and MC (open histogram). The kinematic variables x, y and Q^2 reconstructed with the Σ method and the ratio between the hadronic final state particles transverse momentum and the scattered electron transverse momentum are shown from left to right and from top to bottom.

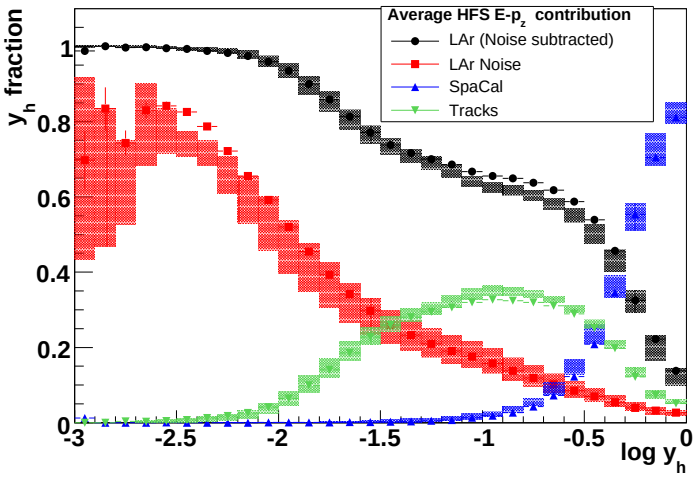

Figure 9.7: Distribution of the fraction of y_h contributed by tracks, LAr calorimeter and noise and SpaCal for the E_p= 920 GeV sample. The shaded areas correspond to the range of the MC simulation considering the systematic uncertainties.

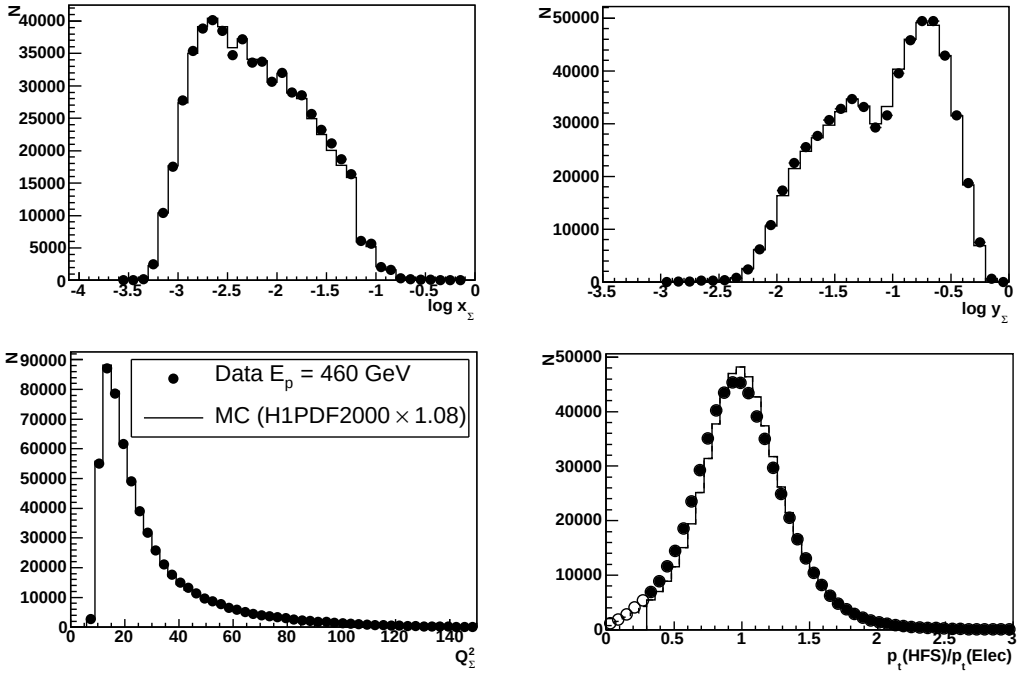

Figure 9.8: Control distributions for the E_p= 460 GeV data in 2007. The open histogram corresponds to MC and the closed circles to data. The distributions presented from left to right and from top to bottom are: Kinematic variables x, y and Q^2 reconstructed with the Σ method and the ratio between the hadronic final state particles transverse momentum and the scattered electron transverse momentum.

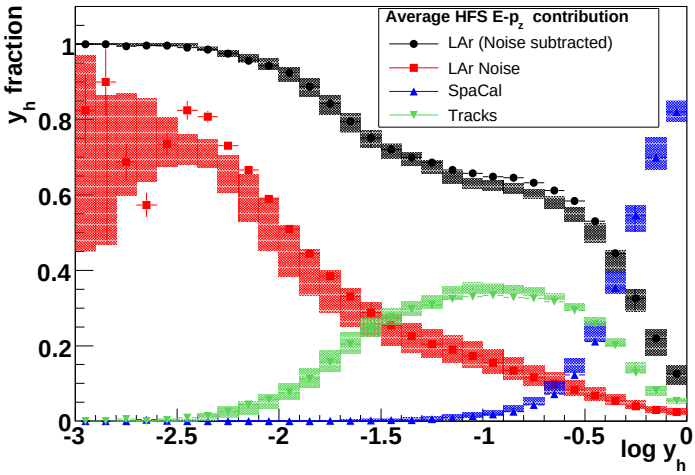

Figure 9.9: Distribution of the fraction of y_h contributed by tracks, LAr calorimeter and noise and SpaCal for the E_p= 460 GeV sample. The shaded areas correspond to the range of the MC simulation considering the systematic uncertainties.

9.4 Cross Section Measurement

The measurement of the cross-section is performed in bins. The binning chosen in the (x, Q^2) plane is appropriate because the structure functions of the proton are usually also expressed in terms of those variables. The aim of the binning is to have equally distributed statistics and to minimise the migration of events between the bins, which is studied using their "purity" and "stability". The objective is also to have a nearly photoproduction background free sample. The "purity" indicates how much the events measured in a bin are contaminated by event migration from adjacent bins, whereas the stability controls the migration of events out of the bin. They are defined as:

$$Purity = \frac{N_{rec\&\&gen}}{N_{rec}} \quad Stability = \frac{N_{rec\&\&gen}}{N_{gen}} \tag{9.6}$$

where N_{rec}, N_{gen} are the numbers of events reconstructed and generated in a certain bin and $N_{rec\&\&gen}$ is the number of events reconstructed and generated in the same bin. Both quantities take values between 0 and 1 by definition and they are sensitive to resolution and shifts in the reconstruction of x and Q^2.

The selected bins using the electron or the Σ method with the corresponding purity and stability values are shown in figure 9.10, E_p= 920 GeV data, and in figure 9.11, E_p= 460 GeV data. From these plots one can see that the values of the purity vary between approximately 30% and 60% for both methods and energies. The stability for the high energy sample has values between 35% and 60% for the Σ method and between 35%-90% for the electron method, see figure 9.10. For the low energy data the values vary between 45%-70% and 40%-70% for the electron and Σ method respectively.

The high values of the purity and stability reconstructed by the electron method are a consequence of the high resolution of the kinematic variables based on the precisely measured electron energy and polar angle. However, the y_e resolution degrades rapidly towards low y due to the factor $1/y$, see section 2.2. That causes a drop of purity and stability to too low values below $y \approx 0.1$, which limits the applicability of this method. The Σ method is then preferable, the resolution in y_Σ is less dependent on y, therefore the values of the purity and stability show a much smaller variation within the inelasticity range. The differential cross-section is measured in a bin only if the purity and stability is higher than 30%. In the kinematic region where the electron and the Σ method overlap, the electron method is preferred due to its smaller uncertainty, because of the performed calibration, as long as it satisfies the criteria in purity and stability. The Σ method allows to extend the measurement to higher x where the electron method has large uncertainty.

In principle the cross section measurement is performed using the integrated luminosity $\mathcal{L}_{Data}$ and the number of events collected in a bin N_{Data}, $\sigma = N_{Data}/\mathcal{L}_{Data}$. However several factors have to be taken into account, leading to the following expression:

$$\frac{\mathrm{d}^2\sigma(x, Q^2)}{\mathrm{d}x\mathrm{d}Q^2} = \frac{N_{Data} - N_{\gamma p} - N_{BG}}{A \cdot \mathcal{L}_{Data}} \cdot \frac{1}{1 + \delta_{RC}} \cdot c_{BC} \,. \tag{9.7}$$

where:

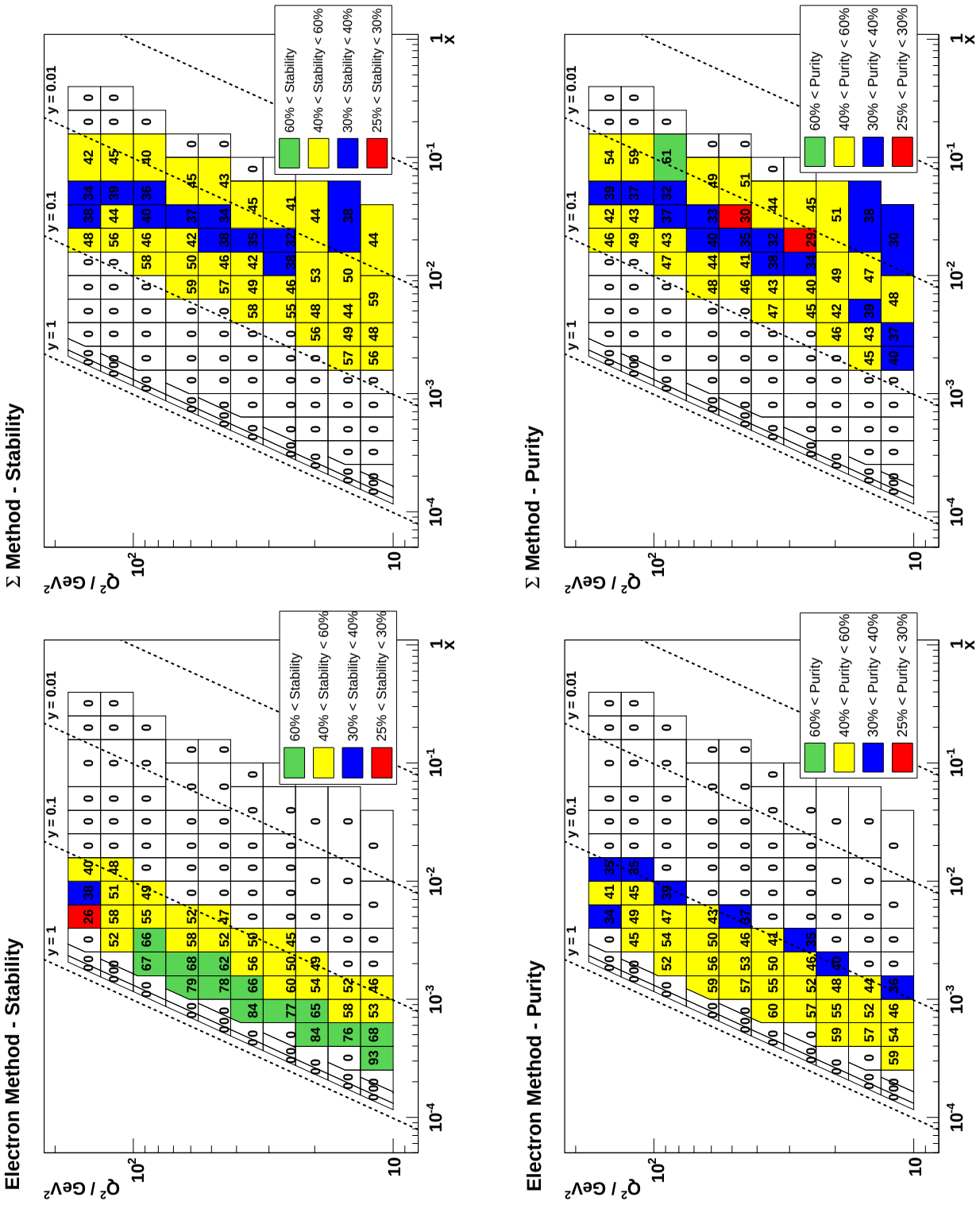

Figure 9.10: Purity and stability values for the selected bins for the high energy proton beam sample, reconstructed with the Σ or electron method.

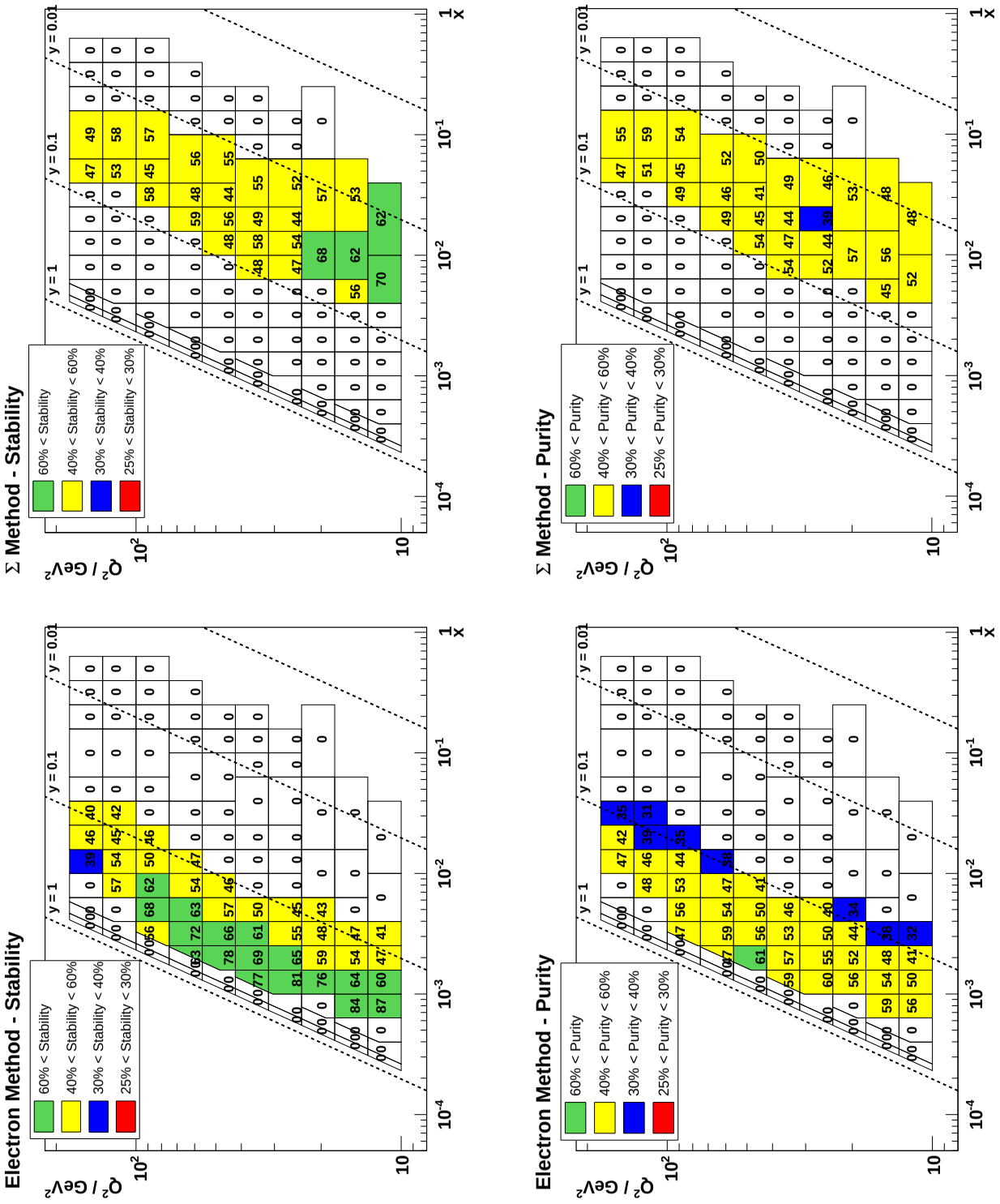

Figure 9.11: Purity and stability values for the selected bins for the low energy proton beam sample, reconstructed with the Σ or electron method.

- $N_{\gamma p}$ is the number of photoproduction events in the bin which is, taking into account the selection, negligible with respect to the total number of events, N_{data}.
- N_{BG} corresponds to the number of events due to other (non-ep) background, it has not been analysed but it is expected to be also a small value due to the selection.
- A is the detector acceptance, which is calculated using the MC simulation as $A = N_{rec}^{MC}/N_{gen}^{MC}$.
- δ_{RC} represents the radiative corrections on the Born level cross section, calculated as $\delta = \sigma_{rad}^{MC}/\sigma_{Born}^{MC} - 1$, where σ_{rad}^{MC} and σ_{Born}^{MC} are bin integrated full and Born level cross sections respectively taken from MC simulation.
- c_{BC} is the *bin centre correction*, which has to be applied in order to take the maximum variation of the cross section over the bin size and to obtain the cross section at the bin centre value. It can be derived from MC as

$$c_{BC} = \frac{\mathrm{d}^2\sigma^{MC}(x_c, Q_c^2)}{\mathrm{d}x\mathrm{d}Q^2}/\sigma_{Born}^{MC} \tag{9.8}$$

The cross section measurement is simplified because the DJANGO MC already contains the radiative corrections. Using the relation

$$N_{gen}^{MC} = \mathcal{L}^{MC}\sigma_{rad}^{MC}\,, \tag{9.9}$$

the formula to determine the cross section via the *Monte Carlo Method* is obtained.

$$\frac{\mathrm{d}^2\sigma(x, Q^2)}{\mathrm{d}x\mathrm{d}Q^2} = \frac{N_{Data} - N_{\gamma p} - N_{BG}}{N_{rec}^{MC}} \cdot \frac{\mathcal{L}^{MC}}{\mathcal{L}_{Data}} \frac{\mathrm{d}^2\sigma^{MC}(x, Q^2)}{\mathrm{d}x\mathrm{d}Q^2}\,, \tag{9.10}$$

since

$$\frac{1}{A}\frac{1}{1+\delta_{RC}} \cdot c_{BC} = \left[\frac{N_{gen}^{MC}}{N_{rec}^{MC}}\right] \cdot \left[\frac{\sigma_{Born}^{MC}}{\sigma_{rad}^{MC}}\right] \cdot \left[\frac{\mathrm{d}^2\sigma^{MC}(x, Q^2)}{\mathrm{d}x\mathrm{d}Q^2}\frac{1}{\sigma_{Born}^{MC}}\right] = \frac{\mathcal{L}^{MC}}{N_{rec}^{MC}} \cdot \frac{\mathrm{d}^2\sigma^{MC}(x, Q^2)}{\mathrm{d}x\mathrm{d}Q^2}. \tag{9.11}$$

The results of the cross section measurements presented in this thesis are listed in the tables in Appendix A. Instead of calculating σ, the reduced cross section, σ_r will be obtained as in equation 2.22. In figure 9.12 the cross section for the low energy and high energy sample is shown. The error bars, which are in most of the cases smaller than the marker size, are calculated as $\sqrt{\delta_{syst}^2 + \delta_{stat}^2}$. The error on the cross-section determination is clearly dominated by the systematic uncertainties. Only for very few bins at low Q^2 the statistical error exceeds the systematic one.

The difference between the cross section of the high and low proton beam energy is about 5-6%. This is in good agreement with the difference between the yields presented in the previous chapter. The radiative corrections are included in the calculation of the cross section so they are not the reason of the difference in the yield or the cross section between the two

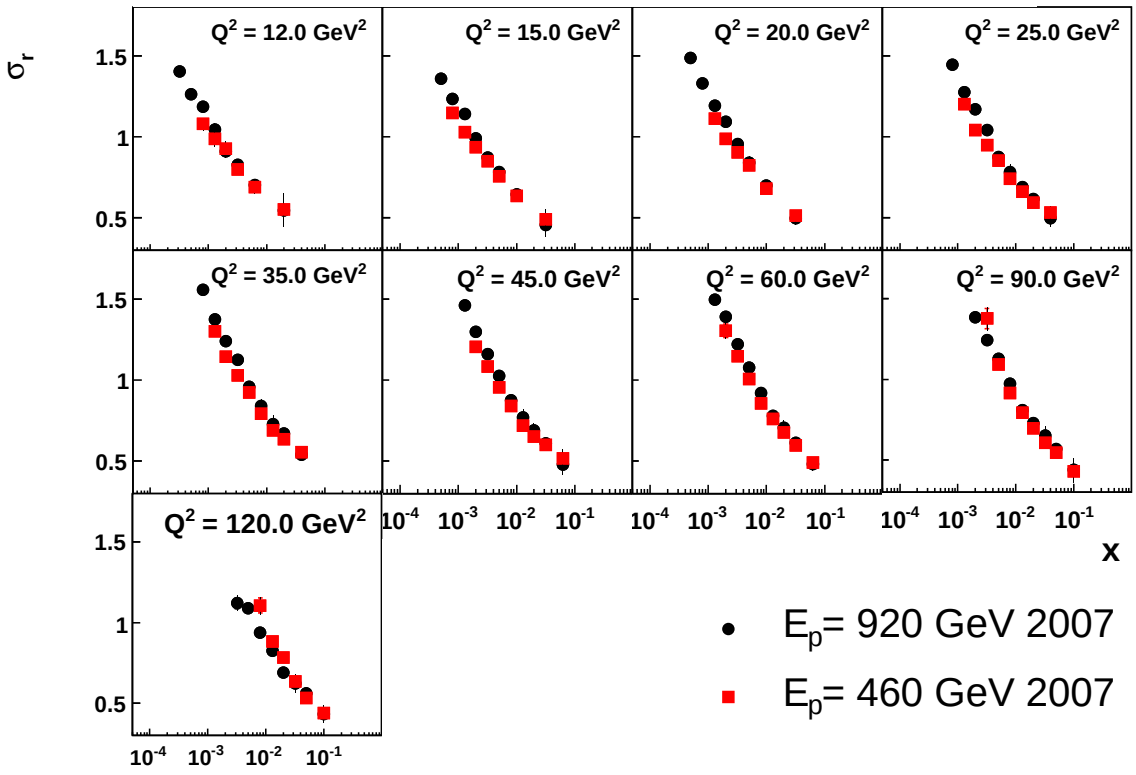

Figure 9.12: Reduced cross section measurement as a function of x for different Q^2 values. The points are reconstructed with the electron or Σ method according to the bin selection. The errors are quadratical sum of systematics and statistical errors.

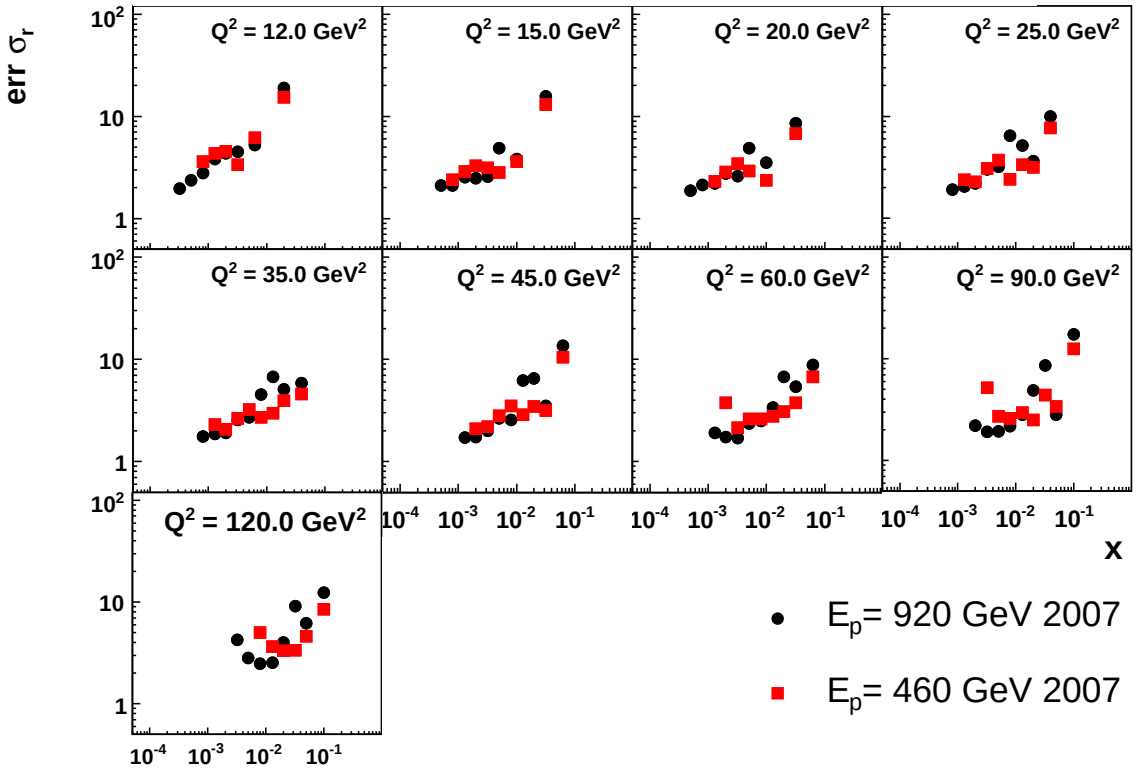

Figure 9.13: Total systematic uncertainties for the E_p= 920 GeV data, closed circles, and E_p= 460 GeV data, squares.

data sets and the disagreement comes from the luminosity determination.

In figure 9.13 the total systematic error are shown, they vary between 3% to 10%. For points corresponding to the electron method the uncertainty lies within 3%. However, the errors corresponding to points obtained with the Σ method are rather large because there is no hadronic final state energy calibration. The uncertainty is especially high for the $E_p = 920$ GeV data because, at fixed (x, Q^2), y is half of the value for the $E_p = 460$ GeV sample and, therefore, the uncertainty due to the hadronic final state measurement is larger, see section 9.2.

The last published H1 measurement in the same kinematic range used H1 data from years 96/97 [6]. Figure 9.14 shows a comparison between the cross section measured for the 2007 data and the mentioned high precision measurement. The ratio shows a rather large disagreement, up to 15% for the E_p= 920 GeV data in 2007 and 10% for the E_p= 460 GeV sample. However, this difference is consistent with a global normalisation effect, out of the scope of this analysis. This should be seen in the light the step found in the yield in September 2006.

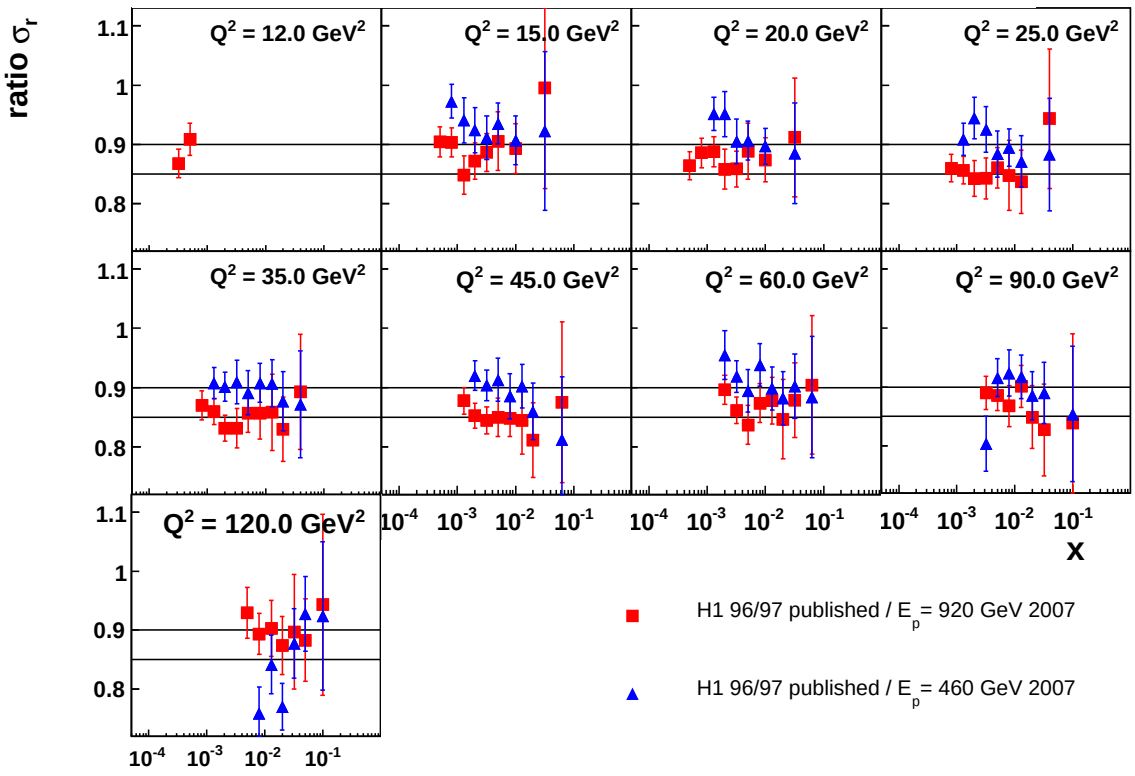

Figure 9.14: Ratio between the measured cross section of H1 96/97 [6] and the high proton beam energy data, squares, and the low proton beam energy data, triangles.

Chapter 10

Conclusions

Prior to the measurement of the longitudinal proton structure function it is necessary to analyse the performance of the detectors involved and the quality of the data. That was the purpose of this thesis, the kinematic range studied was $10 < Q^2 < 120$ GeV^2 and the low and intermediate y, $y < 0.6$, where the background is low. This kinematic range corresponds to a high scattered electron energy measured in the SpaCal.

The performance of the SpaCal, BST and CIP was studied. The SpaCal trigger efficiency was obtained for subtriggers s0 and s3, their efficiency was determined to be 99.9%. The efficiency of the non SpaCal components of s7 and s8 was also checked. Their efficiency, especially for s7, is lower than for the SpaCal subtriggers. However, this should not be a problem for the F_L measurement because of the combination of s7 with s8. The tracking efficiency of the BST is about 80%-85%, depending on if the tracks are fitted to a vertex or not, while for MC the efficiency is the same in both cases. The alignment needs to be corrected to improve the efficiency within the sector borders and to remove the ϕ dependence of the momentum measurement, which will be fundamental to remove the γ-p background at lower E'_e. The CIP vertex reconstruction was probed to be correct and after the alignment the uncertainty of the θ measurement is around 1 mrad.

The second part of this work was to study the data quality of the three proton beam energy runs in 2007 with E_p=920 GeV, E_p=460 GeV and E_p=575 GeV. The stability of these three sets was analysed: The yield is always flat without significant variations. The yield was also obtained for the positron run in 2006 because of the suspicion that there was a problem with the luminosity determination. For the measurement of F_L an absolute shift in the luminosity would not be critical, but an unknown relative shift between the three different sets would make the measurement impossible. It has been found that the normalisation of the three data sets differs up to 10%, which is unexpectedly large and needs to be corrected to perform the F_L and inclusive DIS cross section measurements.

The behaviour of the E_p=920 GeV and E_p=460 GeV data was compared to MC, the scattered electron energy was calibrated and the MC was also reweighted to the data cross section and z-position of the vertex. There are no major discrepancies between the MC and

data. There is still room for improvement because there was no hadronic final state calibration. However, the overall scale is wrong compared to H1PDF2000 by a factor 12% in the case of the high proton energy and by 8% the low energy. Finally, the first cross sections were obtained for the high and low proton energy run. The reduced cross section for E_p=920 GeV data is approximately 5% higher than the cross section for E_p=460 GeV data, which is compatible with the difference in the yield. Comparing the cross section measurement in this thesis with the results using H1 data from 96/97, the conclusion is that there is an overall normalisation problem in 2007 data.

The following step is to modify the phase space selected towards higher values of y to a maximum of $y \sim 0.85$ for the low energy run to measure F_L. The results in this work will be needed to perform the best F_L measurement.

Appendix A

Tables of the experimental results

In the following tables the results of the cross section measurements are listed. The kinematic variables, the reduced cross section, R and F_2 together with the systematics are presented for the E_p= 920 GeV and E_p= 460 GeV data from 2007. The values of R used for the extraction of F_2 are calculated using H1PDF2000.

Results for the E_p= 920 GeV data 2007												
Q^2 [GeV^2]	x	y	σ_r	F_2	δ_{tot} [%]	δ_{stat} [%]	δ_{unc} [%]	δ_{cor} [%]	δ_{E_e} [%]	δ_{θ_e} [%]	δ_{LAr} [%]	δ_{noise} [%]
12.0	$3.20 \cdot 10^{-4}$	0.369	1.402	1.436	1.9	0.4	0.9	1.7	−1.0	−1.3	0.3	−0.2
12.0	$5.00 \cdot 10^{-4}$	0.236	1.261	1.272	2.4	0.5	0.9	2.1	−1.0	−1.8	0.3	−0.1
12.0	$8.00 \cdot 10^{-4}$	0.148	1.187	1.191	2.8	0.6	1.0	2.5	−1.3	−2.2	0.2	−0.1
12.0	$1.30 \cdot 10^{-3}$	0.091	1.044	1.045	3.8	0.7	1.0	3.6	−2.5	−2.7	0.2	−0.1
12.0	$2.00 \cdot 10^{-3}$	0.059	0.909	0.909	4.3	0.7	1.0	4.1	−1.6	−2.9	−1.2	1.1
12.0	$3.20 \cdot 10^{-3}$	0.037	0.828	0.828	4.5	0.8	1.1	4.3	−1.6	−2.6	2.6	1.3
12.0	$6.31 \cdot 10^{-3}$	0.019	0.701	0.701	5.3	0.7	1.0	5.1	−1.9	−2.1	−2.9	3.1
12.0	$2.00 \cdot 10^{-2}$	0.006	0.546	0.546	19.0	1.1	1.2	18.9	−1.8	1.1	−14.2	12.2
15.0	$5.00 \cdot 10^{-4}$	0.295	1.358	1.375	2.1	0.4	0.9	1.9	−0.9	−1.6	0.4	−0.1
15.0	$8.00 \cdot 10^{-4}$	0.185	1.234	1.239	2.1	0.4	0.9	1.8	−0.9	−1.6	0.3	−0.1
15.0	$1.30 \cdot 10^{-3}$	0.114	1.142	1.144	2.5	0.5	0.9	2.3	−1.7	−1.5	0.3	−0.1
15.0	$2.00 \cdot 10^{-3}$	0.074	0.992	0.993	2.5	0.5	0.9	2.2	−0.2	−1.5	−0.8	−0.4
15.0	$3.20 \cdot 10^{-3}$	0.046	0.873	0.873	2.6	0.5	1.0	2.3	−0.4	−1.5	1.6	−0.2
15.0	$5.00 \cdot 10^{-3}$	0.030	0.782	0.782	4.9	0.6	1.0	4.7	−0.5	−1.3	4.5	0.0
15.0	$1.00 \cdot 10^{-2}$	0.015	0.644	0.644	3.8	0.5	1.0	3.6	−0.7	−0.7	−3.0	1.7
15.0	$3.20 \cdot 10^{-2}$	0.005	0.455	0.455	15.8	0.7	1.0	15.7	−1.5	2.1	−10.3	11.6
20.0	$5.00 \cdot 10^{-4}$	0.394	1.487	1.523	1.9	0.4	0.9	1.6	−0.6	−1.4	0.4	−0.2
20.0	$8.00 \cdot 10^{-4}$	0.246	1.330	1.341	2.1	0.4	0.9	1.9	−0.9	−1.6	0.3	0.0
20.0	$1.30 \cdot 10^{-3}$	0.151	1.193	1.196	2.2	0.4	0.9	1.9	−1.2	−1.5	0.3	−0.1
20.0	$2.00 \cdot 10^{-3}$	0.098	1.094	1.095	2.8	0.4	0.9	2.5	−1.9	−1.6	0.4	0.0
20.0	$3.20 \cdot 10^{-3}$	0.062	0.954	0.954	2.6	0.5	1.0	2.4	0.7	−1.7	0.8	−1.2
20.0	$5.00 \cdot 10^{-3}$	0.039	0.841	0.842	4.9	0.5	1.0	4.7	0.6	−1.8	4.3	−0.8
20.0	$1.00 \cdot 10^{-2}$	0.020	0.698	0.698	3.5	0.4	0.9	3.4	0.5	−1.4	2.8	−1.1
20.0	$3.20 \cdot 10^{-2}$	0.006	0.499	0.499	8.6	0.5	1.0	8.5	−0.1	−0.5	−5.7	6.3
25.0	$8.00 \cdot 10^{-4}$	0.308	1.444	1.464	1.9	0.5	1.0	1.6	−0.7	−1.4	0.4	−0.1
25.0	$1.30 \cdot 10^{-3}$	0.189	1.274	1.280	2.0	0.5	1.0	1.7	−0.9	−1.5	0.3	0.0
25.0	$2.00 \cdot 10^{-3}$	0.123	1.169	1.171	2.2	0.5	1.0	1.9	−1.2	−1.4	0.3	0.0
25.0	$3.20 \cdot 10^{-3}$	0.077	1.043	1.044	3.0	0.5	1.0	2.8	−2.2	−1.7	0.4	0.0

continued on next page

Results for the E_p= 920 GeV data 2007												
Q^2 [GeV^2]	x	y	σ_r	F_2	δ_{tot} [%]	δ_{stat} [%]	δ_{unc} [%]	δ_{cor} [%]	δ_{E_e} [%]	δ_{θ_e} [%]	δ_{LAr} [%]	δ_{noise} [%]
25.0	$5.00 \cdot 10^{-3}$	0.049	0.876	0.877	3.2	0.5	1.0	3.0	0.9	−1.6	2.1	−1.2
25.0	$8.00 \cdot 10^{-3}$	0.031	0.782	0.782	6.5	0.5	1.0	6.4	0.7	−1.5	6.1	−1.1
25.0	$1.30 \cdot 10^{-2}$	0.019	0.688	0.688	5.2	0.6	1.0	5.0	0.6	−1.6	4.0	−2.5
25.0	$2.00 \cdot 10^{-2}$	0.012	0.617	0.617	3.6	0.6	1.1	3.4	0.7	−1.5	2.0	−2.1
25.0	$3.98 \cdot 10^{-2}$	0.006	0.497	0.497	10.0	0.6	1.0	9.9	0.5	−1.2	−6.7	7.2
35.0	$8.00 \cdot 10^{-4}$	0.431	1.556	1.603	1.8	0.6	1.0	1.3	−0.7	−0.9	0.4	−0.3
35.0	$1.30 \cdot 10^{-3}$	0.265	1.374	1.387	1.9	0.5	1.0	1.5	−0.5	−1.4	0.3	0.0
35.0	$2.00 \cdot 10^{-3}$	0.172	1.240	1.245	1.9	0.5	1.0	1.5	−0.9	−1.2	0.3	0.0
35.0	$3.20 \cdot 10^{-3}$	0.108	1.124	1.126	2.5	0.5	1.0	2.3	−1.6	−1.5	0.3	0.0
35.0	$5.00 \cdot 10^{-3}$	0.069	0.958	0.959	2.7	0.6	1.0	2.4	1.0	−1.4	1.2	−1.3
35.0	$8.00 \cdot 10^{-3}$	0.043	0.839	0.840	4.5	0.6	1.0	4.4	1.0	−1.6	3.8	−1.2
35.0	$1.30 \cdot 10^{-2}$	0.027	0.728	0.728	6.8	0.7	1.1	6.6	1.0	−1.5	6.2	−1.6
35.0	$2.00 \cdot 10^{-2}$	0.017	0.671	0.671	5.1	0.7	1.1	4.9	0.7	−1.5	3.5	−3.0
35.0	$3.98 \cdot 10^{-2}$	0.009	0.540	0.540	5.8	0.6	1.0	5.7	0.9	−1.7	−3.8	3.7
45.0	$1.30 \cdot 10^{-3}$	0.341	1.461	1.485	1.7	0.6	1.0	1.2	−0.5	−1.0	0.4	−0.1
45.0	$2.00 \cdot 10^{-3}$	0.222	1.298	1.306	1.7	0.6	1.0	1.3	−0.7	−1.0	0.2	0.0
45.0	$3.20 \cdot 10^{-3}$	0.138	1.159	1.162	2.0	0.6	1.1	1.6	−0.9	−1.2	0.3	0.0
45.0	$5.00 \cdot 10^{-3}$	0.089	1.026	1.027	2.6	0.6	1.1	2.3	−2.0	−1.2	0.3	0.0
45.0	$8.00 \cdot 10^{-3}$	0.055	0.876	0.876	2.6	0.7	1.1	2.2	1.1	−1.4	1.2	−0.6
45.0	$1.30 \cdot 10^{-2}$	0.034	0.768	0.769	6.2	0.7	1.1	6.0	0.9	−1.3	5.6	−1.7
45.0	$2.00 \cdot 10^{-2}$	0.022	0.690	0.690	6.5	0.8	1.1	6.3	0.9	−1.3	5.6	−2.4
45.0	$3.20 \cdot 10^{-2}$	0.014	0.610	0.610	3.5	0.8	1.2	3.2	0.6	−1.0	2.0	−2.0
45.0	$6.31 \cdot 10^{-2}$	0.007	0.478	0.478	13.5	0.8	1.1	13.5	1.0	−1.5	−9.2	9.6
60.0	$1.30 \cdot 10^{-3}$	0.454	1.494	1.543	1.9	0.9	1.2	1.1	−0.6	−0.8	0.4	−0.3
60.0	$2.00 \cdot 10^{-3}$	0.295	1.389	1.404	1.7	0.7	1.1	1.2	−0.4	−1.1	0.2	0.0
60.0	$3.20 \cdot 10^{-3}$	0.185	1.221	1.226	1.7	0.7	1.1	1.1	−0.5	−0.9	0.2	0.0
60.0	$5.00 \cdot 10^{-3}$	0.118	1.075	1.077	2.4	0.7	1.1	1.9	−1.4	−1.2	0.3	0.0
60.0	$8.00 \cdot 10^{-3}$	0.074	0.919	0.920	2.5	0.8	1.2	2.1	0.6	−0.7	1.0	−1.5
60.0	$1.30 \cdot 10^{-2}$	0.045	0.778	0.778	3.4	0.8	1.2	3.0	1.2	−1.4	2.2	−0.9
60.0	$2.00 \cdot 10^{-2}$	0.030	0.705	0.705	6.8	0.9	1.2	6.6	0.6	−0.9	6.1	−2.1
60.0	$3.20 \cdot 10^{-2}$	0.018	0.612	0.612	5.4	0.9	1.2	5.2	0.6	−1.0	4.2	−2.7
60.0	$6.31 \cdot 10^{-2}$	0.009	0.481	0.481	8.8	0.9	1.2	8.7	1.1	−1.5	−6.2	5.7
90.0	$2.00 \cdot 10^{-3}$	0.443	1.383	1.424	2.2	1.3	1.4	1.1	−0.1	−1.0	0.3	−0.1
90.0	$3.20 \cdot 10^{-3}$	0.277	1.244	1.255	1.9	0.9	1.2	1.2	−0.4	−1.1	0.2	0.0
90.0	$5.00 \cdot 10^{-3}$	0.177	1.128	1.132	1.9	0.8	1.2	1.2	−1.0	−0.8	0.2	0.0
90.0	$8.00 \cdot 10^{-3}$	0.111	0.974	0.976	2.2	0.9	1.2	1.6	−0.8	−1.3	0.3	0.0
90.0	$1.30 \cdot 10^{-2}$	0.068	0.808	0.808	2.8	1.0	1.3	2.3	1.1	−0.9	1.3	−1.2
90.0	$2.00 \cdot 10^{-2}$	0.044	0.728	0.728	4.9	1.0	1.3	4.6	1.4	−1.3	3.8	−1.6
90.0	$3.20 \cdot 10^{-2}$	0.028	0.653	0.653	8.6	1.1	1.4	8.4	1.2	−1.2	7.5	−3.1
90.0	$5.00 \cdot 10^{-2}$	0.018	0.569	0.569	2.8	1.2	1.4	2.1	0.9	−1.0	−0.4	0.2
90.0	$1.00 \cdot 10^{-1}$	0.009	0.438	0.438	17.4	1.3	1.5	17.3	1.1	−1.2	−13.1	11.1
120.0	$3.20 \cdot 10^{-3}$	0.369	1.119	1.144	4.3	3.1	2.7	1.0	−0.9	−0.4	0.1	0.0
120.0	$5.00 \cdot 10^{-3}$	0.236	1.088	1.096	2.8	1.6	1.7	1.6	−0.2	−1.6	0.2	0.0
120.0	$8.00 \cdot 10^{-3}$	0.148	0.939	0.941	2.5	1.3	1.5	1.5	−0.9	−1.2	0.2	0.0
120.0	$1.30 \cdot 10^{-2}$	0.091	0.824	0.824	2.5	1.2	1.5	1.6	−1.2	−1.1	0.4	0.0
120.0	$2.00 \cdot 10^{-2}$	0.059	0.691	0.691	4.0	1.4	1.5	3.5	2.3	−0.9	1.7	−1.7
120.0	$3.20 \cdot 10^{-2}$	0.037	0.622	0.622	9.1	1.4	1.6	8.8	2.0	−1.1	7.9	−3.2
120.0	$5.00 \cdot 10^{-2}$	0.024	0.561	0.561	6.2	1.4	1.6	5.8	2.0	−1.2	4.8	−2.0
120.0	$1.00 \cdot 10^{-1}$	0.012	0.432	0.432	12.3	1.4	1.6	12.2	1.6	−0.9	−9.6	7.0

Results for the E_p= 460 GeV data 2007												
Q^2 [GeV^2]	x	y	σ_r	F_2	δ_{tot} [%]	δ_{stat} [%]	δ_{unc} [%]	δ_{cor} [%]	δ_{E_e} [%]	δ_{θ_e} [%]	δ_{LAr} [%]	δ_{noise} [%]
12.0	$8.00 \cdot 10^{-4}$	0.295	1.079	1.094	3.6	0.7	0.9	3.4	−1.3	−3.2	0.2	−0.1
12.0	$1.30 \cdot 10^{-3}$	0.182	0.986	0.990	4.3	0.8	0.9	4.2	−2.3	−3.5	0.1	−0.1
12.0	$2.00 \cdot 10^{-3}$	0.118	0.928	0.929	4.6	0.9	1.0	4.4	−1.9	−3.9	0.2	0.0
12.0	$3.20 \cdot 10^{-3}$	0.074	0.798	0.798	3.4	1.0	1.0	3.0	−0.2	−3.0	0.3	−0.1
12.0	$6.31 \cdot 10^{-3}$	0.037	0.690	0.690	6.2	0.8	1.0	6.1	−1.5	−3.1	−3.3	3.6
12.0	$2.00 \cdot 10^{-2}$	0.012	0.553	0.553	15.4	0.9	1.0	15.3	−1.5	0.2	−5.9	14.1
15.0	$8.00 \cdot 10^{-4}$	0.369	1.146	1.171	2.4	0.7	0.9	2.1	−0.9	−1.9	0.2	−0.1
15.0	$1.30 \cdot 10^{-3}$	0.227	1.030	1.038	2.9	0.8	0.9	2.6	−1.6	−2.0	0.2	−0.1
15.0	$2.00 \cdot 10^{-3}$	0.148	0.936	0.939	3.3	0.7	0.9	3.0	−2.3	−1.9	0.2	−0.1
15.0	$3.20 \cdot 10^{-3}$	0.092	0.849	0.850	3.1	0.8	0.9	2.9	−2.0	−2.0	0.3	−0.1
15.0	$5.00 \cdot 10^{-3}$	0.059	0.757	0.757	2.8	0.8	1.0	2.5	0.1	−2.1	−1.3	0.0
15.0	$1.00 \cdot 10^{-2}$	0.030	0.634	0.634	3.6	0.6	0.9	3.4	−0.2	−1.4	−2.3	2.1
15.0	$3.20 \cdot 10^{-2}$	0.009	0.491	0.491	13.0	0.7	0.9	12.9	−1.3	1.8	−3.7	12.2
20.0	$1.30 \cdot 10^{-3}$	0.303	1.113	1.128	2.3	0.8	0.9	2.0	−1.2	−1.5	0.2	−0.1
20.0	$2.00 \cdot 10^{-3}$	0.197	0.987	0.992	2.9	0.8	0.9	2.6	−1.9	−1.7	0.2	0.0
20.0	$3.20 \cdot 10^{-3}$	0.123	0.905	0.907	3.4	0.8	0.9	3.2	−2.7	−1.7	0.3	−0.1
20.0	$5.00 \cdot 10^{-3}$	0.079	0.824	0.825	2.9	0.8	1.0	2.6	−2.0	−1.6	0.6	−0.1
20.0	$1.00 \cdot 10^{-2}$	0.039	0.680	0.680	2.4	0.6	0.9	2.1	0.6	−1.6	−0.4	−1.1
20.0	$3.20 \cdot 10^{-2}$	0.012	0.514	0.514	6.8	0.6	0.9	6.7	0.0	−0.5	−1.8	6.4
25.0	$1.30 \cdot 10^{-3}$	0.379	1.201	1.230	2.4	1.3	1.0	1.7	−0.9	−1.5	0.2	0.0
25.0	$2.00 \cdot 10^{-3}$	0.246	1.043	1.053	2.3	0.9	1.0	1.9	−1.2	−1.4	0.2	0.0
25.0	$3.20 \cdot 10^{-3}$	0.154	0.950	0.953	3.1	0.9	1.0	2.8	−2.2	−1.7	0.2	0.0
25.0	$5.00 \cdot 10^{-3}$	0.098	0.853	0.854	3.7	0.9	1.0	3.5	−3.0	−1.7	0.4	−0.1
25.0	$8.00 \cdot 10^{-3}$	0.062	0.741	0.742	2.4	1.0	1.0	2.0	0.7	−1.5	−0.3	−1.1
25.0	$1.30 \cdot 10^{-2}$	0.038	0.661	0.662	3.4	1.0	1.0	3.0	0.6	−1.6	0.1	−2.5
25.0	$2.00 \cdot 10^{-2}$	0.025	0.593	0.593	3.2	1.1	1.0	2.8	0.7	−1.5	0.6	−2.1
25.0	$3.98 \cdot 10^{-2}$	0.012	0.531	0.531	7.7	0.8	1.0	7.6	0.5	−1.2	−1.9	7.2
35.0	$1.30 \cdot 10^{-3}$	0.530	1.301	1.368	2.3	1.4	1.1	1.5	−0.5	−1.4	0.2	0.0
35.0	$2.00 \cdot 10^{-3}$	0.345	1.144	1.165	2.1	1.0	1.0	1.5	−0.9	−1.2	0.1	0.0
35.0	$3.20 \cdot 10^{-3}$	0.215	1.028	1.035	2.7	1.0	1.0	2.2	−1.6	−1.5	0.2	0.0
35.0	$5.00 \cdot 10^{-3}$	0.138	0.921	0.923	3.2	1.0	1.0	2.9	−2.4	−1.5	0.3	0.0
35.0	$8.00 \cdot 10^{-3}$	0.086	0.792	0.793	2.7	1.1	1.0	2.2	1.0	−1.6	0.0	−1.2
35.0	$1.30 \cdot 10^{-2}$	0.053	0.689	0.689	3.0	1.1	1.0	2.5	1.0	−1.5	−0.6	−1.6
35.0	$2.00 \cdot 10^{-2}$	0.034	0.635	0.635	3.9	1.2	1.1	3.6	0.8	−1.5	1.0	−3.0
35.0	$3.98 \cdot 10^{-2}$	0.017	0.553	0.553	4.6	0.9	1.0	4.4	0.9	−1.7	−1.1	3.7
45.0	$2.00 \cdot 10^{-3}$	0.443	1.203	1.242	2.1	1.3	1.1	1.2	−0.7	−1.0	0.1	0.0
45.0	$3.20 \cdot 10^{-3}$	0.277	1.083	1.094	2.2	1.1	1.0	1.6	−0.9	−1.2	0.1	0.0
45.0	$5.00 \cdot 10^{-3}$	0.177	0.955	0.958	2.8	1.2	1.1	2.3	−2.0	−1.2	0.2	0.0
45.0	$8.00 \cdot 10^{-3}$	0.111	0.839	0.840	3.5	1.9	1.1	2.8	−2.3	−1.5	0.3	0.0
45.0	$1.30 \cdot 10^{-2}$	0.068	0.719	0.719	2.9	1.3	1.1	2.3	0.9	−1.3	−0.2	−1.7
45.0	$2.00 \cdot 10^{-2}$	0.044	0.651	0.651	3.5	1.3	1.1	3.0	0.9	−1.3	0.3	−2.4
45.0	$3.20 \cdot 10^{-2}$	0.028	0.599	0.599	3.1	1.4	1.1	2.6	0.6	−1.0	0.4	−2.0
45.0	$6.31 \cdot 10^{-2}$	0.014	0.515	0.515	10.5	1.9	1.0	10.3	1.0	−1.5	−3.1	9.6
60.0	$2.00 \cdot 10^{-3}$	0.591	1.304	1.383	3.8	3.1	1.8	1.1	−0.4	−1.1	0.1	0.0
60.0	$3.20 \cdot 10^{-3}$	0.369	1.145	1.167	2.1	1.5	1.1	1.1	−0.5	−0.9	0.0	0.0
60.0	$5.00 \cdot 10^{-3}$	0.236	1.006	1.013	2.6	1.4	1.1	1.9	−1.4	−1.2	0.2	0.0
60.0	$8.00 \cdot 10^{-3}$	0.148	0.856	0.858	2.6	1.4	1.1	1.9	−1.4	−1.3	0.2	0.0
60.0	$1.30 \cdot 10^{-2}$	0.091	0.760	0.761	2.8	1.5	1.2	2.0	−1.7	−1.0	0.5	0.0
60.0	$2.00 \cdot 10^{-2}$	0.059	0.677	0.678	3.1	1.5	1.2	2.4	0.6	−0.9	−0.3	−2.1
60.0	$3.20 \cdot 10^{-2}$	0.037	0.596	0.597	3.8	1.7	1.2	3.1	0.6	−1.0	0.4	−2.7

continued on next page

Results for the E_p= 460 GeV data 2007												
Q^2 [GeV^2]	x	y	σ_r	F_2	δ_{tot} [%]	δ_{stat} [%]	δ_{unc} [%]	δ_{cor} [%]	δ_{E_e} [%]	δ_{θ_e} [%]	δ_{LAr} [%]	δ_{noise} [%]
60.0	$6.31 \cdot 10^{-2}$	0.019	0.492	0.492	6.8	1.3	1.1	6.5	1.1	−1.5	−2.3	5.7
90.0	$3.20 \cdot 10^{-3}$	0.554	1.377	1.435	5.2	4.5	2.5	1.2	−0.4	−1.1	0.1	0.0
90.0	$5.00 \cdot 10^{-3}$	0.354	1.091	1.108	2.7	2.0	1.3	1.2	−1.0	−0.8	0.1	0.0
90.0	$8.00 \cdot 10^{-3}$	0.222	0.915	0.920	2.6	1.7	1.2	1.5	−0.8	−1.3	0.2	0.0
90.0	$1.30 \cdot 10^{-2}$	0.136	0.794	0.795	3.0	1.7	1.2	2.1	−1.4	−1.5	0.3	0.0
90.0	$2.00 \cdot 10^{-2}$	0.089	0.698	0.699	2.5	1.8	1.3	1.2	−0.4	−1.1	0.5	0.0
90.0	$3.20 \cdot 10^{-2}$	0.055	0.607	0.607	4.4	1.9	1.3	3.8	1.2	−1.2	0.6	−3.1
90.0	$5.00 \cdot 10^{-2}$	0.035	0.545	0.545	3.4	2.1	1.4	2.3	0.9	−1.0	−0.9	0.2
90.0	$1.00 \cdot 10^{-1}$	0.018	0.430	0.430	12.5	1.7	1.2	12.4	1.1	−1.2	−4.8	11.1
120.0	$8.00 \cdot 10^{-3}$	0.295	1.105	1.114	5.0	4.2	2.3	1.5	−0.9	−1.2	0.1	0.0
120.0	$1.30 \cdot 10^{-2}$	0.182	0.884	0.886	3.7	2.8	1.7	1.6	−1.2	−1.1	0.1	0.0
120.0	$2.00 \cdot 10^{-2}$	0.118	0.784	0.785	3.3	2.5	1.6	1.6	−0.7	−1.3	0.3	0.0
120.0	$3.20 \cdot 10^{-2}$	0.074	0.636	0.636	3.4	2.6	1.5	1.6	0.2	−1.4	0.6	0.0
120.0	$5.00 \cdot 10^{-2}$	0.047	0.534	0.534	4.6	2.8	1.6	3.3	2.0	−1.2	0.0	−2.0
120.0	$1.00 \cdot 10^{-1}$	0.024	0.441	0.441	8.5	2.2	1.4	8.1	1.6	−0.9	−3.3	7.0

List of Figures

List of Tables

Bibliography

[1] H1 collaboration, *Running at Low Proton Beam Energies*, H1-10/05-622, October 2005, hep-ex/0302034.

[2] R. Thorne, *The importance of a measurement of $F_L(x,Q^2)$ at HERA*, Ringberg Workshop, October 2005, published in the Proceedings [http://www.mppmu.mpg.de].

[3] J. Feltesse, *Measurement of the longitudinal structure function at low x at HERA*. Ringberg Workshop, October 2005, published in the Proceedings [http://www.mppmu.mpg.de].

[4] H Abramowicz and A. C. Caldwell, *HERA collider physics*, Rev. Mod. Phys. **71** (1999) 1275-1409.

[5] A. M. Cooper-Sakar, R. C. E. Devenish and A. de Roeck, *Structure Functions of the Nucleon and their Interpretation*, Int. J. Mod. Phys. **A 13** (1998), no. 20 3385-3586 hep-ph/9712301.

[6] H1 collaboration, *Deep-Inclusive ep Scattering at Low x and a Determination of α_s*, DESY 00-181, December 2000, hep-ex/0012053.

[7] G. Altarelli and G. Marinelli, *Transverse momentum of jets in electroproduction from quantum chromodynamics*, Phys. Lett. **B76** 89-94 (1978).

[8] E. D. Bloom et al. *High-energy inelastic ep scattering at 6 degrees and 10 degrees*, Phys. Rev. Lett. **23**, 930 (1969).

[9] R. P. Feynman, *Very high-energy collisions of hadrons*, Phys. Rev. Lett. **23**, 1414 (1969).

[10] J. D. Bjorken, *Asymptotic sum rules at infinite momentum*, Phys. Rev. Lett. **179**, 1547 (1969).

[11] C. G. Callan, D. J. Gross, *High-Energy Electroproduction and the Constitution of the Electric Current*, Phys. Rev. Lett. **22**, 156-159 (1969).

[12] I. Abt et al., *The H1 detector at HERA*, Nucl. Instr. Meth. **A386** (1997) 310-347.

[13] I. Abt et al., *The tracking, calorimeter and muon detectors of the H1 experiment at HERA*, Nucl. Instr. Meth. **A386** (1997) 348-396.

[14] M. Cuje et al., *H1 High Luminosity Upgrade 2000, CIP and Level 1 Vertex Trigger*, presented to the 44th DESY PRC (1998), DESY-PRC98/02 and H1 internal report H1-IN-535 (01/1998).

[15] B. List, *The H1 silicon tracker*, Proceedings of VERTEX2003, Nucl. Instrum. Meth. **A549** (2005) 33-36.

[16] B. List, *The H1 central silicon tracker*, Proceedings of VERTEX2001, Nucl. Instrum. Meth. **A501** (2001) 49-53.

[17] B. Andrieu et al., *The H1 liquid argon calorimeter system*, Nucl. Instrum. Meth. **A336** (1993) 460-498.

[18] B. Andrieu et al., *Results from pion calibration runs for the H1 liquid argon calorimeter and comparisons with simulations*, Nucl. Instrum. Meth. **A336** (1993) 499-509.

[19] T. Nicholls et al., *Performance of an electromagnetic lead/scintillating-fibre calorimeter for the H1 detector*. Nucl. Instrum. Meth. **A374** (1996) 149-156.

[20] R. D. Appuhn et al., *Hadronic response and e/pi separation with the H1 lead/fibre calorimeter*. Nucl. Instrum. Meth. **A382** (1996) 395-412.

[21] H. Cronström et al, *The H1 forward muon spectrometer*, Nucl. Instrum. Meth. **A340** (1994) 304-308.

[22] M. Nožička, *The forward and backward silicon trackers of H1*, Nucl. Instrum. Meth. **A501** (2003) 54-59.

[23] A. A. Glazov, *Measurement of the Proton Structure Functions $F_2(x,Q^2)$ and $F_L(x,Q^2)$ with the H1 Detector at Hera*, Humboldt University Berlin, DESY-THESIS-2005-030, April 1998.

[24] J. Kretzschmar, *A Trigger with the BST-PAD Detector for the H1 Experiment*, Humboldt University Berlin, Diplomarbeit 12/2006.

[25] J. Kretzschmar, Dissertation in preparation

[26] A. Vargas Treviño, *Determination of the energy scale uncertainty for the measurement of F_2 at low values of Q^2 using the H1 detector*, University of Dortmund, Dissertation 07/2006.

[27] O. Beherendt, *Measurement of the proton structure function F_2 at low Q^2 at HERA*, University of Dortmund, Dissertation 09/2006.

[28] D. Eckstein, *Messung der Longitudinalen Struckturfunktion $F_L(x,Q^2)$ mit dem HERA-Experiment H1*, Humboldt University Berlin, dissertation 01/2002.

[29] T. Lašotovička, *Measurement of the Inlclusive Deep Inelastic Scattering Cross Section at Low Q^2*, Dissertation 05/2004.

[30] V. Arkadov, *Measurement of the Deep Inelastic ep Scattering Cross Section using the Backward Silicon tracker at the H1 Detector at HERA*, Humboldt University Berlin, dissertation 10/2000.

[31] M. Nožička, *Forward Silicon Tracker of the H1 Experiment: Hardware and Study of D^* Meson Detection*, Charles University Prague, Dissertation 2006.

[32] I. Tsurin, *The Backward Silicon Tracker Trigger of the HERA Experiment H1*, Humboldt University Berlin, Dissertation 03/2003.

[33] R. Plačakytė, *First Measurement of Charged Current Cross Sections with Longitudinally Polarised Positrons at HERA*, Ludwig-Maximilians-University Munich, Dissertation 06/2006.

[34] L. Finke, *Measurement of Charm and Beauty Dijet Cross Sections in Photoproduction*, Universiy of Hamburg, Dissertation 2006.

[35] H1prelim-07-042, *Inclusive ep Scattering Cross Section at low Q^2 and high y*, presented at DIS 2007, Munich, available at http://www-h1.desy.de/h1/www/publications, 2007.

[36] C. Adloff et al. Measurement and QCD Analysis of Neutral and Charged Current Cross Sections at HERA, Eur. Phys. J. **C30** (2003) 1-32, [hep-ex/0304003].

[37] G. A. Schuler and H. Spiesberger, *DJANGO: The Interface for the event generators HERACLES and LEPTO*, in W. Buchmüller and G. Ingelman, editors, *Physics at HERA, vol 3*, pages 1419-1430, 1992.

[38] H1 Physics Working Group for Inclusive Measurements, http://www-h1.desy.de/h1/www/h1work/inc/index.html.

[39] M. Klein, *One or two proton beam energies*, Low E_p analysis meeting, Zeuthen, 4.5.2007.

[40] D. Pitzl, *Lumi-problem-Report & discussion*, presentation at the H1 Physics Plenary Meeting, 21/22 June 2007, and documentation page.

[41] *ROOT, an Object-Oriented Data Analysis Framework*, http://root.cern.ch

Acknowledgments

I would like to thank Prof. Dr. Hermann Kolanoski, Prof. Dr. Thomas Naumann and Dr. Peter Kostka for the opportunity to study and work at DESY. I am also grateful to Peter Kostka for the opportunity he gave me to take active part in the H1 group, participating in the "Low energy meetings" and the "H1 weeks" in Hamburg. All my gratitude goes to Jan Kretzschmar for his support, help and all what I learnt working with him and of course, for his patience. Despite being really busy with his PhD, he had always time to answer my countless questions. I want to thank Dr. Alexandre Glazov for his useful suggestions, advice and motivation and all the H1 members in Hamburg who helped me and made my stays there really nice. Finally, I would like to mention Peter Steinbach, who together with Jan Kretzschmar, created a friendly atmosphere in our office in Zeuthen. I wish them all the best in their new projects.

Quiero dar las gracias a mi familia, especialmente a mis padres y mis hermanas, por su cariño y apoyo incondicional y agradecer a mis padres que vinieran a visitarme a Berlín mientras estuve trabajando en DESY. Ich muss auch mich bei Robert bedanken, der mich in jeder Lebenslage unterstützt.